SIMULATION OF A HOT MIRROR PARABOLIC TROUGH SOLAR COLLECTOR RECEIVER

Victor Siuluta Kaluba

‘**A thesis submitted to the Faculty of Science in fulfilment of the requirement for the degree of Doctor of Philosophy**’

Johannesburg, 2017

Declaration

I declare that this thesis is my own unaided work. It is being submitted for the award of the Doctor of Philosophy at the University of Witwatersrand, Johannesburg. It has not being submitted before for any degree or examination at any other University.

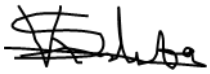

23rd day of November, 2017 in Johannesburg

Abstract

Parabolic trough solar collectors (PTSC) are currently the most mature solar collecting technology, applied commercially for electricity generation. High input temperature in power plants are desired for improved efficiency and help reduce electricity costs. However, at high temperatures, heat losses through radiation increase significantly.

Thermal radiation transfer is the dominant heat loss mechanism in PTSC receivers operating at high temperatures. In existing systems, the radiation losses are reduced by using a selective absorber coating placed on the absorber pipe. It has optical properties that suppress infrared radiation (IR) emissions. The material absorbs well in the solar wavelength range $(0.3\ to\ 2.5\mu m)$ but emits poorly in the infrared (IR) wavelength range. However, the material degrades at temperatures beyond 400^{o}C resulting in high IR emission.

This study developed a theoretical framework to characterize a different approach, alternative to the selective coating in reducing heat losses. This is the use of a hot mirror coating in a PTSC receiver. The coating is placed on the inner surface of the glass cover to reflect infrared radiation emanating from the absorber pipe back for reabsorption. The hot mirror is transparent to solar radiation and reflective in the wavelengths above $2.5\mu m$. The formulations developed described the thermal interactions in a hot mirror coated PTSC receiver.

To describe the heat loss reduction mechanisms, the study modelled theoretically the long range thermal radiation interactions inside the receiver unit. The model used discretization of the active surfaces to account for all the dominant radiation interactions. Different simulations scenarios were done to predict receiver performance. The performance of various candidates for hot mirror coating (ITO, Gold and Silver) were investigated. The effects of variation of some hot mirror optical parameters on overall plant efficiency was also investigated. The simulation was validated using other simulation works and experimental data. The results showed a close match with a discrepancy of 0.7%.

High HTF temperatures were attained using hot mirrors. ITO gave the highest HTF temperature. The hot mirror thermal stability is not compromised since the glass cover stays cooler than the absorber pipe (< 400^{o}C). The glass cover temperatures were far less than the absorber pipe temperatures. Even with the higher temperature of ITO (500^{o}C), the glass cover never reached above 400^{o}C. Solar transmissivity for the hot mirror materials is as important as the need for high HTF out temperatures.

Dedication

To my family, let this mark the fruits of your love and patience

Acknowledgements

The work accomplished in this thesis could not have been any easier without the support of many people and organizations. Firstly, I would like to thank my supervisor, Dr. Philippe Ferrer, for his enduring patience, trust and encouragement. Your guidance and insight made executing this study more bearable. “You always lifted me up”.

To my friends I met during the course of our study, I appreciate the companionship and sharing moments of difficulties. You all could rise to the occasion whenever called upon. I salute you.

To my institution, The University of Zambia, I thank management for the support during the course of my studies. I also thank the STRECC Project for the help rendered during my stay in South Africa.

TABLE OF CONTENTS

LIST OF FIGURES

LIST OF TABLES

ABBREVIATIONS

A	Area
AP	Absorber pipe
CSP	Concentrated solar collector
CV	Control volume
DSG	Direct steam generation
EES	Engineering equation solver
ET	Equation of time
FVM	Finite volume method
GC	Glass cover
HCE	Heat collecting element
HTF	Heat transfer fluid
IEA	International energy agency
IR	Infrared radiation
ITO	Indium Tin Oxide
LST	Local standard time
MW_e	Megawatts electricity
MW_{th}	Megawatts thermal
PET	Polyethylene terephthalate
PTR70	Schott's 2008 parabolic trough receiver
SC	Selective coating
SCA	Selective coating absorber
SEGS	Solar electricity generating system
ST	Standard time
UNFCCC	United Nations framework conference on climate change

NOMENCLATURE

$\boldsymbol{Q}$	Heat transfer rate (W)
$\dot{\boldsymbol{q}}_{\boldsymbol{COND}}$	Conduction Heat flux (W/m^2)
$\dot{\boldsymbol{q}}_{\boldsymbol{CONV}}$	Convection Heat flux (W/m^2)
$\dot{\boldsymbol{q}}_{\boldsymbol{RAD}}$	Radiation Heat flux (W/m^2)
$\dot{\boldsymbol{q}}_{\boldsymbol{sol}}$	Solar Irradiance (W/m^2)
$\dot{\boldsymbol{q}}_{\boldsymbol{A,\theta,i\pm1}}$,	Conduction heat transfer rate along AP circumference
$\dot{\boldsymbol{q}}_{\boldsymbol{G,\theta,i\pm1}}$	Conduction heat transfer rate along GC circumference
$\dot{\boldsymbol{q}}_{\boldsymbol{A,z,j\pm1}}$	Conduction heat transfer rate along AP length
$\dot{\boldsymbol{q}}_{\boldsymbol{G,z,j\pm1}}$	Conduction heat transfer rate along GC length
$\dot{\boldsymbol{q}}_{\boldsymbol{G,sol}}$	Solar Irradiance on GC (W/m^2)
$\dot{\boldsymbol{q}}_{\boldsymbol{A,sol}}$	Solar Irradiance on AP (W/m^2)
$\dot{\boldsymbol{q}}_{\boldsymbol{AG,IR}}$	Infrared radiation from AP to GC (W/m^2)
$\dot{\boldsymbol{q}}_{\boldsymbol{GG,IR}}$,	Infrared radiation from GC to GC (W/m^2)
$\dot{\boldsymbol{q}}_{\boldsymbol{GA,IR}}$	Infrared radiation from GC to AP (W/m^2)
$\dot{\boldsymbol{q}}_{\boldsymbol{IR,refl}}$	Back reflected Infrared radiation
$\dot{\boldsymbol{q}}_{\boldsymbol{IR,1\,refl}}$	Singly reflected infrared radiation
$\dot{\boldsymbol{q}}_{\boldsymbol{IR,2refl}}$	Doubly reflected infrared radiation
$\dot{\boldsymbol{q}}_{\boldsymbol{GO,IR}}$	Infrared radiation from GC to Environment (W/m^2)
$\dot{\boldsymbol{q}}_{\boldsymbol{AF,conv}}$	Convection Heat transfer rate from AP to HTF (W/m^2)
$\dot{\boldsymbol{q}}_{\boldsymbol{GO,conv}}$	Convection Heat transfer rate from GC to Environment
$\dot{\boldsymbol{m}}$	Mass flow rate (kg/s)
$\boldsymbol{C_p}$	Specific heat capacity
$\boldsymbol{T_{j+1}^F}$	Temperature of the $(j+1)^{th}$ HTF control volume
$\boldsymbol{T_j^F}$	Temperature of the $(j)^{th}$ HTF control volume
$\boldsymbol{T_i^A}$	Temperature of the $(i+1)^{th}$ AP control volume
$\boldsymbol{T_{i-1}^A}$	Temperature of the $(i-1)^{th}$ AP control volume

$\boldsymbol{T_{i+1}^{A}}$	Temperature of the $(i+1)^{th}$ AP control volume
$\boldsymbol{T_{i}^{G}}$	Temperature of the $(i)^{th}$ GC control volume
$\boldsymbol{T_{i-1}^{G}}$	Temperature of the $(i-1)^{th}$ GC control volume
$\boldsymbol{T_{i+1}^{G}}$	Temperature of the $(i+1)^{th}$ GC control volume
$\boldsymbol{T_s}$	Surface temperature
$\boldsymbol{T_f}$	Fluid temperature
$\boldsymbol{E_\lambda}$	Black body emissive power (W)
$\boldsymbol{L_{st}}$	Local meridian where standard time is based
$\boldsymbol{L_{loc}}$	The meridian of the location
N	n^{th} day of a year
$\boldsymbol{r_A}$	AP Radius
$\boldsymbol{r_G}$	GC Radius
$\boldsymbol{k_A}$	AP Thermal conductivity of a material
$\boldsymbol{k_G}$	GC Thermal conductivity of a material
T	Temperature
K	Kelvin scale (K)
L	Length (m)
I	Radiation intensity (W/m^2)
d	Distance (m)
$\boldsymbol{\hat{X}_{ijkl}}$	Radiation Vector from point ij to point kl
$\boldsymbol{\hat{n}_{kl}}$	Unit vector on point kl
ΔL	Difference in length (m)
$\boldsymbol{\Delta T}$	Difference in temperature (K)
$\boldsymbol{\Delta s_A}$	Arc length on AP (m)
$\boldsymbol{\Delta s_G}$	Arc length on GC (m)
$\boldsymbol{\frac{dT}{dx}}$	Temperature gradient along length (K/m)
$\boldsymbol{r_A}$	Radius of AP
$\boldsymbol{Nu}$	Nusselt number

$\boldsymbol{h_f}$	Convective heat transfer coefficient for the HTF
$\boldsymbol{h_w}$	Convective heat transfer coefficient for the wind
$\boldsymbol{Re}$	Reynold's number
$\boldsymbol{Pr}$	Prandtl number
$\boldsymbol{F_{1\rightarrow 2}}$	View factor from emitting area 1 to receiving area 2
$\boldsymbol{R_{ij}^{A}}$	Radiation emitted from a point ij on AP
$\boldsymbol{F_{li}^{GA}}$	View factor of point ij on GC for radiation from AP
$\boldsymbol{F_{li}^{GG}}$	View factor of point ij on GC for radiation from GC
$\boldsymbol{F_{li}^{AG}}$	View factor of point ij on AP for radiation from GC
$\boldsymbol{A_{kl}}$	A point kl on AP
$\boldsymbol{A_{ij}}$	A point ij on AP

GREEK LETTERS

α_h	molecular diffusivity of heat $(\mathrm{m}^2/\mathrm{s})$
ρ	Material density $(\mathrm{kg}/\mathrm{m}^3)$
ε	Surface emissivity
η	Efficiency
θ	Angle in radians
λ	Wavelength (m)
$\delta\omega$	Solid Angle in radians
μ	Viscosity
ν	molecular diffusivity of momentum $(\mathrm{m}^2/\mathrm{s})$
σ	Stefan-Boltzmann constant $(5.67 \times 10^{-8}\ \mathrm{W/m^2K^4})$
v_w	wind velocity (m/s)
ω	Hour angle (Degrees)
π	Pi (3.142)
τ	Spectral transmissivity
$\rho_{G,sol}$	Solar reflectivity on GC
$\rho_{A,sol}$	Solar reflectivity on GC
$\rho_{A,IR}$	Infrared reflectivity on AP
$\rho_{G,IR}$	Infrared reflectivity on GC
$\rho_{A,IR}$	Infrared reflectivity on AP
$\alpha_{A,sol}$	Solar absorption on AP
α	Spectral absorptivity

SUBSCRIPTS

$\boldsymbol{i}$	Designation for a point on the circumference
$\boldsymbol{j}$	Designation for a point along the axial length
$\boldsymbol{k}$	Point on circumference in radiative contact with ij
$\boldsymbol{m}$	Point on axial length in radiative contact with ij
$\left(\frac{\boldsymbol{i+k}}{\boldsymbol{2}}\right)\left(\frac{\boldsymbol{j+l}}{\boldsymbol{2}}\right)$	Midway between two radiatively interacting points
$\boldsymbol{i-N_m}$	Designation for an extreme full area point on the circumference in radiative contact with ij on the left side
$\boldsymbol{i+N_m}$	Designation for an extreme full area point on the circumference in radiative contact with ij on the left side
$\boldsymbol{i+N_m+1}$,	Designation for an extreme fractional area point on the circumference in radiative contact with ij on the left side
A	Considered on AP
G	Considered on GC
e	Electric power
th	Thermal power

Chapter 1 Introduction

1.0 Background

Global climate concerns and increasing costs of fossil fuels have made inevitable advancements in renewable energy technologies, particularly solar energy. Clean non-polluting energy sources are now sought after as anthropogenic induced contributions to climate change [1] and finiteness of fossil fuels [2] have now become apparent. According to Kalogirou [2], if the current global energy consumption rates are not checked, the world reserves for oil and gas would only be adequate to meet global energy demand for another 40 and 60 years respectively and 250 years for coal.

The continued burning of fossil fuels to meet global energy needs not only depletes the resources, but also increases carbon dioxide emissions. It is estimated that carbon dioxide contributes 50% of the human induced global warming [2]. The United Nations Framework Convention on Climate Change (UNFCCC) introduced the Copenhagen Account [3], where it was agreed that measures must be taken to keep global temperature increase to below 2^{o}C [3]. This has been challenging given that fossil fuels have continued to be primary energy sources whilst world energy demand has continued to increase.

Access to modern energy services can be correlated to the wellbeing of mankind, later on the development of any country. The provision of clean water, sanitation and health care, reliable and efficient lighting, cooking, heating and cooling, mechanical power, transport and telecommunication services depends on availability to modern energy services [4]. Sub-Saharan Africa has seen rapid economic growth and energy use has risen by 45%. However, access to modern energy services, though increasing, remains limited. Despite many positive efforts, more than 620 million people remain without access to electricity and nearly 730 million rely on the traditional use of solid biomass for cooking [4, 5]. This means continued exposure to indoor environments with smoke that are currently linked to 3.5 million premature deaths each year [4, 5].

Renewable energies, particularly solar energy, has shown great potential as a means to move the global energy production away from fossil fuels to non-polluting sources. Solar energy can be harnessed through photovoltaic or solar thermal technologies. Photovoltaic conversion is the direct conversion of sunlight into electricity with no intervening heat engine [6]. Solar thermal involves the use of collectors that capture and transform solar radiation to heat. This can then be used in heat applications or converted to mechanical work for direct use or electricity generation, which is the interest of our study. It is estimated that $1m^2$ of solar collector mirrors prevents 12 tonnes of CO_2 from being emitted annually into the atmosphere [7]. This makes solar thermal energy a strong candidate for sustainable development.

Solar thermal collectors are a special kind of heat exchangers. They transform solar radiation energy to internal energy of a transport medium. There are two types of solar thermal collectors which are further differentiated based on component layout. The two major types are non-concentrating or stationary and concentrating (CSP) or sun tracking [8]. The former has a same area for intercepting and for absorbing solar radiation, whereas the concentrating solar collector has large reflecting surfaces that intercept and redirect (focus) the sun's beam radiation to a smaller receiving area, thereby increasing the radiation flux. Concentrating collectors are made to track the sun on its path across the sky. Table 1.1 shows the various types of solar thermal collectors with some of their descriptive characteristics.

Table 1.1: Types of solar collectors [8]

Motion	Collector Type	Absorber Type	Concentration Ratio	Indicative Temperature Range (°C)
Stationery	Flat-Plate collector (FPC)	Flat	1	30-80
	Evacuated tube collector (ETC)	Flat	1	50-200
	Compound parabolic collector (CPC)	Tubular	1-5	60-240
Single axis tracking	Compound parabolic collector (CPC)	Tubular	5-15	60-300
	Linear Fresnel reflector (LFR)	Tubular	10-40	60-250
	Cylindrical trough collector (CTC)	Tubular	15-50	60-300
	Parabolic trough collector (PTC)	Tubular	10-85	60-400
Two axis tracking	Parabolic dish reflector (PDR)	Point	600-2000	100-1500
	Heliostat field collector (HFC)	Point	300-1500	150-2000

Note: *Concentration ratio is defined as the aperture area divided by the receiver/absorber area of the collector*

Solar radiation is a high-temperature, high energy source at its origin, the Sun, where the irradiance is about 63 MW/m^2. However, Sun–Earth geometry dramatically decreases the solar energy flow down to around 1 kW/m^2 on the Earth's surface [7]. As such, optical concentration is adopted through concentrating solar power technologies (CSP) in order to raise the temperatures at which thermal energy is obtained.

There are four types of CSP systems. Each is either line focusing or point focusing. The parabolic trough solar collector and Linear Fresnel reflector are line focusing. The parabolic dish and central receiver are point focusing. Figure 1.1 illustrates the configuration of each CSP and the respective working principle.

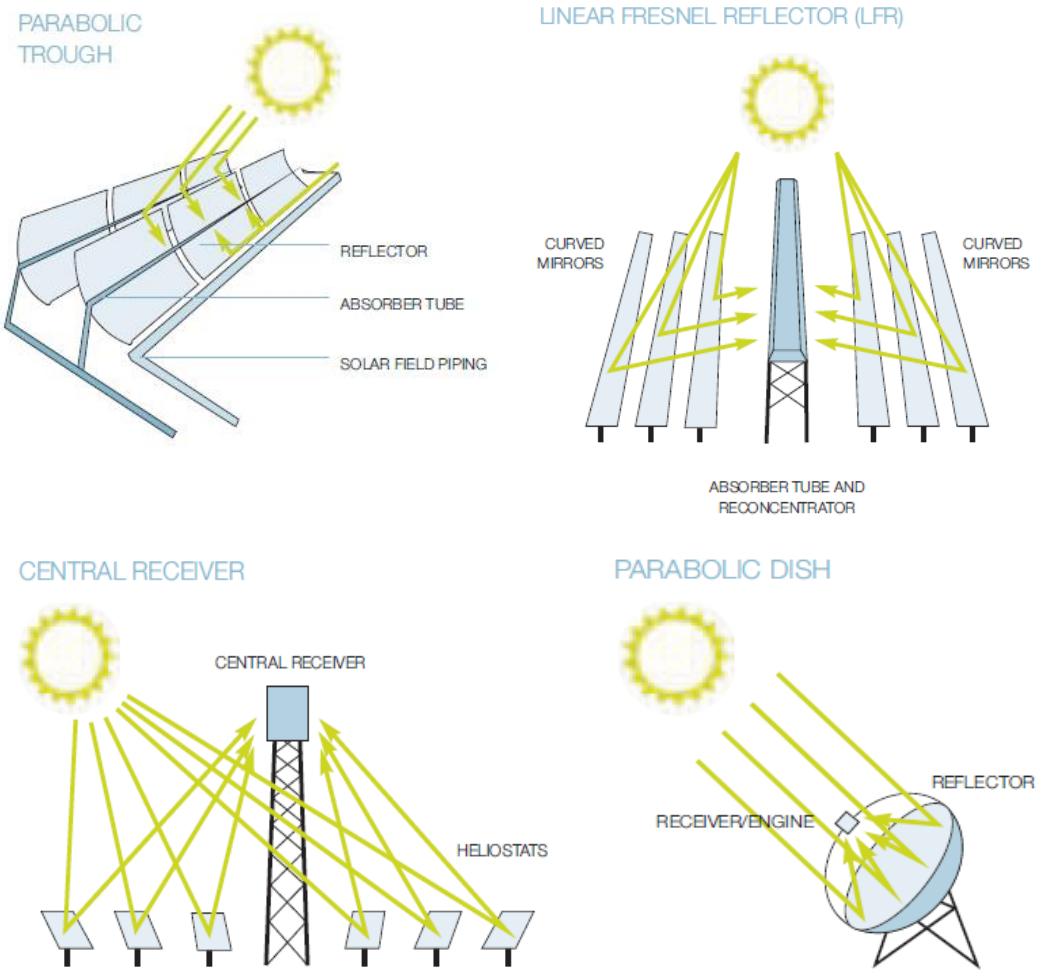

Figure 1.1: Illustration of CSP systems [10]

Parabolic trough solar collectors (PTSC) are the most proven and mature of the concentrating solar power technologies used today for electricity generation [9,10, 11,12,13,14] and process heat applications [9,15,16,17]. The biggest application of this type of system is the Southern California power plants, known as solar electric generating systems (SEGS), which have a total installed capacity of 354 MW_e [12]. Another important application of this type of collector is installed at Plataforma Solar de Almeria (PSA) in Southern Spain mainly for experimental purposes with a total installed capacity of 1.2 MW_{th} [13].

Parabolic trough solar collectors are made by bending mirrored surfaces into a parabolic trough shape, which is used to concentrate sunlight on to receiver tubes placed in the trough's focal line. The receiver is the heat exchange element (HCE). It is composed of a metallic absorber pipe (AP) coated on its outer surface with a selective absorbing material. The absorber pipe is enclosed in an evacuated glass tube or glass cover (GC). A heat transfer fluid (HTF) circulates in the absorber pipe carrying with it heat abstracted from the sun to points of application. The system tracks the sun along one axis during operation.

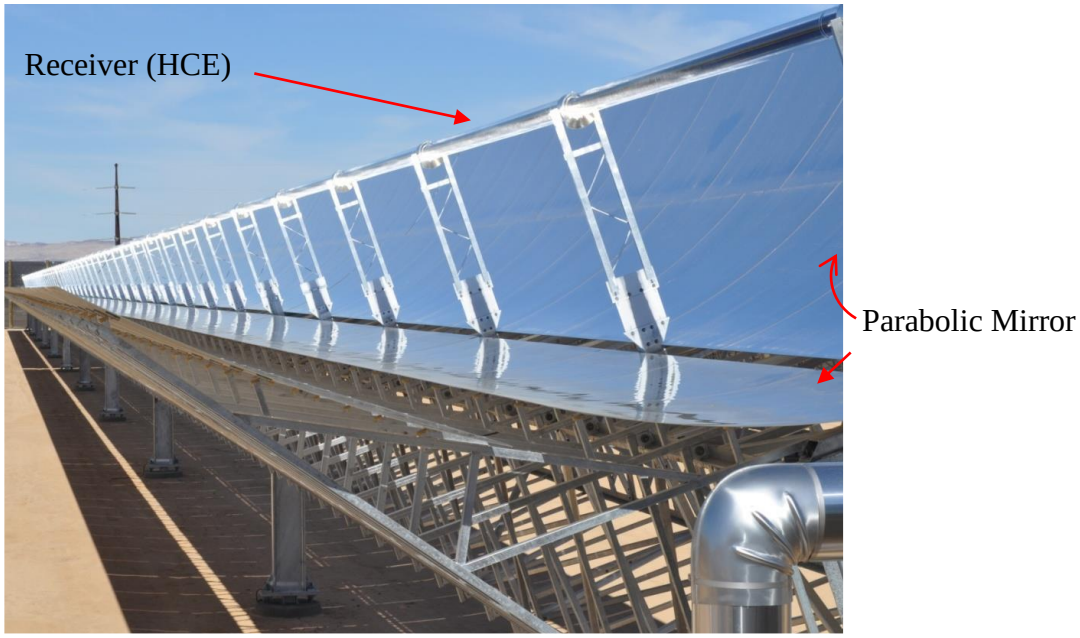

Figure 1.2: Ultimate Trough Demonstration loop developed by FLABEG GmbH [18]

Despite being tested and proven commercially, a lot of research and development focused on the performance of the PTSC system or its components is still being done. High temperatures are needed to improve efficiencies in systems that are thermally fed by parabolic trough solar collectors, such as solar electricity generation plants (SEGS). Thus reducing thermal losses in solar receivers is imperative.

It is the core of this study to achieve a high operating temperatures in parabolic trough solar receivers. The study is motivated by adopting a different approach for minimizing heat losses, i.e. 'use of a hot mirror (herein sometimes called "hot mirror") to confine infrared radiations within a solar receiver through back reflections'. The study models a PTSC receiver unit with a hot mirror. It develops formulations for describing the thermal interactions inside the receiver that include recaptured emitted Infrared radiation. Existing systems use a method of suppressing Infrared emissions from the surface of the absorber pipe. They use selective absorber coatings. These emit lowly in the Infrared wavelength range and absorbs highly in the visible range.

1.1 Problem Statement

From Stefan-Boltzmann law [19-21], any surface at a given absolute temperature emits energy with an order of magnitude proportional to the fourth power of its temperature (T^4). In solar receivers, infrared (IR) radiation emissions become increasingly significant as the absorber pipe temperature increases.

Existing parabolic solar receivers use a selective absorber coating on the absorber pipe to reduce radiative heat losses. The principle is: the selective absorber coating emits poorly in the infra-red (IR) wavelength range whilst having a higher absorptance in the visible region of the solar spectrum. This method is effective in reducing receiver heat loss by suppressing infrared radiation emission.

However, it is only effective in as long as the selective material can withstand absorber temperatures. Currently most commercially available selective materials decompose at a temperature of 400^{o}C [22-25] Beyond this temperature, most used selective absorber coating materials thermally decompose. As such, many of the parabolic trough plants currently deployed operate at temperatures below 400^o C [22-25]. The receivers are restricted to operate below the thermal degradation temperatures otherwise, heat losses increase significantly with increasing absorber temperature. Limiting PTSC absorber's temperatures to below 400^o C, affects most high temperature applications.

A recently reported high temperature selective coating material is used in Archimede Solar Energy (ASE) HEMS08 receiver. This is the latest and world's most advanced solar receiver tube, designed for thermodynamic solar power plants, operating at high temperature (up to 550^{o}C) with molten salts as Heat Transfer Fluid (HTF)[23]. However, complications of thermal stresses arise with increased operating temperatures. Thermal stresses on the glass cover can be reduced by reducing its Infrared absorption. A hot mirror coating on the glass cover inner surface helps by reflecting IR radiation thereby cooling the glass cover surface [26].

1.2 Research Justification

Maximum attainable efficiency in a heat to work conversion system is limited by the ideal Carnot efficiency. In existing parabolic trough solar receivers, the selective coating is placed on the absorber surface and is therefore, directly subjected to absorber temperatures. Consequently, the thermal degradation temperature of the coating material becomes an upper operation limit for the receiver. In this study, this limit is raised. The hot mirror material is placed on the inner surface of the glass cover. Since the absorber temperature is much higher than the glass cover temperature, the HTF can be heated to higher temperatures before the coating material thermally decompose. High efficiencies can thus be achieved in heat engines. Higher temperatures mean greater capacity for generating mechanical work. Figure 1.4 illustrates the justification.

Introducing a hot mirror would not only help reduce heat losses, but also accelerate introduction of direct steam generation system (DSG) due to raised PTSC operating temperatures. In a DSG, water is heated in the solar receivers to generate steam directly and used to drive turbines for electricity generation. Such a system eliminates the costly HTF, heat exchanger unit and other HTF looping pipes as illustrated in Figure 1.5 (b).

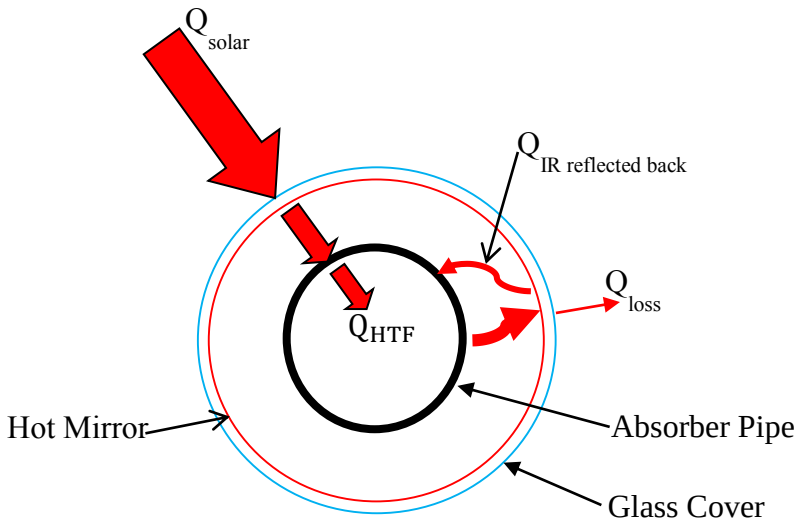

Figure 1.3: Schematic of hot mirror reflections to reduce heat losses in a receiver cross section

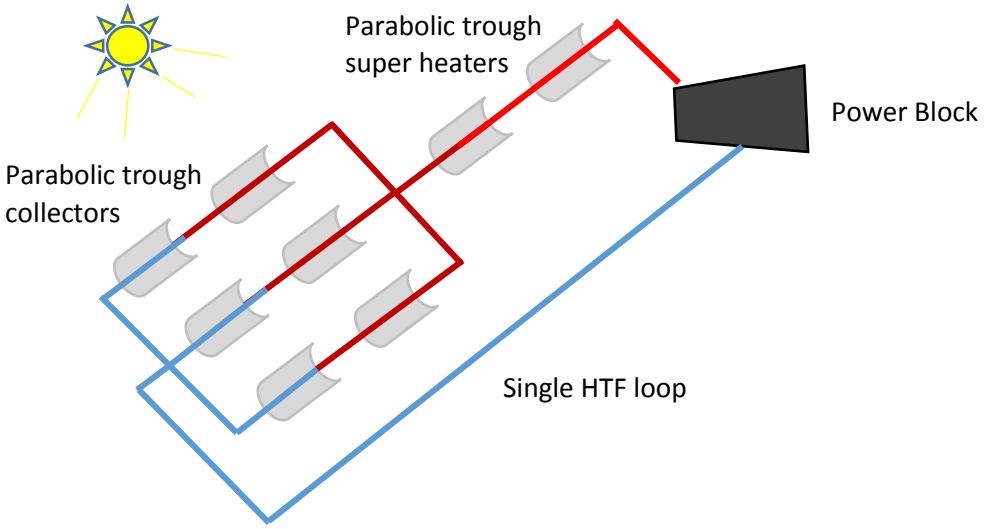

(a)

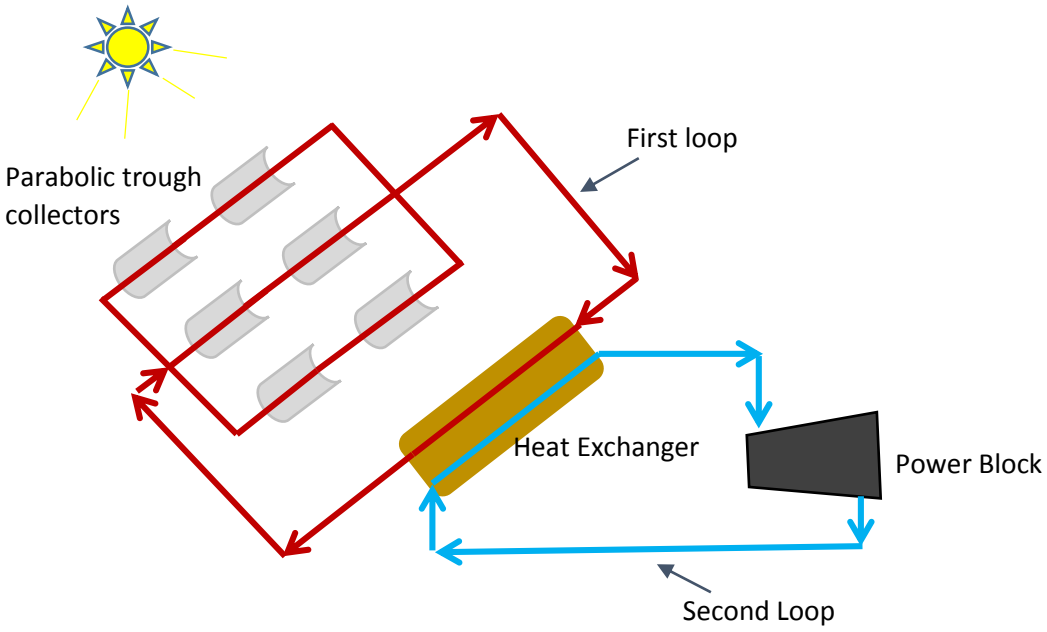

(b)

Figure 1.4: Illustration of a plant layout for (a) direct steam generator (DSG) (b) HTF based steam generator

1.3 Research Organization

Chapter 1: This is the introductory chapter. A general background to the study is presented. The context and objectives are highlighted. The problem is defined and research justification explained.

Chapter 2: Chapter 2 is the literature review. The basic theories of solar radiation, concentrating solar power and selective coating materials are explained. Some previous works done in improving the performance of a parabolic solar receiver are also presented here.

Chapter 3: Chapter 3 describes how the theoretical model was developed

Chapter 4: Chapter 4 describes the thermal processes' calculations in the hot mirror receiver.

Chapter 5: The chapter describes simulation and the flow of the algorithm.

Chapter 6: The chapter describes the results

Chapter 7: The discussion and conclusions are described in this chapter.

Chapter 2 Literature Review

2.0 Introduction

Parabolic trough solar collectors are so far the most successful and mature concentrating solar power technology on the market [27]. Improvements to their performance play a vital role in solar energy utilization. Many studies have been conducted through experiments and /or simulations to better understand the factors that affect the optical and thermal processes.

The PTSC heat collection element (HCE), commonly known as receiver, has been the center of the many studies. Improvements on it have a huge bearing on the cost of generated electricity in the SEGS. The development of models for different receiver conditions has resulted in increased comprehension of the performance processes.

In this chapter, a description of the PTSC HCE and models developed to characterize its performance are presented. However, it is imperative to present first, the nature of solar radiation. The principles of solar energy conversion in a PTSC HCE can best be understood by knowing the nature of solar radiation. The use of hot mirror materials, herein called hot mirror, for energy conservation is also reviewed.

2.1 Nature of Solar Radiation

Solar radiation arrives on the earth's surface in form of electromagnetic waves or as parcels of energy called photons. The properties of this radiation are conveniently discussed by starting with a blackbody theory, whose emitted spectrum - known as the Planck spectrum is uniquely defined if the absolute temperature an emitting surface is known [19, 20, 27]. The spectral blackbody emissive power distribution is defined by Planck's law as below (equation 1) [27]:

$$B_\lambda(T) = \frac{(2\pi hc^2)}{\lambda^5\left(e^{\frac{hc}{k}/\lambda T} - 1\right)} \qquad 1$$

Where: $c = 2.998 \times 10^8$ m/s the speed of light in a vacuum, $h = 6.6252 \times 10^{-2}$ J the Planck's constant, $k = 1.3806 \times 10^{-23}$ J/K Boltzmann constant, T is the absolute temperature of a blackbody in Kelvin.

Electromagnetic waves of different wavelengths carry different amounts of energy and based on their characteristics, the waves are grouped into different categories (Figure 2.1). For a given temperature, a peak of the Planck distribution occurs. This wavelength is found from Wien's displacement law (Equation 2) [27].

$$\lambda_{max} = \frac{2897.8}{T} \qquad 2$$

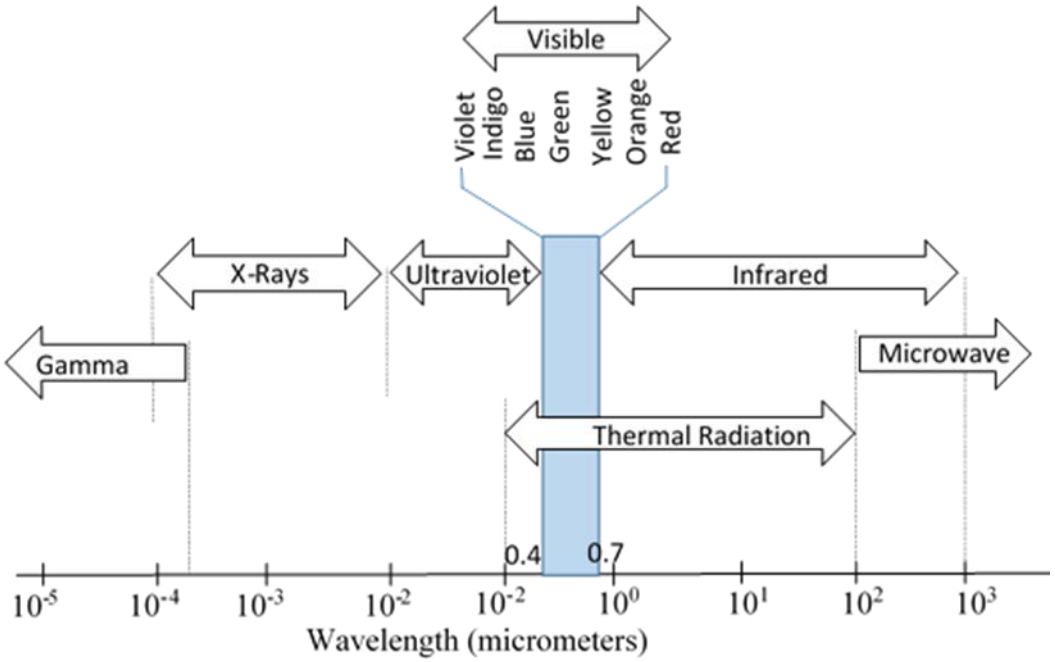

Figure 2.1: Electromagnetic wave spectrum (radiation traveling through vacuum) [19]

The wavelengths of importance in solar energy and its applications are from 0.3 µm to approximately 2.5 µm [19,28]. The spectral distribution of the emission from the sun's surface follows Planck's spectrum according to equation (1). This surface is modelled as a black body at a temperature of approximately 5780K [28].

The total solar flux emitted by the sun can be found by integrating Planck's distribution curve shown by the dotted line in Figure 2.3. Using Stefan-Boltzmann law [28], it follows:

$$F_{sun\ total} = \int_0^\infty \varepsilon B_\lambda(T) d\lambda = \sigma T^4 \qquad 3$$

Where; $\varepsilon = 1$ (the emissivity for a blackbody), $\sigma = 5.67 \times 10^{-8}$ W/m^{2}K^4 (The Stefan-Boltzmann constant)

The total solar flux towards the earth decreases proportionally to the square of the sun-earth distance. Solar energy flux reaching the earth's atmosphere is called the total solar irradiance (G_o). This extraterrestrial radiation (G_o) reaching the earth can be determined using equation 4[28].

$$G_o = F_{sun\ total} \times \left(\frac{4\pi {R_{sun}}^2}{4 {r_{sun-earth}}^2} \right) \qquad 4$$

where; $r_{sun\text{-}earth} = 1.5 \times 10^{11}$m (the average sun to earth distance), $R_{sun} = 6.69 \times 10^8 m$ (the average sun radius)

A solar constant is defined from the total solar irradiance (Figure 2.2). The solar constant G_s is the energy from the sun per unit time received on a unit area of surface perpendicular to the direction of propagation of the radiation at mean earth-sun distance outside the atmosphere.

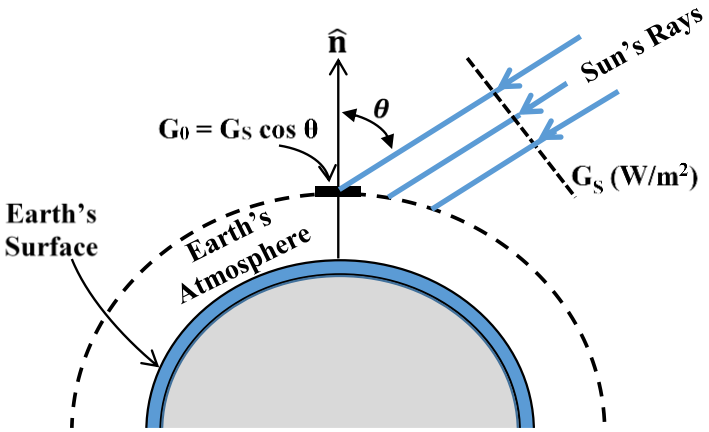

Figure 2.2: Extraterrestrial Radiation G_o on the outer atmosphere [28]

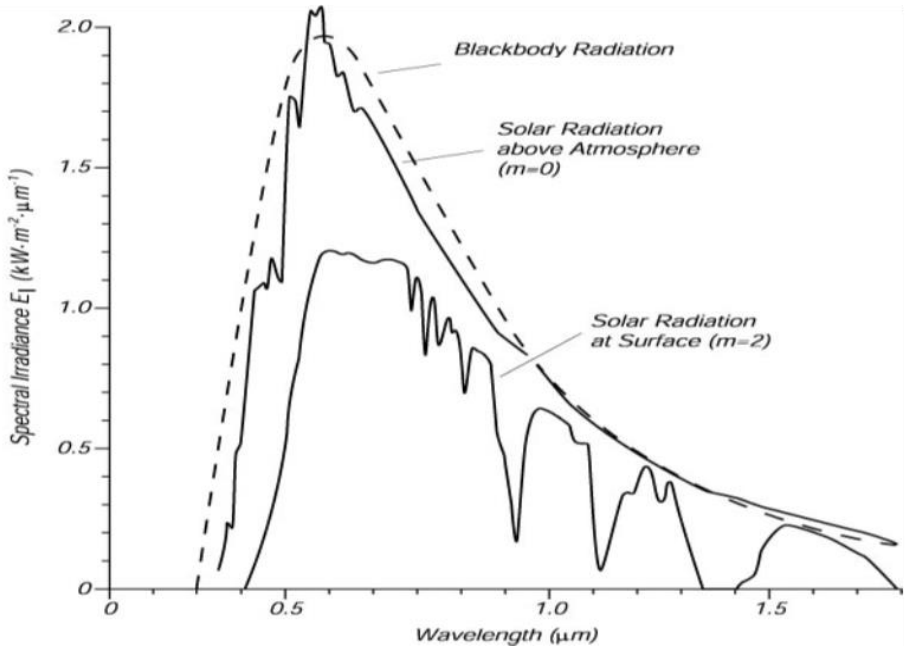

Figure 2.3: Solar Radiation irradiance at the top of the atmosphere and at the sea surface on a clear day [29]

As mentioned earlier, the amount of solar energy available on the earth's surface is significantly less than what is available above the outer atmosphere. The spectral distribution of solar radiation on the ground plotted in Figure 2.3 shows that the solar radiation undergoes considerable attenuation as it passes through the atmosphere.

Incoming solar radiation experiences changes both in directional distribution and in spectral distribution due to absorption and scattering as it passes through the atmosphere [30,31]. Solar energy incident on a surface on earth can be either direct or diffuse. The direct portion, generally referred to as direct normal irradiance (DNI) is the solar radiation directly from the sun that would strike a solar collector surface perpendicularly. On the other hand, diffuse part is the radiation assumed to reach a solar collector surface uniformly from all directions after undergoing scattering or reflections by air molecules and many other kinds of particles such as dust, smog, and water droplets suspended in the atmosphere. The variation of diffuse radiation can be between 10% and 100% of the total solar radiation, which is what causes regional

changes in ground level irradiance as well as temporal changes with shifting atmospheric components [28]. Direct normal irradiance (DNI) can be predictably used for concentrated solar thermal applications [32].

2.2 Solar Geometry

The geometric relationships between a plane of any particular orientation relative to the earth at any time (whether that plane is fixed or moving relative to the earth) and the incoming beam solar radiation, that is, the position of the sun relative to that plane, can be described in terms of the following angles [33].

- Latitude (φ), the angular location north or south of the equator, north positive; $-90^\circ \leq \varphi \leq 90^\circ$
- Declination (δ), the angular position of the sun at solar noon (i.e., when the sun is on the local meridian) with respect to the plane of the equator, north positive; $-23.45^\circ \leq \delta \leq 23.45^\circ$

$$\delta = 23.45 \sin\left(360 \times \frac{(284 + n)}{365}\right) \quad (5)$$

where n is the n^{th} day of a year

- Hour angle (ω), the angular displacement of the sun east or west of the local meridian due to rotation of the earth on its axis at 15^o per hour; morning negative, afternoon positive

$$\omega = 15 \times (ST - 12) \quad (6)$$

where ST is the solar time in hours.

The conversion clock time or local standard time (LST) to solar time (ST) requires knowledge of the location's longitude, the day of the year, and local standard meridian

as in equation 7 [33]. Note the local standard meridian is the longitude on which local standard time or clock time is based[14].

$$ST = LST + 4 \times (L_{st} - L_{loc}) + ET \quad (7)$$

where;

$$ET = 9.87 \sin 2B - 7.35 \cos B - 1.5 \sin B \quad (8)$$

$$B = \left(\frac{360}{365}\right)(n - 1) \quad (9)$$

In addition to the three basic angles; hour angle, latitude and sun's declination angle, several other angles are used to define the sun's position in the sky relative to a surface as shown in Figure 2.4.

- Slope (β), the angle between the plane of the surface in question and the horizontal; $0^\circ \leq \beta \leq 180^\circ$ ($\beta > 90^\circ$ means that the surface has a downward-facing component.)
- Surface azimuth angle (γ), the deviation of the projection on a horizontal plane of the normal to the surface from the local meridian, with zero due south, east negative, and west positive; $-180^\circ \leq \gamma \leq 180^\circ$.
- Angle of incidence (θ), the angle between the beam radiation on a surface and the normal to that surface.
- Zenith angle θ_z, the angle between the vertical and the line to the sun, that is, the angle of incidence of beam radiation on a horizontal surface.
- Solar altitude angle α_s, the angle between the horizontal and the line to the sun (that is the complement of the zenith angle).
- Solar azimuth angle γ_s, the angular displacement from south of the projection of beam radiation on the horizontal plane. Displacements east of south are negative and west of south are positive.

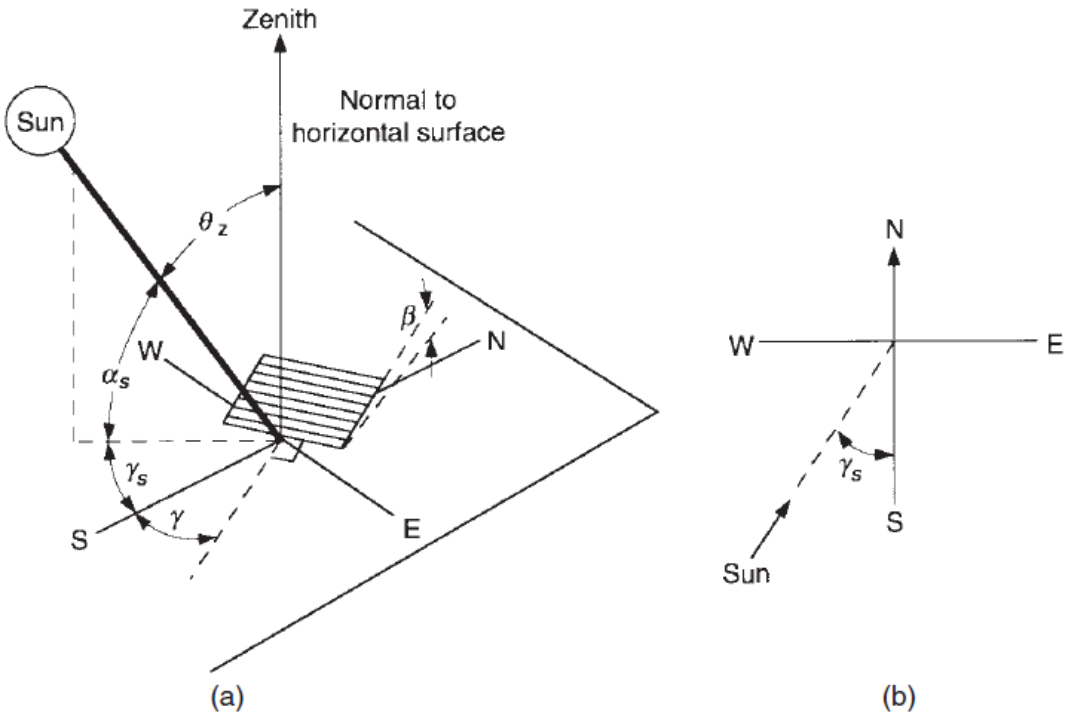

Figure 2.4: (a) Zenith angle, slope, surface azimuth angle, and solar azimuth angle for a tilted surface. (b) Plan view showing solar azimuth angle[8, 33]

2.3 Tracking Incoming Solar Energy

Some solar collectors ‘‘track’’ the sun by moving in prescribed ways to minimize the angle of incidence of direct (beam) radiation on their surfaces and thus maximize the incident beam radiation. The angular geometric relations of the suns path are well known. The sun’s path is irregular and depends on parameters such as latitude, time of day and day of the year. It is described by the solar altitude and solar azimuth angles. A general relationship of the incidence angle for beam radiation with all earlier mentioned solar geometric angles exists [8] (equation 10).

$$\cos\theta = \sin\delta\sin\varphi\cos\beta - \sin\delta\cos\varphi\sin\beta\cos\gamma + \cos\delta\cos\varphi\cos\beta\cos\omega + \cos\delta\sin\varphi\sin\beta\cos\gamma\cos\omega + \cos\delta\sin\beta\sin\gamma\sin\omega \quad (10)$$

There are several commonly occurring cases for which Equation 10 is simplified. For horizontal surfaces, the angle of incidence is the zenith angle of the sun, θ_z. Its value

must be between 0◦ and 90◦ when the sun is above the horizon. For this situation, β = 0 and equation 10 become [8]:

$$\cos\theta_z = cos\ \varphi\ cos\ \delta\ cos\ \omega\ +\ sin\ \varphi\ sin\ \delta \qquad 11$$

Tracking systems are classified by their motions. Rotation can be about a single axis (which could have any orientation but which in practice is usually horizontal east-west, horizontal north-south, vertical, or parallel to the earth's axis). Alternatively, rotation can be on two axis. This is full tracking. Full tracking, tracks the sun path in two directions, and is therefore the most efficient, although often costly to implement.

2.4 The Parabolic trough Solar Collector Receiver

In a parabolic trough solar collector, parabolic shaped mirrors reflect solar radiation onto a linear receiver located on the focus of the parabola as explained in chapter 1 and shown in Figure 1.3(a). The receiver is composed of an absorber pipe enclosed in a tubular glass cover (Figure 2.6). The interim space between the absorber pipe and the glass cover is evacuated to reduce heat losses through convection. The glass cover is highly transparent to the incident solar radiation. A heat transfer fluid (HTF) flows through the absorber pipe carrying with it heat which can be used directly or in heat exchangers. The heat is transferred to the HTF through conduction across the walls of the absorber pipe and also through convection to the HTF raising its internal energy.

The basis of the selective absorber approach in solar energy collection is to develop a surface which is strongly absorbing over the solar spectrum but non-absorbing at longer wavelengths. The "ideal" absorption curve of a selective absorber is illustrated in Figure 2.6. By using a solar collector surface with an absorption curve such as that in Figure 2.6, solar radiation is highly absorbed. At the same time, the absorptivity and therefore its emission (by Kirchhoff's laws) at longer wavelengths is low [19]. This helps to reduce heat losses occurring as a result of long wavelengths emissions.

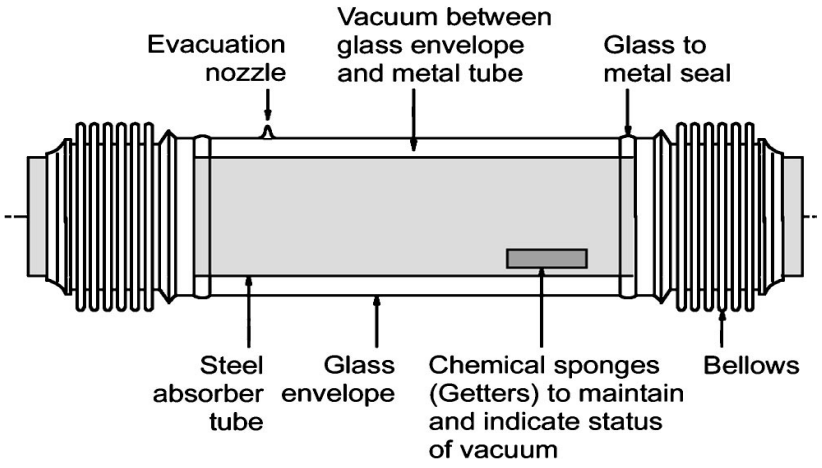

Figure 2.5: A typical receiver unit of a PTSC [34]

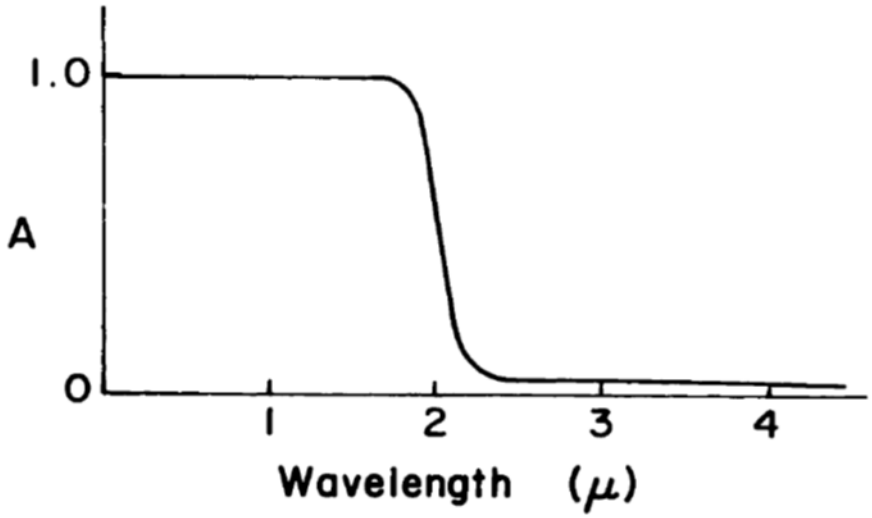

Figure 2.6: Ideal selective absorber surface absorption curve [35]

2.4.1 Models of PTSC Receiver

Presently, the key issues on improving the performances of PTSC receiver have attracted attention and thus many studies implemented. Dudley et al. developed a 1D model of the LS2 physical model [36]. With their accompanied experimental work, they derived performance correlations relating collector efficiency and thermal loss to working fluid temperature by simple polynomial correlation of the test data. An

incidence angle modifier was also developed by measuring the efficiency of the collector for a range of incidence angles. The experimental work has since become a blueprint for simulation validation. They demonstrated a superior performance of Cermet over Chrome black as absorber selective coatings. Chrome black and Cermet selective coatings were studied together with three receiver configurations: glass envelope with vacuum or air in the receiver annulus, and a bare receiver tube.

To overcome the operation temperature constraint of conventional receivers, Bader et al. [37] used a 2D validated heat transfer model to investigate numerically a tubular cavity receiver that uses air as a heat transfer fluid. They determined possible an efficient operation at up to 500^{o}C.

Garcia-Valladares et al. [38] investigated the influence of geometric structures of the receiver on the system's thermal efficiency. They developed a single pass model and extended it in order to simulate PTSC receiver with counter flow concentric circular heat exchangers (double-pass). It was demonstrated numerically that the double pass configuration enhanced the thermal efficiency compared with a single-pass PTSC receiver.

Pei et al. [39] proposed an innovative parabolic trough solar receiver that employs two solar selective coatings with different properties placed at different locations on the outer surface of the absorber. They developed a novel double-selective-coated receiver with two kinds of solar selective absorbing coatings based on the spectrum parameter model of radiation heat transfer. Two coatings with different spectral properties were considered plated on corresponding surfaces of the receiver with and without concentrated light spots. Heat loss simulation results showed that the double-selective-coated receiver reduced heat loss and boosted the collecting efficiency significantly compared with PTR70 receiver. When the temperature of absorber was 500^{o}C, the double-selective-coated receiver reduced heat loss by 157.8 W/m and increased the collecting efficiency from 64.7% to 68.1%. The System Advisor Model annual simulation results indicated that double-selective-coated receivers decreased the levelized cost of electricity of concentrating solar plants from 2.78% to 7.34%, and

increase electricity production from 2.94% to 8.21% compared with traditional PTR70 receivers.

Risi et al. [40] proposed an innovative transparent PTSC working with gas based nanofluids as HTF. They developed a mathematical model considering the geometrical, thermal and fluid dynamic aspects of the transparent PTSC in order to obtain global performance. A genetic algorithm optimization (MOGA II) was used to improve and optimize the performance of the solar collector. The simulation showed a thermal efficiency of 62.5%. They also reported a nanofluid temperature of about 650°C.

Various other studies developed models characterizing the processes in PTSC receiver and thus predict performance. Forristal R. et al. [41] developed a heat transfer model, both a 1D and a two-dimensional model (2D), implemented in Engineering Equation Solver (EES) that could be used to evaluate new and current HCE designs. Price et al. analyzed the effect of receiver vacuum on the thermal losses and receiver glass temperature. They found that the glass cover temperature can be informative about thermal losses from the receiver. The glass cover temperature can be used to detect deterioration of the heat collecting element, such as due to lost vacuum. Cheng et al. [42] developed a three-dimensional numerical model by combining the MCRT Method and the FLUENT software. They conducted three typical testing conditions to validate the model. Their simulation results showed good agreement with experiments. Edenburn [43] has done a performance study on cylindrical parabolic collector by comparing theoretical evaluation with the experimental result. Hachicha et al. [44] proposed a numerical model based on the finite volume method (FVM) to predict the solar radiation distribution on the receiver and the thermal processes. Men et al. [45] developed a 3D optical and thermal model for a tubular receiver in a PTSC. They used the finite volume method to describe the heat transfer processes on the active heat exchanging surfaces of the receiver.

Ratzel et al. [46] analyzed heat losses in the annular space of a receiver. Three configurations were considered: evacuation, oversizing annular space with Rayleigh

numbers kept below 1000 and use of gases with low thermal conductivity. They used an IR camera to measure the glass temperature.

Further PTSC improvement efforts have been made through the proposed direct steam generation (DSG) as a development of the SEGS. Odeh et al. [47] proposed a direct steam generation collector (DSG) in order to eliminate the costly synthetic oil, intermediate heat transport piping loop and oil to stream heat exchanger. A theoretical performance model was developed by Abengoa Solar [48] to be used in the design of DSG commercial plants. Abengoa Solar built, operated, and evaluated a demonstration plant of 8 MWht. This was used to validate the reliability of the theoretical model. Kalogirou et al. [49] analyzed a low pressure steam generation system which is based on heating water in a PTC and then flashing to steam in a separate vessel. The flow in the solar PTC is maintained in the liquid phase region. The works on DSG are efforts to use direct steam generation (DSG) inside parabolic troughs in order to achieve higher HTF temperatures and global efficiencies.

2.5 Hot Mirror Application

The Optical properties that are of primary interest for most solar materials are transmittance (τ), reflectance (ρ), absorptance (α) and emittance (ε). These properties characterize how a particular coating or a material interacts with incident energy. Furthermore, radiation characteristics of surfaces can be changed completely by applying thin layers of coatings on them. By definition, spectral transmittance (τ_λ) is the ratio of incident radiation transmitted through a medium at wavelength λ, to that of the total incident radiation at (λ). Spectral reflectance (ρ_λ) is the ratio of incident radiation reflected from the medium at wavelength λ, to the total incident radiation at λ. Spectral absorptance (α_λ) is the ratio of incident radiation absorbed in the medium at wavelength λ, to the total incident radiation at same wavelength (λ).

Hot mirror (herein called hot mirror) or low emittance coatings play a significant role in solar thermal conversion, transparent insulation for architectural windows and photovoltaic conversion. A hot mirror is defined as a coating that is predominately

transparent over the visible wavelengths (0.3 to77microm) and reflective in the infrared wavelengths (2.0-100microm) [50]. The fundamental principle is basically the wavelength difference between incoming solar radiation and thermal radiation emitted by surfaces [51]. Many studies and works have been done to exploit the wavelength differences in energy conservation. Lambert C. et.al. [52] demonstrated two scenarios of applying hot mirror coatings for space air conditioning. The first is the use of hot mirror cooling in a warm climate in which the hot mirror coating, allowed only transmission of visible energy through a window, with the remainder of the wavelengths reflected. Secondly, the hot mirror was used for winter heating. Thermal infrared were reflected back into a building space. In this process the majority of the solar energy could be utilized for passive solar gain and day lighting. Winegarner [53] demonstrated the significancy of a hot mirror in solar conversion systems. An efficiency increase for a flat plate solar collector with a hot mirror coating applied to the inside surface of a glass cover was reported. The solar conversion efficiency for the hot mirror system was reported as 43% compared to 33% for a selective absorber system. The net result of applying a hot mirror coating on the inside surface of the glass cover is to efficiently absorb solar energy and poorly emit infrared energy, much as a selective absorber does. Jarvinen R.M. [54] showed that the use of hot mirrors in large solar cavity receivers can increase system efficiency by 20% to 30%. Levin P. et al [55] presented to the Lawrence Berkerley laboratories of the department of energy in USA, the potential hot mirror characteristics of their unique transparent electrically conductive plastic designated by a trade name Intrex. Placed on a PET substrate, its IR reflectivity was 86% for type 18 and 71.7% for type 42, IR transmissivity 0% for type 18 and 85% for type 42 and absorptivity of 13.4% (type 18) and 27.4% (type 42).

Selkowitz S. et.al. [56] made a review of the progress on the development of transparent hot mirror applications in the 1970s. They observed that depending on applications, cost savings of about 25% to 75% were possible to achieve by 1980s. A recent review was made by Granqvist C.G. et al. [57]. They made a survey of works on spectrally selective coatings. Karlsson B. [58], Ribbing C.C. [59] and Valkonen E. [60] studied the

solar optical properties of thin films of noble metals (gold, Silver) and transition metals. Their results suggested the transition metals have poorer selective properties than noble metals. They also concluded that Gold has the best properties for a coating which transmits visible solar radiation but reflects infrared radiation.

Hamberg I. [61] and Granqvist C.G., studied the doped semiconductor Indium Tin Oxide (ITO). They reported that ITO is highly transparent for shortwave lengths and highly reflective for long wave lengths. Lampert C.M [62] studied scientific properties of optical materials and coatings in a broad range. The study suggested that hot mirrors applied as heating-load hot mirrors can be used as an alternative to selective absorbers in solar thermal collectors.

Hot mirror coatings are classified as below:

Thin metal layers [63]. A good IR reflector can be made by depositing on the glass substrate a thin metal film, made of a metal with a low IR emissivity, such as silver, gold, copper, or aluminum. However, to obtain a good IR reflectivity (>80%), the solar transmissivity of a simple metal layer becomes quite limited (less than 40%).

Doped semiconductors with an appropriate band gap [63]: With respect to metal films, doped semiconductor thin layers have usually a lower IR-reflective coefficient (usually less than 85%) but they have a better transparency for the visible light (up to 80%). A 200nm film of Indium Tin Oxide (In_2O_3: Sn) has a solar transmissivity of about 80%, with an IR-reflective coefficient of 75%.

Composite layers (Multiple layers) [63]: The solar transmissivity of a metal thin film can be increased using a material with high refractive index as an antireflective layer. Composite layers are usually made by a thin noble metal layer between transparent dielectric layers. The solar transmissivity can be increased above 70%, but the realization is more difficult, since different layers of accurately controlled thickness must be deposited. For this reason, this solution is probably more expensive and technically difficult.

Chapter 3 Methodology to a hot mirror model

3.0 Introduction

In this chapter, the development of a theoretical model for a hot mirror receiver is presented. Non-uniform concentrated solar radiation is considered incident on the receiver unit. This is a distribution produced using the semi-analytical formulation by Jeter [64]. The fundamental principle of the model is energy conservation on the discretized control volumes. Radiative heat fluxes are treated as boundary conditions on the control volume surfaces. It is thus important to describe and derive mathematical expressions for the dominant heat fluxes influencing heat transfer. Mathematical expressions that relate the geometric and material properties of the hot mirror receiver and the heat transfer are derived. This paves way for developing a consistent thermal model.

3.1 Description of the heat fluxes

Heat flux on a receiver unit, under steady state conditions, can be described with the help of Figure 3.1. Concentrated solar energy is incident on the glass cover (GC) as ($\dot{q}_{G,sol}$) and on the absorber pipe (AP) as $\dot{q}_{A,sol}$. The GC has high transmittance in incoming solar radiation while the AP has high absorptance. They both increase in temperature thereby emitting IR radiation: $\dot{q}_{AG,IR}$ (from AP to GC), $\dot{q}_{GA,IR}$ (from GC to AP), $\dot{q}_{GG,IR}$ (from GC to GC) and $\dot{q}_{GO,IR}$ (from GC to the outside (O)).

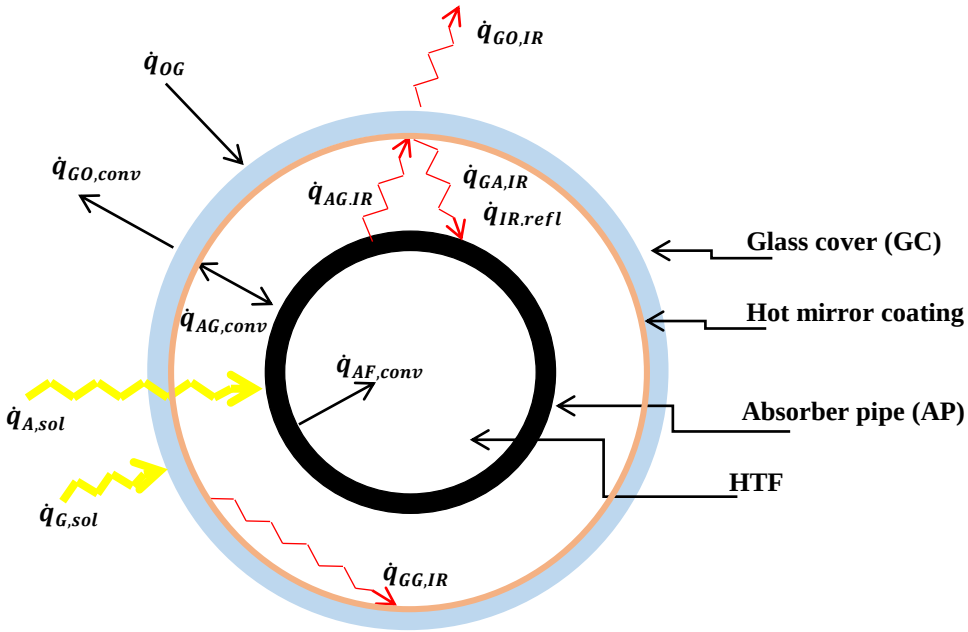

Figure 3.1: Heat fluxes on a receiver unit (Cross section)

The GC exchanges radiation with the environment. Radiation from the environment, $\dot{q}_{OG,IR}$ impinged on GC. With a hot mirror on the inner side of GC, IR radiation from AP is reflected back onto itself via the IR reflecting surface on the GC as $\dot{q}_{IR,refl}$. Due to its importance, details of the back reflected IR radiation, $\dot{q}_{IR,refl}$ are given in chapter 4.

Some energy absorbed by AP is transferred to the HTF by convection as ($\dot{q}_{AF,conv}$). Through the same process, heat is transferred from the GC to the outside as ($\dot{q}_{GO,conv}$) and between AP and GC. However, due to a vacuum in the annulus space, convection transfer between AP and GC was negligible.

Conduction played mainly a role between neighbouring control volumes of different temperatures on the AP and GC as explained in section 3.3. However, conduction was neglected in support fixtures (structural support members anchoring the receiver unit).

3.2 Discretization of the receiver unit

In order to include the non-uniform solar flux distribution around the circumference of the receiver, the AP, GC and HTF were discretized into control volumes (CV). In this way, heat transfer is evaluated at a number of surface segments. The finite volume method (FVM) was used with each CV's temperature represented by the center temperature. CV surface temperatures were thus interpolated from the center temperature. Figure 3.2 illustrates the discretization of the receiver unit. Part (a) shows CVs along the longitudinal direction while part (b) shows the CVs along the circumference.

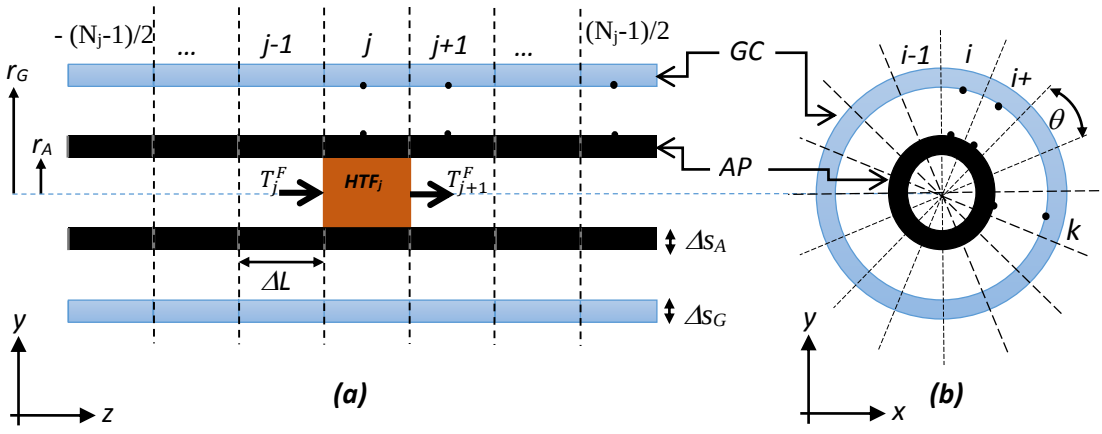

Figure 3.2: Discretization of the absorber pipe, glass cover and heat transfer fluid

Upon discretization, the number of resulting segments on the GC and AP was N_i and each CV was labeled by the integer i with $\frac{-(N_i-1)}{2} < i < \frac{(N_i-1)}{2}$ along the circumference (azimuthal direction, Figure 3.2 (b)), and N_j segments along its axis (longitudinal direction Figure 3.2 (a)) identified by the integer j where $\frac{-(N_J-1)}{2} < j < \frac{(N_J-1)}{2}$.

Figure 3.2 (a) illustrates the discretization of the HTF. This was done along the axial direction only. The CVs or segments labeled by the integer j. The thermal analysis along the azimuthal direction and along the axial direction created a basis for a 3D analysis of the receiver unit.

3.3 Heat flux interactions

With the receiver unit discretized, it is easy to analyze the heat fluxes using small segments. Figure 3.3 is an extract of a CV from the cross sectional view of a discretized receiver unit (Figure 3.2 (b)). It illustrates the heat flux interactions on both the AP and GC.

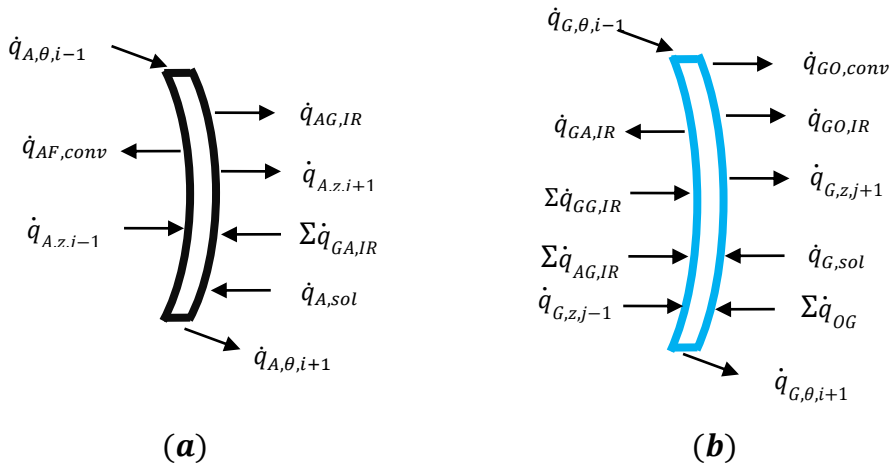

Figure 3.3: Heat exchange terms on (a) absorber pipe (AP) and (b) glass cover (GC)

3.3.1 Conduction heat transfer

Referring to Figure 3.3, only the following heat fluxes, $\dot{q}_{A,\theta,i\pm1}$, $\dot{q}_{G,\theta,i\pm1}$, $\dot{q}_{A,z,j\pm1}$ and $\dot{q}_{G,z,j\pm1}$, need introduction. They denote conductive heat transfers on for a CV i, on both the AP and GC, with its neighboring CVs along the azimuthal (θ) and axial (z) direction. Each direction has a pair for a CV thus representing both heat in-and outflow. Contribution from the conduction terms in the axial direction i.e. $\dot{q}_{A,z,j\pm1}$ and $\dot{q}_{G,z,j\pm1}$ is relatively small. This is because the temperature gradient along the axial direction between consecutive segments ($j-1$, j and $j+1$) is quite small [63, 64]. Therefore these small flux contributions were ignored and heat conduction through the pipe wall (AP) and the glass cover (GC) was considered only in the azimuthal direction between i and its immediate neighboring elements *i-1* and *i+1*.

All the conductive terms on a CV *i* on the AP along the azimuthal direction were summed up to get a resulting conductive term $\dot{q}_{A,\theta}$. The sum can be written as:

$$\dot{q}_{A,\theta} = \dot{q}_{A,\theta,i-1} + \dot{q}_{A,\theta,i+1} \quad (15)$$

Equation 15 can be rewritten using the Fourier law of conduction heat transfer [65]. It defines the rate of heat conducted in a medium as being proportional to both, the medium's cross sectional area which is perpendicular to the direction of heat flow, and the temperature change with respect to a length in the direction of heat flow [65]. It is expressed as:

$$Q = -kA\left(\frac{dT}{dx}\right) \quad (16)$$

where *Q* is the rate of heat transfer, *k* is the material thermal conductivity, *A* is the cross sectional area and $\frac{dT}{dx}$ is the temperature gradient in the direction of heat flow. It thus follows that equation 15 can be rewritten as:

$$\dot{q}_{A,\theta} = k_A\left(\frac{T_i^A - T_{i+1}^A}{\left(r_A + \frac{\Delta s_A}{2}\right)\theta}\right)\Delta s_A \Delta L + k_A\left(\frac{T_i^A - T_{i+1}^A}{\left(r_A + \frac{\Delta s_A}{2}\right)\theta}\right)\Delta s_A \Delta L \quad (17)$$

or

$$\dot{q}_{A,\theta} = k_A\left(\frac{2T_i^A - T_{i+1}^A - T_{i-1}^A}{\left(r_A + \frac{\Delta s_A}{2}\right)\theta}\right)\Delta s_A \Delta L \quad (18)$$

The sum of conductive terms for the GC is similar to the equation 15. For a CV *i* on GC, it can be written as:

$$\dot{q}_{G,\theta} = \dot{q}_{G,\theta,i-1} + \dot{q}_{G,\theta,i+1} \quad (19)$$

and rewritten as:

$$\dot{q}_{G,\theta} = k_G\left(\frac{\left(2T_i^G - T_{i+1}^G - T_{i-1}^G\right)}{\left(r_G + \frac{\Delta s_G}{2}\right)\theta}\right)\Delta s_G \Delta L \quad (20)$$

where; $k_{material}$ is material thermal conductivity (AP and GC), $T_i^{A\ or\ G}$ is the temperature of the i^{th} CVs' center point (on AP or GC) and the remaining symbols are as defined in Figure 3.2. A close approximation for small CV size ($<r_A$) was that the temperature varies linearly between centers of neighboring CVs. The CV size are small enough for this linear approximation.

Conduction heat transfer rate for the AP and GC surfaces can thus be described by Equations 18 and 20 respectively.

3.3.2 Convection heat transfer

In a parabolic trough solar receiver, convective heat transfer occurs between the AP and the HTF, and from the GC to the outside. As mentioned, convection in the annulus space can be considered negligible due to existence of a vacuum. By definition, heat transfer through a fluid is by convection in the presence of bulk fluid motion [28,]. The rate of convection heat transfer is observed to be proportional to the temperature difference and is conveniently expressed by Newton's law of cooling [65, 66] as:

$$Q = hA(T_s - T_f) \qquad 21$$

Where h is convection heat transfer coefficient, A is heat transfer surface area, T_s is temperature of the surface and T_f is temperature of the fluid sufficiently far from the surface.

Convection heat transfer from AP into the HTF occurred on a CV labeled "*ij*" on AP into a segment labeled "*j*" of HTF. The HTF segment "*j*" received the convective heat from as many CV, around a circumference on AP where CV "*ij*" was, as there were. Therefore, from equation 21, convection heat transfer from one CV "*ij*" is as follows:

$$\left(\dot{q}_{AF,conv}\right)_{ij} = h_f[r_A\theta\Delta L]\left(T_{ij}^A - T_j^F\right) \qquad 22$$

where T_{ij}^A is the average temperature of the CV "*ij*" on AP, T_j^F is the average HTF temperature at segment "*j"* and the quantity in square brackets is the area of the CV in thermal contact with the HTF.

From literature, the convective heat transfer coefficient (h_f) is defined by a dimensionless parameter, the Nusselt number, (Nu_{r_A}) [65, 66] which depends on the physical properties of the fluid and the physical situation. It represents the relative contribution of convection and conduction to heat transfer in a fluid. When a fluid is in motion, heat transfer in a fluid involves convection. When a fluid is motionless, it involves conduction. Thus the Nusselt number represents an enhancement of heat transfer through a fluid as a result of convection relative to conduction. It is expressed as [65]:

$$Nu = \frac{q_{conv}}{q_{cond}} = \frac{h\Delta T}{\left(k\,{}^{\Delta T}/_{L}\right)} = \frac{hL}{k} \quad (23)$$

Many empirical formulations exist. The closest formulation for the Nusselt number for a non-uniformly heated fluid flow inside a pipe is given by the Gnielinski correlation [67].

$$Nu_{r_A} = \left(\frac{B}{2}\right)\left(\frac{Pr(Re-1000)}{\left(1+12\sqrt{\frac{B}{8}}\left(Pr^{2/3}-1\right)\right)}\right)\left(\frac{Pr}{Pr_w}\right)^{0.11} \quad (24)$$

where $B = \frac{1}{(1.82\log_{10}(Re)-1.64)^2}$ and *Re* and *Pr*, the Reynolds and Prandtl number, respectively. Pr_w is the Prandtl number taken at the wall temperature.

In this relation, the *Nu* number is a function of temperature through the Reynolds and Prandtl numbers' temperature dependence.

The Prandtl number describes the relative thickness of the velocity and thermal boundary layers in a flow over a heated or cooled surface [68]. In such a flow, both the velocity and thermal boundary layers will develop simultaneously. Velocity boundary layer describes a thickness of a fluid in which the effects of viscous shearing forces caused by the fluid viscosity are felt. It is a perpendicular distance from the surface at which the fluid velocity $u = 0.99u_\infty$, where u_∞ is the free stream velocity. Similarly, the thermal boundary layer is a distance from a surface over which a fluid flows, at which the temperature difference $T - T_s$ equals $0.99(T_\infty - T_s)$ where T_s is the surface temperature and $T_\infty$is the free stream fluid temperature.

As such the Prandtl number is used to describe the effect on the convective heat transfer rate of the velocity boundary layer relative to the thermal boundary layer. It is expressed as below.

$$Pr = \frac{\upsilon}{\alpha_h} \quad (25)$$

where ν is the molecular diffusivity of momentum and α_h is the molecular diffusivity of heat.

In terms of the Nusselt number, the convective heat transfer coefficient (h_f) is:

$$h_f = \frac{Nu_{r_A} \cdot k_A}{2r_A} \quad (26)$$

A simplification for the fluid temperature is that each HTF CV is at the fluid bulk temperature obtained at any specific location. Recalling that equation 22 gives the convective heat transferred to the HTF segment from one AP CV, the contribution of heat from all the AP CVs on a circumference where CV "*ij*" lies is simply the sum of energy from all the CVs on the AP circumference. Thus, the total convective heat transfer into the HTF segment *j* from all CVs across the circumference is the sum:

$$\left(\dot{q}_{AF,conv}\right)_j = \sum_{i=1}^{N_i} h_f[r_A\theta\Delta L]\left(T_{ij}^A - T_i^F\right) \quad 27$$

Considering convective heat transfer between all CVs across the circumference of the GC surface and the environment, an equation similar to equation (27) was used. This is stated in terms of the GC properties as:

$$\left(\dot{q}_{GO,conv}\right)_j = \sum_{i=1}^{N_i} h_w[(r_G + \Delta s_G)\theta\Delta L]\left(T_{ij}^G - T^O\right) \quad 28$$

with T_{ij}^G the average CV temperature on the GC, T^O the ambient temperature and h_w is the heat transfer coefficient with wind as the fluid. It is given by the following correlation [69]:

$$h_w = 4{v_w}^{0.58} \times (2(r_G + \Delta s_G))^{-0.42} \quad 29$$

where v_w is the wind velocity. All other quantities are as defined in Figure 3.2.

Equations 27 and 28 were the derived expressions for convection heat transfer for the AP to HTF and GC to the environment respectively.

3.3.3 Radiation transfer

Heat losses in an evacuated parabolic trough solar receiver from the AP to the GC and environment eventually occur through radiation heat transfer. It is as a result of emissions from a surface at some absolute temperature. The rate of heat emission given by the Stefan-Boltzmann law [19, 70] is:

$$Q = \varepsilon\sigma A T^4 \quad 30$$

where ε is the surface emissivity, σ is the Stefan–Boltzmann constant ($5.67\text{x}10^8 \text{W/m}^2\text{K}^4$) and *T* is the absolute temperature of the surface in K

To describe the radiative heat exchange between surfaces, it is important to know the total heat energy emanating from each surface and the angle in space through which

the radiation is intercepted by other surfaces or the exchanging surfaces' relative orientation.

Surfaces in radiative contact not only exchange their emitted radiation but also exchange some incidence radiation that they reflect in the direction of the other surfaces. This is accounted for by the Radiosity concept [19], i.e. the total radiation emanating from a surface due to its emissions and reflection of incident radiation.

$$J = \varepsilon\sigma A T^4 + \rho H \qquad 31$$

where ρ is the surface coefficient of reflection and H is the incidence radiation.

The angle in space through which emitted radiation is incepted by another surface is called the solid angle. It gives to rise to the concept of "the view factor". This is a fraction of energy that strikes an intercepting surface directly from the source surface [19, 70]. View factor is a geometric function that can be describes as below.

In geometries that can be modelled as infinitely long, such as ducts and channels, an approximation of the view factor can be made using an approach called the Hottel's crossed string method [27, 28]. Such Geometries can be considered infinitely long when they are very long in one direction relative other directions. Figure 3.3 illustrates the method.

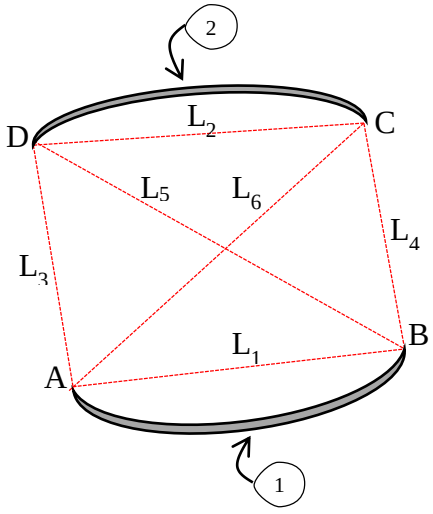

Figure 3.4: Hottel's crossed string method [28]

Hottel's crossed string method involves drawing uninterrupted lines across faces of emitting surfaces and joining the endpoints with the straight lines. View factor approximation by the Hottel's crossed-strings method can be expressed in terms of the string lengths as:

$$F_{1\to2} = \frac{\sum(crossed\ string\ lengths) - \sum(uncrossed\ string\ lengths)}{2 \times (string\ on\ surface\ 1\ length)} \quad 32$$

In the study, the parabolic trough solar receiver was considered as infinitely long [44]. The AP and GC are irradiated by both visible and IR radiation and their material properties were characterized in terms of these radiation types. The cut-off wavelength for visible and IR was chosen at 900nm.

Radiation exchange within the receiver surfaces involved each AP CV radiatively interacting directly with the GC CVs and the AP CV exchanging with other AP CVs via IR reflections on the hot mirror. The CV surfaces on the AP were assumed diffuse and gray, while the GC was gray and a specular reflector to incoming IR radiation, due to the hot mirror coating on the surface facing the AP.

To determine the effective radiation exchange, a net radiation method [19] was applied on each CV. A view factor notation was defined as F_{kl}^{MN}. This is described as the view factor from CV "*k*" of material "M" to CV "*l*" of material "N". Material M and N can be the AP or GC. The view factor values were approximated by the Hottel's crossed string method. Uninterrupted connection lines between the faces of the CVs were drawn to define the method.

Net radiation on the absorber pipe (AP)

With the heat fluxes on the AP surfaces known, it is now possible to determine the net radiation on any one CV on the AP. A CV on the AP (CVAP) intercepts solar radiation $\left(\dot{q}_{A,sol}\right)_{ij}$ as well as IR radiation $\left(\Sigma\dot{q}_{GA,IR}\right)_{ij}$ (see Figure 3.1 or 3.3(a)). The IR consists of the three components: thermal radiation from the CVGCs, and the singly and doubly reflected radiations. Due to the AP geometry, all $F_{kl}^{AA} = 0$, meaning no CVAP directly imparts radiation onto any other CVAP. The radiation incident on the CVAP labeled "*ij*" is

$\left(\dot{q}_{A,sol}\right)_{ij} + \left(\Sigma\dot{q}_{GA,IR}\right)_{ij}$

where the $\left(\dot{q}_{A,sol}\right)_{ij}$ is given by a predetermined profile [64] and

$$\left(\Sigma\dot{q}_{GA,IR}\right)_{ij} = \sum_{l=1}^{N_i} F_{li}^{GA} R_{lj}^{G} + \left(\dot{q}_{IR,1\,refl}\right)_{ij} + \left(\dot{q}_{IR,2refl}\right)_{ij} \quad 33$$

where R_{lj}^{G} is purely the thermal radiation originating from CVGC "*lj*" along the circumference. Thermal radiation originating from control volumes along the axial direction diminished with increasing length due to the cosine effect, (i.e., cosine of large angle tend to zero). As such, they are small compared to the leading term ($<10^{-6}$) in the above summation (equation 33) and were neglected.

The non-trivial single and double reflection terms $\left(\dot{q}_{IR,1\,refl}\right)_{ij}$ and $\left(\dot{q}_{IR,2refl}\right)_{ij}$ are discussed in detail in the chapter 4.

From the radiosity concept, the radiation emanating from the CVAP, $\left(\dot{q}_{AG,IR}\right)_{ij}$, which consists of its own thermal radiation and reflected portions of the incoming radiation can be expressed as:

$$J = R_{ij}^{A} + \rho_{A,sol}\left(\dot{q}_{A,sol}\right)_{ij} + \rho_{A,IR}\left(\Sigma\dot{q}_{GA,IR}\right)_{ij} \quad 34$$

with $\rho_{A,sol}$ and $\rho_{A,IR}$ the coefficients of reflection for solar and IR respectively.

The net absorbed radiation by the CV on the AP is therefore

$$\left(\dot{q}_{RAD,A}\right)_{ij} = -R_{ij}^{A} + \left(1-\rho_{A,sol}\right)\left(\dot{q}_{A,sol}\right)_{ij} + \left(1-\rho_{A,IR}\right)\left(\Sigma\dot{q}_{GA,IR}\right)_{ij} \quad 35$$

with outgoing radiation defined as negative.

Net radiation on glass cover (GC)

A CV on the GC (CVGC) is irradiated by solar radiation, $\dot{q}_{G,sol}$, IR radiation from the AP, $\Sigma\dot{q}_{AG,IR}$, IR radiation from other parts of the GC $\Sigma\dot{q}_{GG,IR}$ and radiation from the environmental background $(\Sigma\dot{q}_{OG})_{ij}$ (see Figure 3.1 or 3.3(b)). This is written

$$\left(\dot{q}_{G,sol}\right)_{ij} + \left(\Sigma\dot{q}_{AG,IR}\right)_{ij} + \left(\Sigma\dot{q}_{GG,IR}\right)_{ij} + (\Sigma\dot{q}_{OG})_{ij}$$

Specifically, the term $\left(\Sigma\dot{q}_{AG,IR}\right)_{ij}$ consists of the sum of thermal radiation from CVAP,($\sum_{l=1}^{N_i} F_{li}^{AG} R_{lj}^{A}$), and radiation which originated from a different CVAP, and was reflected once off the GC and once off the AP, $\left(\dot{q}_{IR,2G,refl}\right)_{ij}$:

$$\left(\Sigma\dot{q}_{AG,IR}\right)_{ij} = \sum_{l=1}^{N_i} F_{li}^{AG} R_{lj}^{A} + \left(\dot{q}_{IR,2G,refl}\right)_{ij} \quad 36$$

Further,

$$\left(\Sigma\dot{q}_{GG,IR}\right)_{ij} = \sum_{l=1}^{N_i} F_{li}^{GG} R_{lj}^{G} \quad 37$$

where R_{lj}^{A} and R_{lj}^{G} is the thermal radiation originating from CVs "*lj*" along the circumference of the AP and the GC. The reflection term $\left(\dot{q}_{IR,2G,refl}\right)_{ij}$ is discussed in chapter 4.

The incoming radiation from the environment is $(\Sigma\dot{q}_{OG})_{ij} = \sum_{l=1}^{N_i} F_{li}^{OG}\sigma\delta A_O\left(T_{ij}^{O}\right)^4$, where the environment is considered to be the boundary of a large black body cavity

(ε_o= 1) at temperature T_{ij}^{O}, and at the same distance as the collector reflecting surface [41]. Thermal interactions with materials closer by, such as the ground or the collector, are neglected.

The outgoing radiation of the CVGC includes thermal radiation emitted to the AP and the environment, as well as reflected radiation i.e.

$$R_{ij}^{G} + (\rho_{G,sol})\dot{q}_{G,sol} + \rho_{G,IR}\left[\left(\Sigma\dot{q}_{GG,IR}\right)_{ij} + \left(\Sigma\dot{q}_{AG,IR}\right)_{ij} + \left(\Sigma\dot{q}_{OG}\right)_{ij}\right]$$

The GC reflection coefficients are given by $\rho_{G,sol}$ and $\rho_{G,IR}$ for solar and IR respectively. The net radiation from a CV on the GC is therefore:

$$\begin{aligned}\left(\dot{q}_{RAD,G}\right)_{ij} = &-R_{ij}^{G} + \left(1-\rho_{G,sol}\right)\dot{q}_{G,sol} \\ &+ \left(1-\rho_{G,IR}\right)\left[\left(\Sigma\dot{q}_{GG,IR}\right)_{ij} + \left(\Sigma\dot{q}_{AG,IR}\right)_{ij} + (\Sigma\dot{q}_{OG})_{ij}\right]\end{aligned} \qquad 38$$

Equations 35 and 38 were the derived expressions for the net radiative heat transfer for CVs on the AP and on GC respectively.

Chapter 4 Derivation of the Hot Mirror effect

4.0 Introduction

In the previous chapter, net radiation exchange for any CV on the absorber pipe (AP) and glass cover (GC) were expressed as equations 35 and 38. Chapter four presents a derivation of the first and second IR reflection terms. In equation 33, the term $\left(\Sigma \dot{q}_{GA,IR}\right)_{ij}$ contains the first reflection effect $\left(\dot{q}_{IR,1\,refl}\right)_{ij}$ and the second IR reflection effect $\left(\dot{q}_{IR,2refl}\right)_{ij}$ of the hot mirror. Similarly, the term $\left(\Sigma \dot{q}_{AG,IR}\right)$ in equation 36 consists of the second IR reflection effect $\left(\dot{q}_{IR,2G,refl}\right)_{ij}$. These hot mirror effects are a crucial aspect in a system with a hot mirror coating on the inside GC. In what follows, the following assumptions were made:

- CVs are approximately flat, (the CV size is small enough for the approximation to hold).
- IR radiation is reflected maximally twice before absorption and that the hot mirror optical properties are approximately constant for the temperature range of interest (the more the IR undergoes reflection, the less significant its intensity gets).

4.1 Hot Mirror Effect - The first Reflected Infrared Radiation Term $\left(\dot{q}_{IR,refl}\right)_{ij}$

A CV A_{ij} on the AP receives specularly reflected IR radiation that was emitted by another element A_{kl} on AP further along the AP. As mentioned, the first IR reflection occurs on the GC. Determining the amount of radiation received by CV A_{ij} on the AP from A_{kl} on AP helps to sum the IR contributions from all the CVs in radiative contact with A_{ij},.

Radiation emission from a surface towards an intercepting area depends on radiation intensity I, the projection of the emitting area with respect to the intercepting area and the solid angle. Using Figure 4.1, emitted radiation q_{rad} from δA_A to another area δA_G is given by [19, 65, 66]

$$q_{rad} = I\delta A_A \cos(\alpha)\left[\frac{\delta A_G \cos(\beta)}{d^2}\right] \qquad 39$$

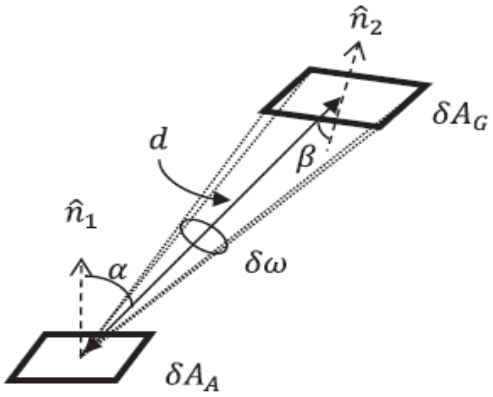

Figure 4.1: Illustration of the emitting and absorption areas and associated angles

with $\delta\omega = \frac{\delta A_G \cos(\beta)}{d^2}$, and angles α , β and the distance d as shown in Figure 4.1. Further, $\hat{n}_1$ and $\hat{n}_2$ are unit normals to the areas δA_A and δA_G, respectively. The radiation intensity I for an emitting unit surface is defined as [19, 65, 66]

$$I = \frac{\varepsilon\sigma}{\pi} T^4, \qquad 40$$

where ε is the emissivity, σ the Stephan Boltzmann constant and T the absolute average temperature of the radiation emitting area.

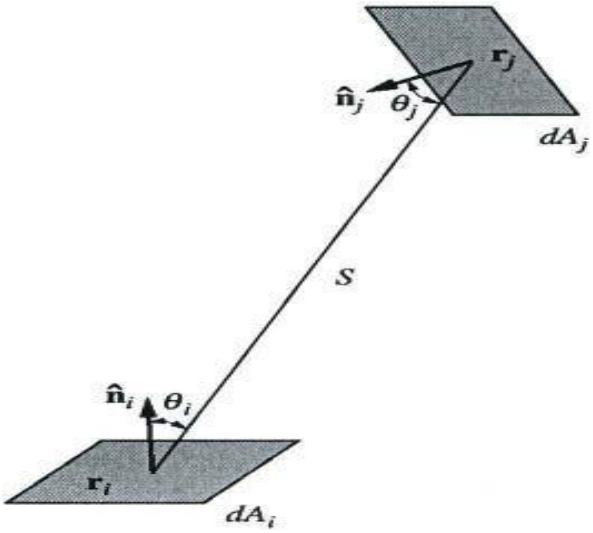

Figure 4.2: Illustration of Radiation exchange between two surfaces[19]

Radiation exchange between surfaces is described using the view factor or form factor. Figure 4.2 illustrates radiation exchange between two infinitesimal surfaces. The total radiation leaving a surface δA_i into the hemispherical space above it is $J_{\delta A_i} = \pi I \delta A_i$. Similarly, the total radiation from surface δA_i intercepted by an area δA_j at a distance S is $J_{\delta A_j} = \frac{(I \cos\theta_i \cos\theta_j \delta A_i \delta A_j)}{S^2}$. Expressing the radiation intercepted by δA_j as a fraction of the radiation leaving δA_i, defines the diffuse view factor for the infinitesimal areas. This is as below:

$$dF_{\delta A_i - \delta A_j} = \frac{\cos\theta_i \cos\theta_j}{\pi S^2} \qquad 41$$

This formalism can be translated to the parabolic trough solar receiver situation. Inside a receiver unit, a CV labeled A_{kl} on the AP emits IR radiation, which is reflected off the GC and returns to a CV A_{ij}, on the AP, see Figure 4.2.

The area of A_{kl} is $\delta A_A = (r_A + \Delta s_A)\theta \Delta L$ (see Figure 3.2). The area on the GC (labeled $(\delta A_G)_{\left(\frac{i+k}{2}\right)\left(\frac{j+l}{2}\right)}$) reflecting the radiation is $(\delta A_G)_{\left(\frac{i+k}{2}\right)\left(\frac{j+l}{2}\right)} = r_G\left(\frac{\theta}{2}\right)\frac{\Delta L}{2}$, with center located halfway between the centers of A_{kl} and A_{ij} (Figure 4.2).

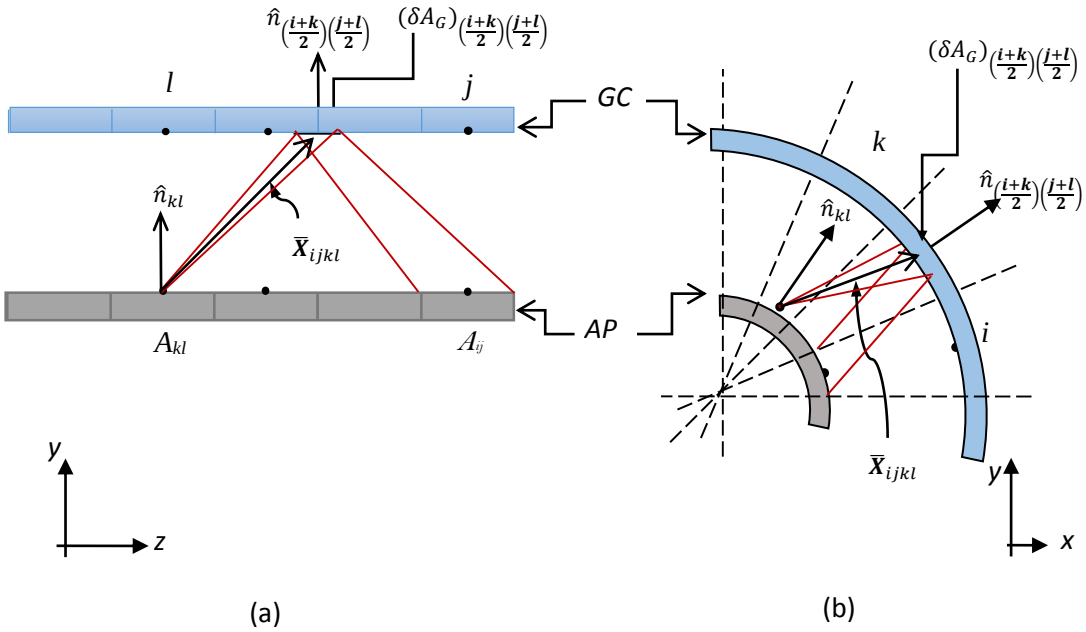

Figure 4.3: Illustration of IR reflection specularly off GC (a) Along axis (b) Side View

The cosine terms in equation (39) are determined by using the definitions

$$cos(\alpha) = \hat{X}_{ijkl} \cdot \hat{n}_{kl} \quad \text{and} \quad cos(\beta) = \hat{X}_{ijkl} \cdot \hat{n}_{\left(\frac{i+k}{2}\right)\left(\frac{j+l}{2}\right)}, \tag{42}$$

where $\hat{X}_{ijkl}$ is the unit vector along the emitted radiation from the centers of A_{kl} to $(\delta A_G)_{\left(\frac{i+k}{2}\right)\left(\frac{j+l}{2}\right)}$ and the angles are defined in Figure 4.1.

In Cartesian coordinates, the locations of the centers are (see Figure 4.3)

$$surface\ center\ of\ A_{kl} = \left((r_A + \Delta s_A)cos(k\theta), (r_A + \Delta s_A)sin(k\theta), l\Delta L\right) \tag{43}$$

$$surface\ center\ of\ (\delta A_G)_{\left(\frac{i+k}{2}\right)\left(\frac{j+l}{2}\right)} = \left(r_G cos(\left(\frac{i+k}{2}\right)\theta), r_G sin(\left(\frac{i+k}{2}\right)\theta), \left(\frac{j+l}{2}\right)\Delta L\right) \tag{44}$$

This allows construction of the vector $\bar{\boldsymbol{X}}_{ijkl}$ (see Figure 4.3)

$$\bar{\boldsymbol{X}}_{ijkl} = \left(r_G\, cos\left(\left(\frac{i+k}{2}\right)\theta\right) - (r_A + \Delta s_A)\, cos(k\theta)\ , r_G\, sin\left(\left(\frac{i+k}{2}\right)\theta\right) - (r_A + \Delta s_A)\, sin(k\theta)\, , \left(\frac{-l+j}{2}\right)\Delta L\right) \tag{45}$$

with length squared $\left|\bar{\boldsymbol{X}}_{ijkl}\right|^2$ (denoted d^2_{ijkl})

$$d^2_{ijkl} = [r_G]^2 + [(r_A + \Delta s_A)]^2 - 2(r_A + \Delta s_A) r_G\, cos\left(\left(\frac{i-k}{2}\right)\theta\right) + \left(\frac{j-l}{2}\right)^2 \Delta L^2 \tag{46}$$

Next, the unit vector $\hat{n}_{kl}$ is defined (see Figure 4.3) by

$$\hat{n}_{kl} = (\cos(k\theta)\, , \sin(k\theta)\, , 0)\ . \tag{47}$$

and similarly $\hat{n}_{\left(\frac{i+k}{2}\right)\left(\frac{j+l}{2}\right)}$ using the appropriate subscripts. Using equations (39) to (47), the IR radiation completely reflected from the element A_{kl} onto A_{ij} can be expressed as

$$\left(\left(\dot{q}_{IR,refl}\right)_{kl}\right)_{ij} = \frac{\frac{\varepsilon\sigma}{\pi}T_{kl}^4\left((r_A+\Delta s_A)\theta\Delta L\right)}{d_{ijkl}^4}\left(\frac{r_G\theta\Delta L}{4}\right)\left(\hat{X}_{ijkl}\cdot\hat{n}_{kl}\right)\left(\hat{X}_{ijkl}\cdot\hat{n}_{\left(\frac{i+k}{2}\right)\left(\frac{j+l}{2}\right)}\right) \quad 48$$

with T_{kl} being the absolute average surface-center temperature of the CV A_{kl}, and all other quantities defined as above. Equation 48 is developed on the assumption that the CV sizes are small enough to approximate the curved absorber surfaces as flat.

For radiation exchange involving specular surfaces, the specular view factor is expressed as a sum of the diffuse view factors with one contribution for each possible direct or reflection path. As such, equation (48) can be rewritten in terms of the specular form factor

$$(F^S)_{klij}^{AA} = \left(\frac{\delta A_G}{\pi d_{ijkl}^4}\right)\left(\hat{X}_{ijkl}\cdot\hat{n}_{kl}\right)\left(\hat{X}_{ijkl}\cdot\hat{n}_{\left(\frac{i+k}{2}\right)\left(\frac{j+l}{2}\right)}\right)$$

as

$$\left(\left(\dot{q}_{IR,refl}\right)_{kl}\right)_{ij} = (F^S)_{klij}^{AA}(\varepsilon\sigma[\delta A_A]T_{kl}^4) \quad 49$$

Equation (49) represents the thermal radiation emitted by A_{kl}, reflected perfectly by the GC and incident onto A_{ij}, i.e. AP to GC to AP. This is referred to as the first reflection. In the next section, this expression is summed to obtain the total incident IR radiation on A_{ij}.

4.2 Summation of all reflected contribution to A_{ij}

All CVs on the AP in radiative contact via reflection with A_{ij} will contribute towards its total received IR radiation, and these contributions must be added. This sum will be constructed next.

Along the axis, the reflections shown in Figure 4.3 (a) can occur for the entire length of the AP, hence summation should occur for all N_j segments. However along the circumference, not all CVs are in radiative contact with A_{ij} if only one reflection is considered. The "extremal ray" in Figure 4.4 shows the limit of which CVs can reflect once onto A_{ij}. The final CVs with which radiative contact via reflection is possible are labelled i-N_m and i+N_m, where the subscript stands for "maximal". Including reflection by A_{ij} onto itself, there are then $2N_m+1$ such elements along the circumference which will contribute to A_{ij} via single reflection.

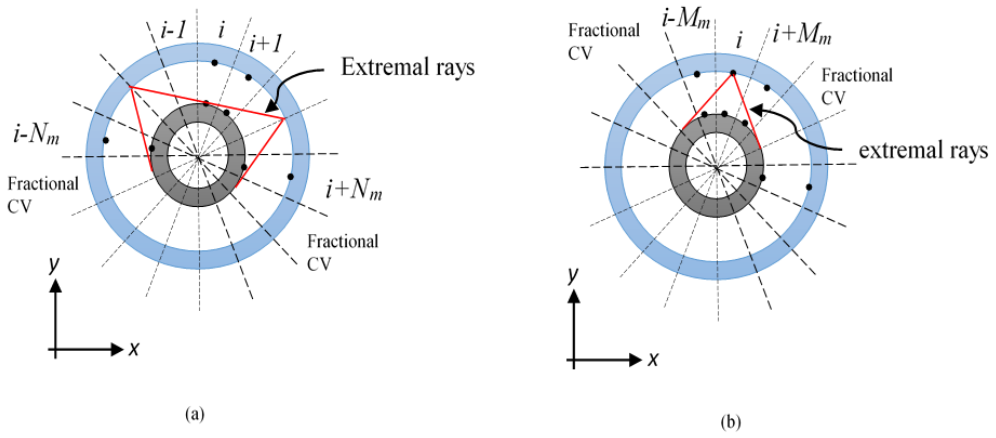

Figure 4.4: Extremal light rays illustrating the limits in which control volumes around the circumference can be in radiative contact with each other for (a) IR radiation reflected once off the GC and (b) IR radiation emitted by the GC.

The CVs at i-N_m-1 and i+N_m+1 are likely to only fractionally contribute (see the "fractional CV" in Figure 4.4. This is taken into account by adding fractional contributions, f ($0<f<1$), of those rows labelled i-N_m-1 and i+N_m+1 to the total IR radiation incident on A_{ij}. The CVs from those two fractionally rows are denoted $\left(\dot{q}_{IR,refl}\right)_{i+N_m+1,j}$ and $\left(\dot{q}_{IR,refl}\right)_{i-N_m-1,j}$ and defined by

$$F_{i+N_m\pm1,j} = f\left(\left(\dot{q}_{IR,refl}\right)_{i+N_m+1,j} + \left(\dot{q}_{IR,refl}\right)_{i-N_m-1,j}\right) \qquad 50$$

In total there are $(2N_m + 1)N_j$ complete radiation contributions and the two fractional rows incident on the CV, A_{ij}. The sum of all single reflection contributions on A_{ij} can be expressed as

$$\left(\dot{q}_{IR,1refl}\right)_{ij} = \rho_{G,IR}\left(\sum_{a=i-N_m}^{i+N_m}\sum_{b=1}^{N_j}\left(\left(\dot{q}_{IR,refl}\right)_{ab}\right)_{ij} + F_{i+N_m\pm1,b}\right). \qquad 51$$

4.3 Hot Mirror Effect - The second reflected infrared radiation term $\left(\dot{q}_{IR,2refl}\right)_{ij}$

The secondary reflection effects (AP to GC to AP to GC to AP) depend on the values of $\rho_{G,IR}$ and $\rho_{A,IR}$. As such these are included in the simulation. Multiplying equation 51 with the appropriate reflection coefficients yields the second hot mirror effect:

$$\left(\dot{q}_{IR,2refl}\right)_{ij} = \rho_{G,IR}\left(\sum_{a=i-N_m}^{i+N_m}\sum_{b=1}^{N_j}\rho_{G,IR}\rho_{A,IR}\left[\left(\sum_{c=a-N_m}^{a+N_m}\sum_{d=1}^{N_b}\left(\left(\dot{q}_{IR,refl}\right)_{cd}\right)_{ab} + F_{a+N_m\pm1,d}\right)_{ij}\right] + F_{i+N_m\pm1,b}\right) \quad 52$$

With expression for first reflection onto AP derived, the secondary reflections on the GC can now be considered, (AP to GC to AP to GC). Reflection of this type on CVGC "*ij*" is incident from all CVAP visible to it, from *i*-M_m, to i+M_m and the fractional contribution in Figure 4.4(b). Similarly to equation (51), it is given by

$$\left(\dot{q}_{IR,2G,refl}\right)_{ij} = \rho_{A,IR}\left(\sum_{a=i-M_m}^{i+M_m}\sum_{b=1}^{N_j}\left(\left(\dot{q}_{IR,1\,refl}\right)_{ab}\right)_{ij} + F_{i+M_m\pm1,b}\right) \quad 53$$

The equations (51) and (53) are important results. They provide the description of hot mirror reflections. They form a basis for the simulation of hot mirror systems and thus help to characterize PTSCs' performance especially in the high temperature regime operations.

Chapter 5 Numerical model for the hot mirror PTSC receiver

5.0 Introduction

In this chapter, the hot mirror PTSC receiver simulation is described. The model was implemented using Visual Basic code (see appendix A). The approach was based on an energy balance imposed on the receiver unit. It includes thermal losses from the HCE, optical losses and the energy gain in the HTF. These processes were applied on control volumes (CVs) as described in chapter three. An algorithm is presented for the sequences in which all the thermal processes and PTSC performance analysis was conducted.

By the time of the study, there is little information available on the theory and application of hot mirror in PTSC tubular receivers. As such, verification and validation of the simulation was done based on theory expectations in heat transfer analysis and on the works, both simulation and experimental, done on a PTSC with a selective coating on the absorber pipe (AP).

5.1 Hot mirror PTSC numerical model

Jeter's formulation [64] for concentrated solar irradiation distribution around a receiver unit was used to determine the solar flux on the outer surfaces of the AP and GC. As mentioned in chapter three, the finite volume method (FVM) was used to carry out a numerical analysis under steady state conditions. The AP and GC were discretized in the azimuthal direction while the HTF in the axial direction.

The heat transfer equations (18, 20, 26, 27, 33 and 36) mentioned in chapter three describe a result of respective heat transfer modes across any one control volume. For each CV on the AP and GC, these equations are incorporated in the energy balance equation of the form.

$$\left(\sum \dot{q}_{COND} + \sum \dot{q}_{CONV} + \sum \dot{q}_{RADtherm} + \sum \dot{q}_{sol}\right)_{ij} = 0 \qquad 54$$

Equation 54 enforces that, on any CV, the sum of the heat transfers is zero. Along the azimuthal direction, applying equation 54 space reduces to a form shown below.

For the AP (Refer to Figure 3.3 (a) in chapter 3)

$$0 = (\dot{q}_{A,\theta,i+1} + \dot{q}_{A,\theta,i-1}) + \dot{q}_{AF,conv} + (\dot{q}_{AG,IR} + \Sigma\dot{q}_{GA,IR}) + \dot{q}_{A,sol} \qquad 55$$

For the GC, (Refer to Figure 3.3 (b) in chapter 3)

$$0 = \dot{q}_{G,\theta,i-1} + \dot{q}_{G,\theta,i+1} + \dot{q}_{GO,conv} + \dot{q}_{G,sol} + \dot{q}_{GO,IR} + \Sigma\dot{q}_{AG,IR} + \dot{q}_{GA,IR} +$$

$$\Sigma\dot{q}_{OG} + \Sigma\dot{q}_{GG,IR} \quad (56)$$

For each receiver surface, (AP and GC), the above equations resulted in a set of algebraic equations of the 4th order where temperature and the heat fluxes were coupled. This means that for a selected number of CVs N=100 both on the AP and GC, there were 100 new equations of the form as shown below.

For the AP:

$$k_A \frac{2T_{ij}{}^A - T_{i+1j}^A - T_{i-1j}^A}{\left(r_A + \frac{\Delta s_A}{2}\right)\theta}\Delta s_A \Delta L + h_f[r_A \theta \Delta L]\left(T_{ij}^A - T_j^F\right) - R_{ij}^A + \left(1 - \rho_{A,sol}\right)\left(\dot{q}_{A,sol}\right)_{ij} + \left(1 - \rho_{A,IR}\right)\left(\sum_{l=1}^{N_i} F_{li}^{GA}\varepsilon\sigma A T^G{}_{lj}{}^4 + \rho_{G,IR}\left(\sum_{a=i-N_m}^{i+N_m}\sum_{b=1}^{N_j}\left(\left(\dot{q}_{IR,refl}\right)_{ab}\right)_{ij} + F_{i+N_m\pm1,b}\right) + \left(\dot{q}_{IR,2refl}\right)_{ij}\right) \quad (57)$$

For the GC:

$$k_A \frac{2T_{ij}{}^A - T_{i+1j}^A - T_{i-1j}^A}{\left(r_A + \frac{\Delta s_A}{2}\right)\theta}\Delta s_A \Delta L + h_f[r_A \theta \Delta L]\left(T_{ij}^A - T_j^F\right) - R_{ij}^A + \left(1 - \rho_{A,sol}\right)\left(\dot{q}_{A,sol}\right)_{ij} + \left(1 - \rho_{A,IR}\right)\left(\Sigma\dot{q}_{GA,IR}\right)_{ij} \quad (55)$$

These were linearized via a Taylor expansion to obtain a set (with N=100, the number selected from the grid dependency test in section 5.3) of discretized equations of the form [71]:

$$a_i T_i = a_{i+1} T_{i+1} + a_{i-1} T_{i-1} + b_i \quad (56)$$

where T_i is the temperature of the control volume of interest (i), $T_{i\pm1}$ are temperatures for the neighboring control volumes $(i \pm 1)$ respectively, a_i is the discretization coefficient for the control volume of interest (i), $a_{i\pm1}$ are the discretization coefficients for the neighboring control volume $(i \pm 1)$ respectively, and b_i is referred to as the source term[71].

The terms of equation (56) are defined as below.
For the AP:

$$a_i = k_A \frac{2 \times \Delta s_A \Delta L}{\left(r_A + \frac{\Delta s_A}{2}\right)\theta} + h_f[r_A \theta \Delta L] + 4 \times \left(\varepsilon_A \sigma [\delta A_A] {T^*}_{ij}^3\right) - 4 \times (F^S)_{klij}^{AA} \left(\varepsilon_A \sigma [\delta A_A] {T^*}_{ij}^3\right) \quad 57$$

$$a_{i+1} = a_{i-1} = \frac{\Delta s_A \Delta L}{\left(r_A + \frac{\Delta s_A}{2}\right)\theta} k_A \quad 58$$

$$b_i = \sum_{i=1}^{N_i} h_f[r_A \theta \Delta L] T_i^F - 3 \times \varepsilon_A \sigma \delta A_A {T^*}_{ij}^4 + \left(1 - \rho_{A,sol}\right)\left(\dot{q}_{A,sol}\right)_{ij} + \left(1 - \rho_{A,IR}\right)\left[\sum_{l=1}^{N_i} F_{li}^{GA} R_l^G - 3 \times \left(\dot{q}_{IR,1refl}\right)_{ij} + \left(\dot{q}_{IR,2refl}\right)_{ij}\right] \quad 59$$

For the GC:

$$a_i = k_G \frac{2 \times \Delta s_G \Delta L}{\left(r_G + \frac{\Delta s_G}{2}\right)\theta} + h_w[r_G \theta \Delta L] + 4 \times \sigma(\varepsilon_1[r_G + \Delta s_G] + \varepsilon_2 r_G) {T^*}_{ij}^3 \quad 60$$

$$a_{i+1} = a_{i-1} = \frac{\Delta s_G \Delta L}{\left(r_G + \frac{\Delta s_G}{2}\right)\theta} k_G \quad 61$$

$$b_i = \sum_{i=1}^{N_i} h_w[r_G \theta \Delta L] T^o + 3 \times \sigma(\varepsilon_1[r_G + \Delta s_G] + \varepsilon_2 r_G) {T^*}_{ij}^3 + \left(1 - \tau_{G,sol}\right)\left(\dot{q}_{G,sol}\right)_{ij} + \left(1 - \rho_{G,IR}\right)\left[\left(\Sigma F_{li}^{GG} \dot{q}_{GG,IR}\right)_{ij} + \left(\Sigma F_{li}^{AG} \dot{q}_{AG,IR}\right)_{ij} + \left(\Sigma F_{li}^{oG} \dot{q}_{OG}\right)_{ij}\right] \quad 62$$

T^* is the initial guessed temperature for a CV.

The energy balance applied on the HTF control volume j is described as:

$$\left(\dot{q}_{AF,conv}\right)_j = \dot{m}C_p\left(T_{j+1}^F - T_j^F\right) \quad 63$$

where $\dot{m}$ is the mass flow rate and C_p the specific heat capacity of the HTF .

The set of discretized equations (equation (56)) and equation (63) are coupled and solved through an iterative process to give a solution of the energy balance equations applied on the receiver surfaces. The temperature profile around the circumference and along the length of the receiver unit and HTF temperature along the length are among the outputs in the solution. This process is described in section 5.2. In the analysis, the following assumptions were made:

- The flow is assumed incompressible.
- The HTF control volumes were considered in the direction of flow.
- There is a linear temperature profile across the boundary surfaces of consecutive control volume. A piecewise linear profile approximation enables linear interpolation functions to be used for surfaces temperatures.
- Radiative fluxes are a surface phenomenon. The surfaces are so thin that absorption can be considered to occur on the surface.
- The absorber pipe surface emits and reflects diffusely.
- The glass cover is specular in IR reflection.

5.2 Description of algorithm

The general algorithm is illustrated in Figure 5.1. The simulation code was developed in Visual Basic with the following structure:

At preprocessing, the geometry and material properties of the PTSC are defined. At the inlet of the AP, a control volume of the HTF (CV_j) enters with a known fluid initial temperature T_j^F. It is bounded by a ring of CVs on the AP and the GC which encloses the vacuum space. An initial temperature T^* is guessed for all AP and GC CVs. T^* is initially guessed for each CV on the AP and GC to calculate the coefficients and constant in equation (56). These are described in terms of T^* in equations 57 to 62.
Equation 56 is solved iteratively for all the CVs on AP and GC rings. The first iteration produces new temperatures T_i for each CV, which serves as a new T^* for the next iteration. The program continues in this way until a convergence criterion $\frac{{T_i}^{n+1}-{T_i}^n}{{T_i}^n} < 10^{-6}$ is satisfied where the superscript *n* denotes the n^{th} iteration. Using the obtained temperatures T_i for each CV, the convection heat transferred into the HFT fluid is computed using equation (27) and the HTF exit temperature from CV *j=1* is determined. This serves as the entry (or known inlet) temperature for the next HTF CV (*j=2*). This process is repeated for the entire length of the receiver (*j=M).* The simulation code is shown in appendix A.

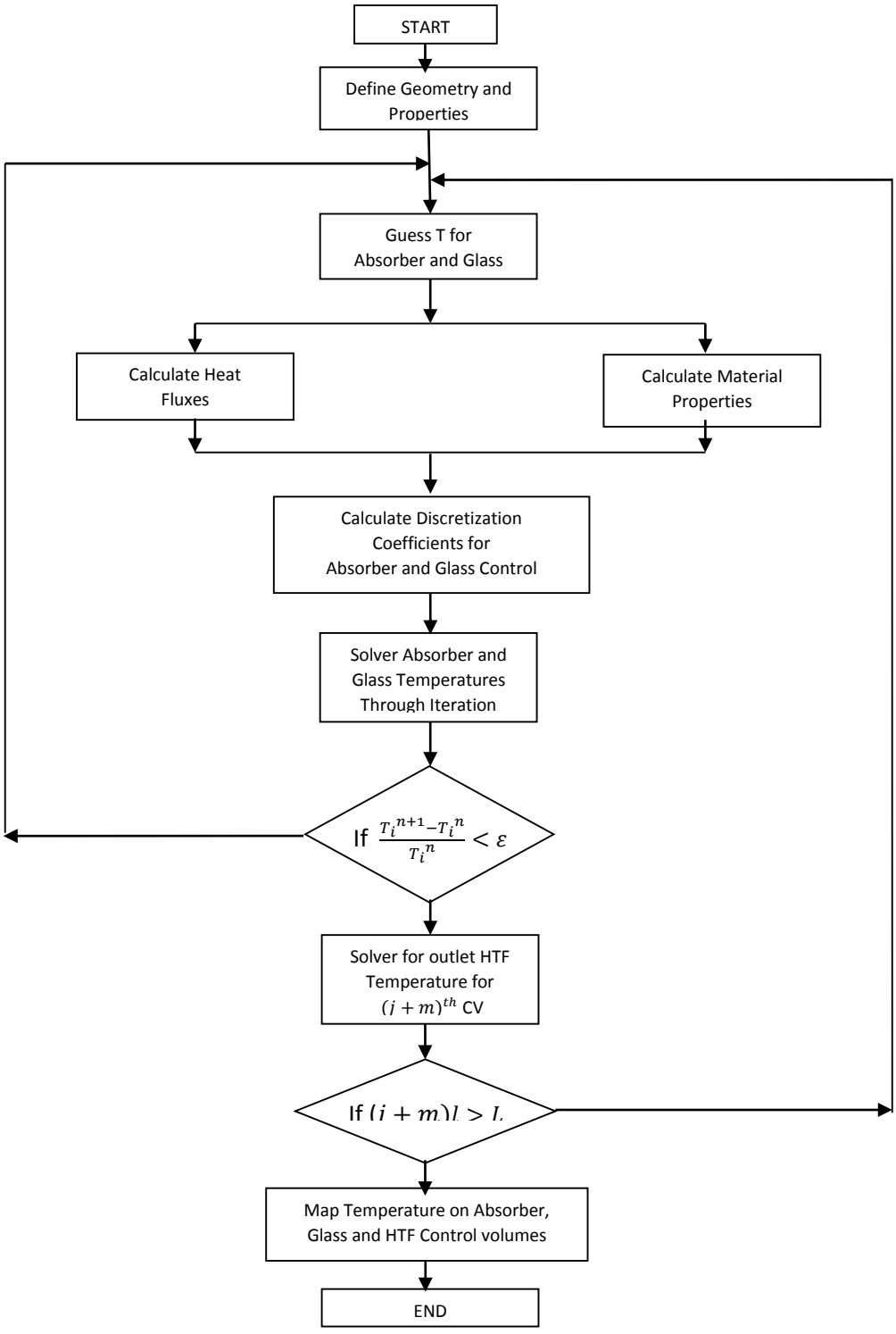

Figure 5.1: Illustration of the algorithm

5.3 Grid dependence Test and Validation

To ascertain a grid independent solution in the numerical model, a grid dependence test was conducted. The size of the CVs could influence results for the surface temperatures. Different sizes were tested by altering the number of CVs along the circumference. The size of a CV along the circumference can be determined from the following:

$$\theta_s = \frac{2\pi}{N} \qquad 64$$

By increasing N, the absorber and glass surfaces' temperature were observed as shown in Table 5.1. Number of divisions of the circumference was increased

Table 5.1: Surface Temperature Variation taken from the same point ($\theta = 0\ rad, x = 2m$) on the receiver length for different number of control volumes

N	1	5	10	50	55	60	70	75	80	90	95	100	105
θ_s	6.3E +00	1.3E +00	6.3E -01	4.2E -01	3.1E -01	2.5E -01	1.8E -01	1.6E -01	1.4E -01	1.1E -01	1.0E -01	9.7E -02	9.0E -02
ΔT	1.4E -02	2.7E -03	1.4E -03	2.7E -04	2.5E -04	2.3E -04	2.0E -04	1.8E -04	1.7E -04	1.5E -04	1.4E -04	1.4E -04	1.3E -04

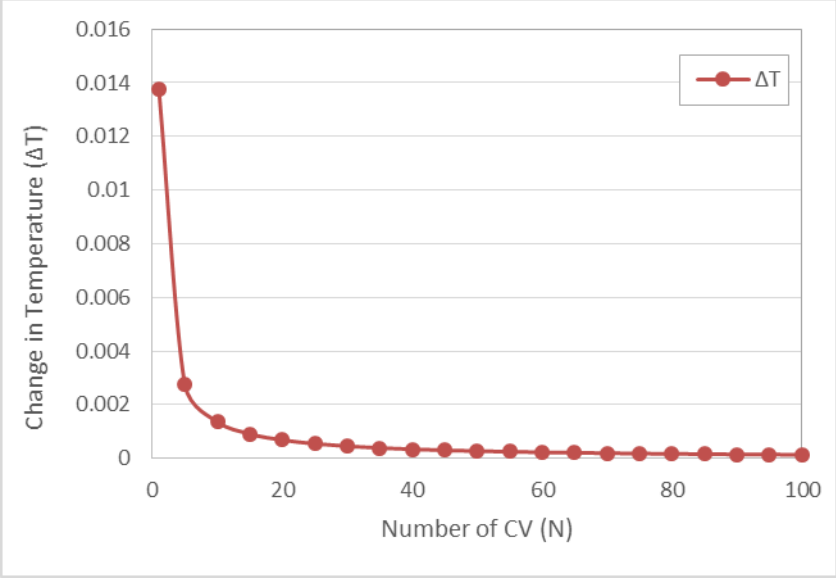

Figure 5.2: Grid dependence test: Change in HTF Temperature with increasing Number of CVs

A number of more than 100 CVs along the azimuthal direction and $\Delta L = 1m$ for the axial segment size gave CV sizes for which the absorber and glass surfaces' temperature results changed insignificantly ($\Delta T = 0.0001^{o}$). Thus a 100 CVs grid along the azimuthally and ΔL =1m for the axial directions was chosen.

Due to the cosine diminishing effect, radiation emanating from control volumes further on the axial length, grid dependence test was not done for the axial length. This was because of the smaller temperature gradient in the axial direction and the diminishing contribution from axial segments. This meant that the axial size would not influence results. A unit length was adopted.

Model validation was undertaken using two approaches. Firstly, theoretical expectations were used by "switching off" (i.e. setting to zero) some parameters of the receiver model to validate the simulation. Comparisons are performed for the following cases: zero solar irradiation, zero absorber material conductivity and zero HTF convective heat transfer coefficient. Figure 5.3 (a) and (b) show the comparison results for the mentioned validation cases. The results conformed to theoretical expectations. The HTF is not expected to gain in energy in all the first three cases (Figure 5.3 (a)) whilst massive temperature rise for the HTF is expected when absorber emissivity losses are cut off (Figure 5.3 (b)). Details of the simulated system are in Table 5.2.

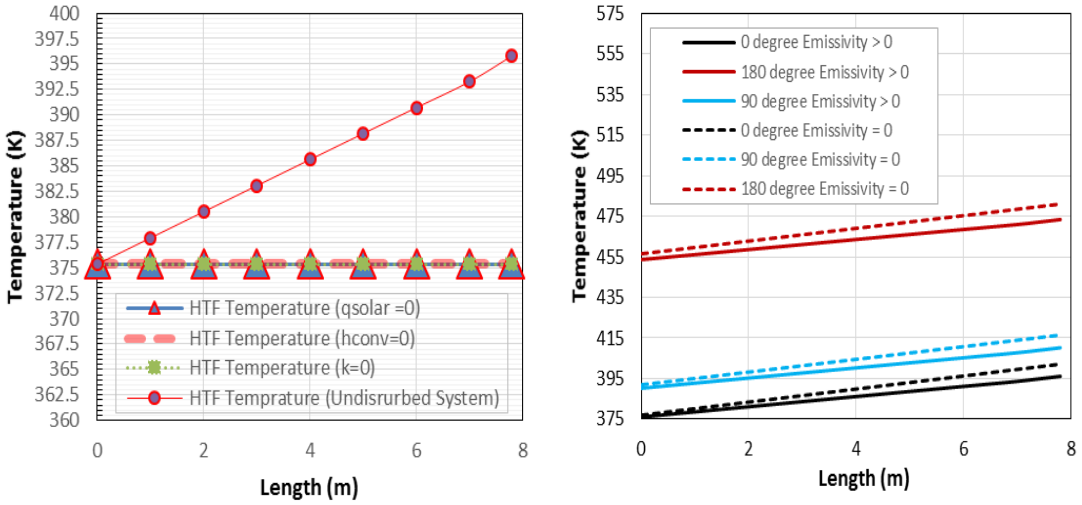

(a) (b)

Figure 5.3: HTF temperature results (a) Zero solar irradiation, zero absorber material conductivity, zero HTF convective heat transfer coefficient (b) Zero emissivity on AP

Secondly, a case of a receiver with a selective coating on the absorber surface was simulated. The model was used to reproduce results for the same PTSC operating conditions modelled by Hachicha et.al. [44] and experimented by Dudley et.al. [36].

Performance comparisons were made against these works. The design parameters used are shown in Table 5.2.

Table 5.2 Design Parameters of the SEGS LS2 used in our simulation and the simulation by [44]

Parameter	Value
Receiver length (L)	7.8 m
Collector aperture (W)	5 m
Focal distance (f)	1.84 m
Absorber internal diameter (D_a,inner)	0.066 m
Absorber external diameter (D_a,ext.)	0.070 m
Absorber emissivity (IR)	0.15
Glass internal diameter (D_g,inner)	0.109 m
Glass external diameter (D_g,ext.)	0.115 m
Glass emissivity (IR)	0.86
Receiver absorptance, visible (α)	0.96
Glass transmittance, visible (τ)	0.95
Parabola specular reflectance (ρ_p)	0.93
Incident angle	0.0
Solar irradiance	933.8 W/m^2
HTF	Syltherm 800
Mass flow rate (kg/sec)	0.68
Temperature HTF (inlet)	375.35 K
Temperature Ambient	294.35 K
Wind speed	2.6 m/s

Figure 5.4 (a) shows the temperature profile around the AP circumference obtained from a simulation done by [44]. From the AP inlet temperature profiles of the AP circumference were taken at five locations spaced every 2 meters along the AP. Figure 5.4 (b) shows simulation results done in this study for the same system.

In Figures 5.4, the maximum temperature difference along each circumference profile is not larger than approximately 80^{o}C. Equally true, there is a small difference between temperatures for the same points on the two graphs. The differences are utmost 0.3% (maximum discrepancy at 180^o). The angle 180^o is a location on the receiver that points directly away from the sun (and towards the center of the parabolic mirror). It can also be noted that in Figure 5.4, the temperature profiles around the circumference follow the profile of the concentrated solar irradiation flux whose profile is represented by the gray and black solid line shown in Figure 5.4 (a) and (b) respectively. The concentrated solar irradiation flux can be derived according to [64] as mentioned previously.

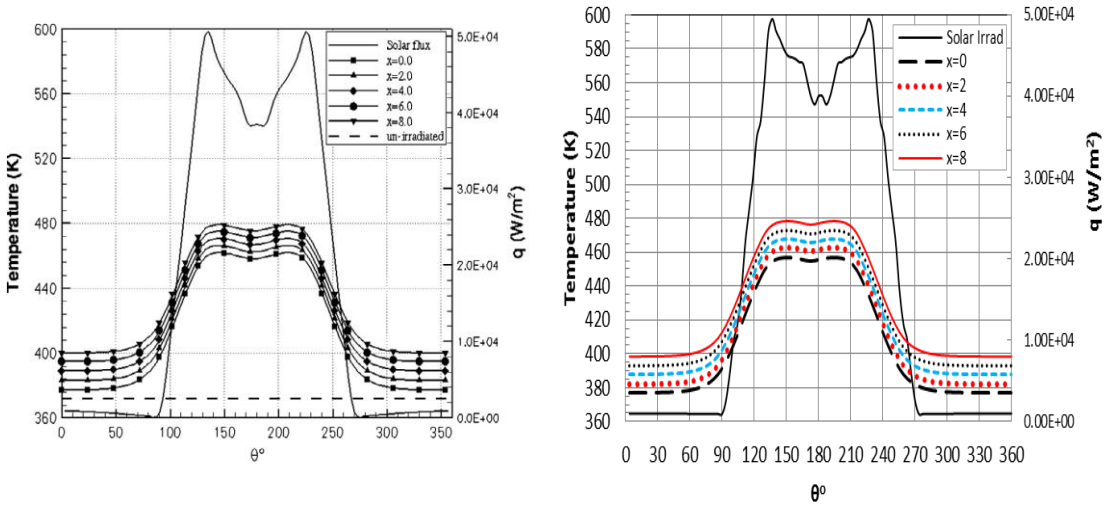

(a) (b)

Figure 5.4: Temperature Profiles around circumference (a) Simulation from [44] (b) Simulation from this study

Results for temperature variation along the axial direction for a 7.8 meter long receiver section showed a similar trend for this study simulated results and the works of 44. Temperatures were taken along the 0^o, 90^o and 180^o angular directions on the AP. The angle 0^o points directly towards the sun at normal position. Figure 5.5 (a) displays results from 44 and 73. Figure 24(b) shows results of the simulation of the same system done by this study. The maximum temperature variation along the axial direction over the receiver length (7.8m) is around 20^oC in both cases. HTF output temperatures are also shown in Figure 5.5 (a) and (b). The HTF temperature increment was compared and the difference is less than 0.5% for the 7.8 meters.

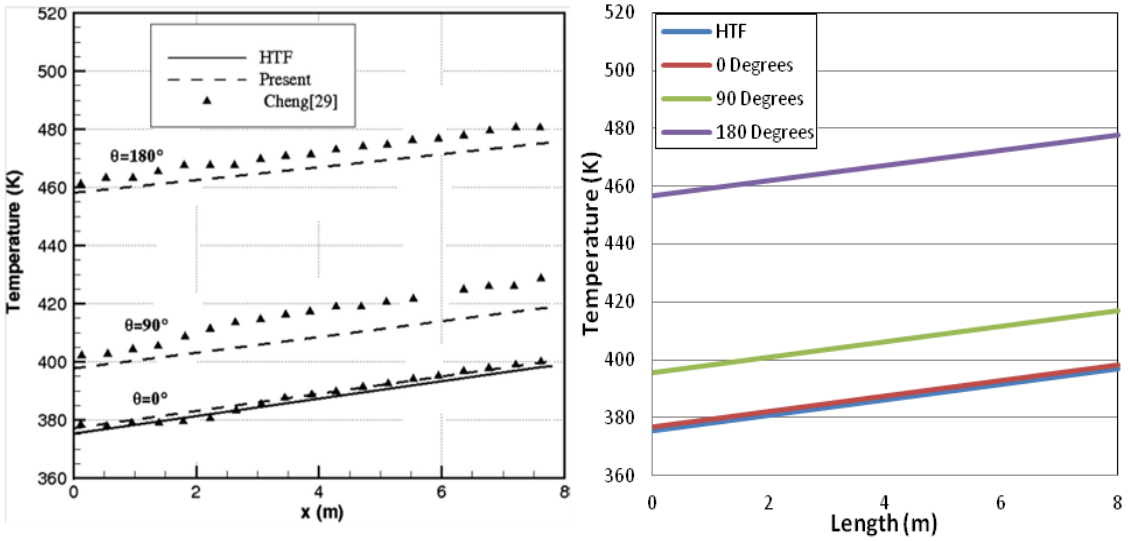

(a) (b)

Figure 5.5: Temperature variation for the AP and HTF along the length (a)According to reference 44 (b) Code from the present study

In Figure 5.6 (a), the GC temperature profile around the circumference is presented at a distance of 4m along the receiver length. The same conditions used in Figure 5.4 (a) are applied as well as un-irradiated. The temperature only varies by around 40^{o}C around the circumference, and is lower than the corresponding AP temperature. Results obtained from this study simulation for a similar system are shown in Figure 5.6 (b). The discrepancy is less than 0.7% (maximum discrepancy at 180^{o}).

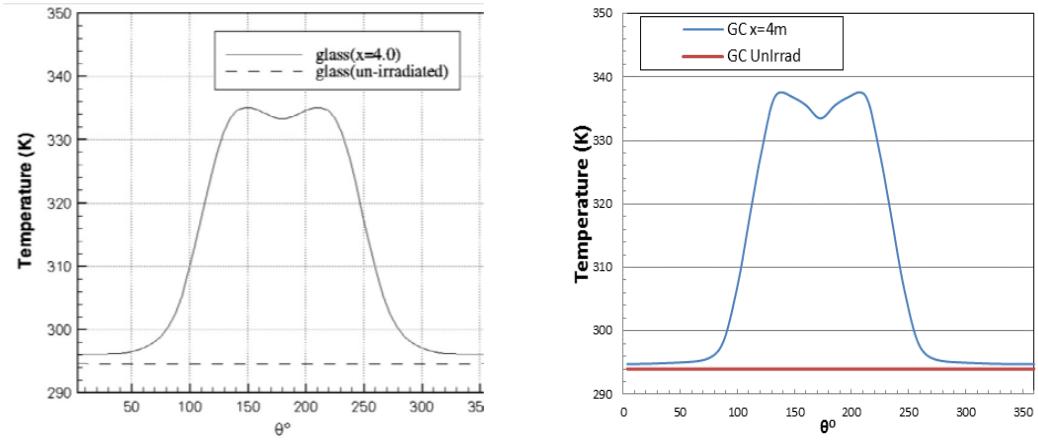

(a) (b)

Figure 5.6: Temperature variation for the GC (a) From reference 44 (b) Code from the present study

Chapter 6 Results

6.0. Introduction

In this chapter, results of the simulation introduced in chapter 5 are presented. First are the results for how HTF output temperature and receiver surface temperature profile changes with increasing HTF inlet temperature. Next are results for a comparison of the performance of different hot mirror coating materials in a PTSC receiver in terms of receiver surface temperature, HTF temperature, local and overall efficiencies. Thirdly, results are presented that describe the influence of visible transmissivity and IR reflectivity on the performance of a hot mirror coating. The fourth simulation compares a combination of a hot mirror and a selective coating with a selective coating only case. Lastly, the results for a comparison of a hot mirror with a selective coating are discussed.

6.1. Comparative performance of hot mirror coatings

6.1.1. Effect of HTF changing inlet temperature

In this section, the question of viability of a hot mirror coating to reduce heat losses at temperatures higher than 400^{o}C (selective coating thermal decomposition temperature) is addressed. A coating's viability is defined based on the temperature where heat losses become lower than a worst case heat loss scenario (an uncoated receiver herein called bare case). Three types of hot mirror coating are compared with a bare case in terms of HTF output temperature and surface profile temperatures. Indium Tin Oxide (ITO), Gold and Silver were used as hot mirror materials.

ITO is widely used as a hot mirror due to its high optical transmittance in the visible wavelength region and high reflectance in the infrared region [62]. A visible transmittance in excess of 90%, an IR reflectivity of about 90% and its remarkable properties such as good adherence to substrates, hardness and inertness have been reported [73]. Thin films of gold, upto 20nm thickness, display good reflectivity in the IR range [74]. Silver films find use as a single layer hot mirror coating [62].

The optical properties for the four scenarios namely Indium Tin Oxide (ITO) coated receiver, Gold coated receiver, Silver coated receiver used in the simulation are shown in Table 6.1. Similarly, the design parameters for the PTSC receiver simulated are shown in Table 6.2. Schematic layout for the setup is shown in Figure 6.1. The angles around the circumference are defined in Figure 6.1 (b).

Table 6.1 Simulated Scenarios, optical characteristics of the GC and AP for different hot mirror materials

		Bare		*ITO*		*Gold*		*Silver*	
		GC	*AP*	*GC*	*AP*	*GC*	*AP*	*GC*	*AP*
Visible	τ	0.935	0	0.875	0	0.44	0	0.4	0
	ρ	0.04	0.14	0.1	0.14	0.529	0.14	0.568	0.14
IR	τ	0	0	0	0	0	0	0	0
	ρ	0.14	0.14	0.85	0.14	0.78	0.14	0.95	0.14

τ – Solar transmissivity, ρ – IR Reflectivity

Table 6.2: Parabolic trough solar collector parameters used in the simulation

Parameter	*Value*
Collector aperture (W)	5 m
Focal distance (f)	1.84 m
Absorber internal diameter (D_a,inner)	0.066 m
Absorber external diameter (D_a,ext.)	0.070 m
Absorber emissivity (IR)	0.15
Glass internal diameter (D_g,inner)	0.109 m
Glass external diameter (D_g,ext.)	0.115 m
Parabola specular reflectance (ρ_p)	0.93
Incident angle	0.0
Solar irradiance	933.7 W/m^2
HTF	Molten Salt (600% $NaNO_3$, KNO_3)
HTF limiting temperature	873.15K
Mass flow rate (kg/sec)	5 kg/s
Heat capacity of HTF	$1443 + 0.172(T - 273.15) J/\text{kg}K$
Temperature HTF (inlet)	375.35 K
Temperature Ambient	294.35 K
Wind speed	1.5m/s to 2.6 m/s

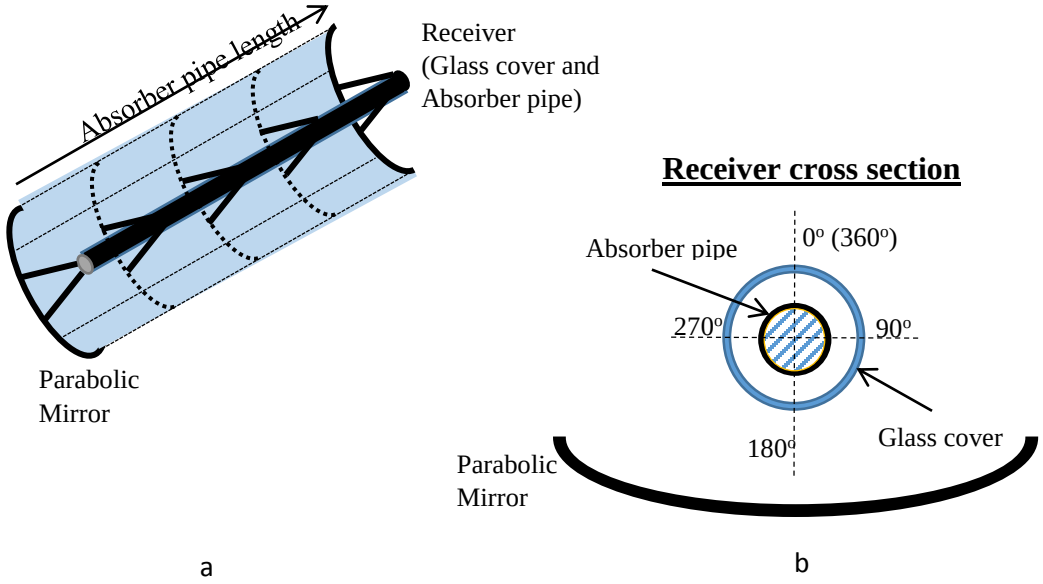

Figure 6.1: Schematic layout of a PTSC (a) axial direction (b) direction along Circumference

In Figure 6.2, the output HTF temperatures of a 7.8m long receiver unit at different HTF inlet temperatures (425K, 575K, 675K, and 775K) are shown. The four different scenarios are compared for four different start temperatures. The output HTF temperatures are presented as indicative to reduced heat losses. Figure 6.2 (a) shows the comparison at HTF inlet temperature of 425K. At this lower input HTF temperature, the HTF output temperature for the bare pipe case competes favorably with all the coating materials. This can be attributed to the relatively poor optical characteristics of the coating materials compared to the bare pipe. Compared to the bare case, all the coating materials have a lower transmissivity to the solar spectrum hence reducing solar irradiance onto the AP. However, Figure 6.2 (b) shows that as HTF inlet temperature increases this is offset. The foregoing negative effect is offset by the IR trapping characteristics.

On the other hand, heat losses increase from the bare pipe as temperature increases. Figure 6.2 (b) to (d) show the trend of improved performance of the coated cases as input HTF temperature increases. The trend is that, ITO gains first (~ 3K at 575K HTF input temperature) in performing better than the bare, then Silver and Gold gradually follow up respectively. Ultimately, at 775K, the ITO gains by 10K whilst the silver gains by ~ 2.5K. The Gold gains insignificantly.

The ITO having a good balance for visible transmission and IR reflectivity performs better than the bare pipe at the first inlet temperature increase. The Gold, having a lower value of IR reflectivity and low solar transmissivity, only performed similar to the bare pipe at 775K. Figure 6.2 demonstrates the effect of heat loss reduction at higher

temperatures by hot mirror coatings. At 775K, a coating material with spectral values such as with ITO or better would have HTF outlet temperature increased over 10K. Such a temperature increase makes the coating material viable to work at higher absorber pipe temperatures.

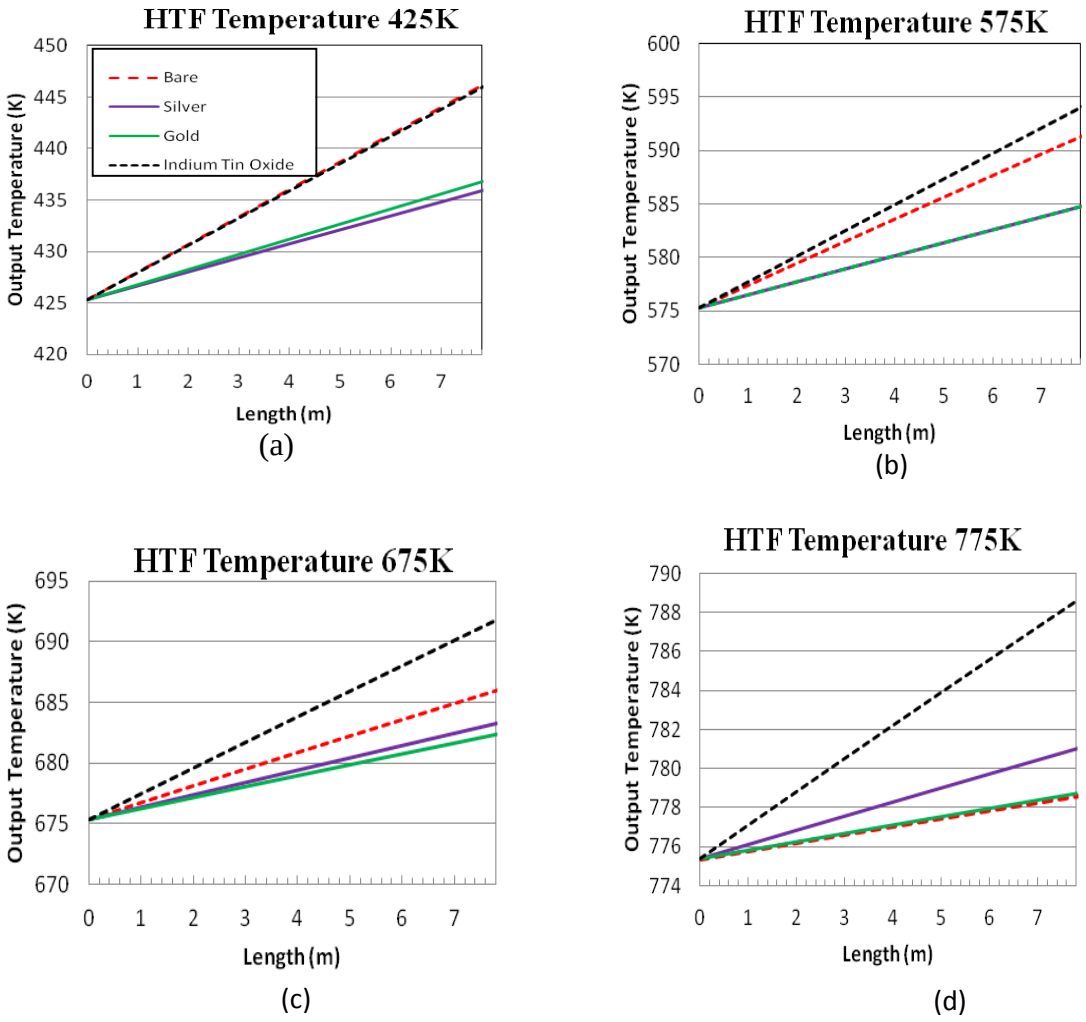

Figure 6.2: HTF outlet temperature for different inlet temperatures

To analyze the GC temperature profile, the ITO scenario was adopted. The ITO case is used owing to its better performance over the other cases as shown previously (Figure 6.3). The temperature profile around the circumference of the GC taken at different distances along the GC length (0m, 4m and 7.8m). Results of the surface temperature profiles are shown in Figure 6.3 (a to d).

Figure 6.3(a) shows that the highest GC temperature (450K) at HTF input temperature of 775K occurred at the exit section (x =7.8m), as expected. However, it is worth noting that the GC surface temperatures are significantly lower ($\Delta T = 120^o C \; to \; 350^o C$) than

the HTF temperatures at higher HTF temperatures (over 500K). GC surface temperatures in existing PTSC are only about 102^oC above the HTF operation temperatures ~ $350^oC\ to\ 400^oC$ [45]. The GC in hot mirror PTSCs can be cooler than that in existing PTSCs. This offers an opportunity to have a coating material placed on a surface that is at a much lower temperature than the HTF. As such, the PTSC can operate with higher HTF temperatures without the coating thermally decomposing. ITO can withstand temperatures of up to 700K [75]. As such, coating materials such as ITO, placed on the GC are exposed to lower temperatures below their thermal decomposition limits even at high HTF temperature.

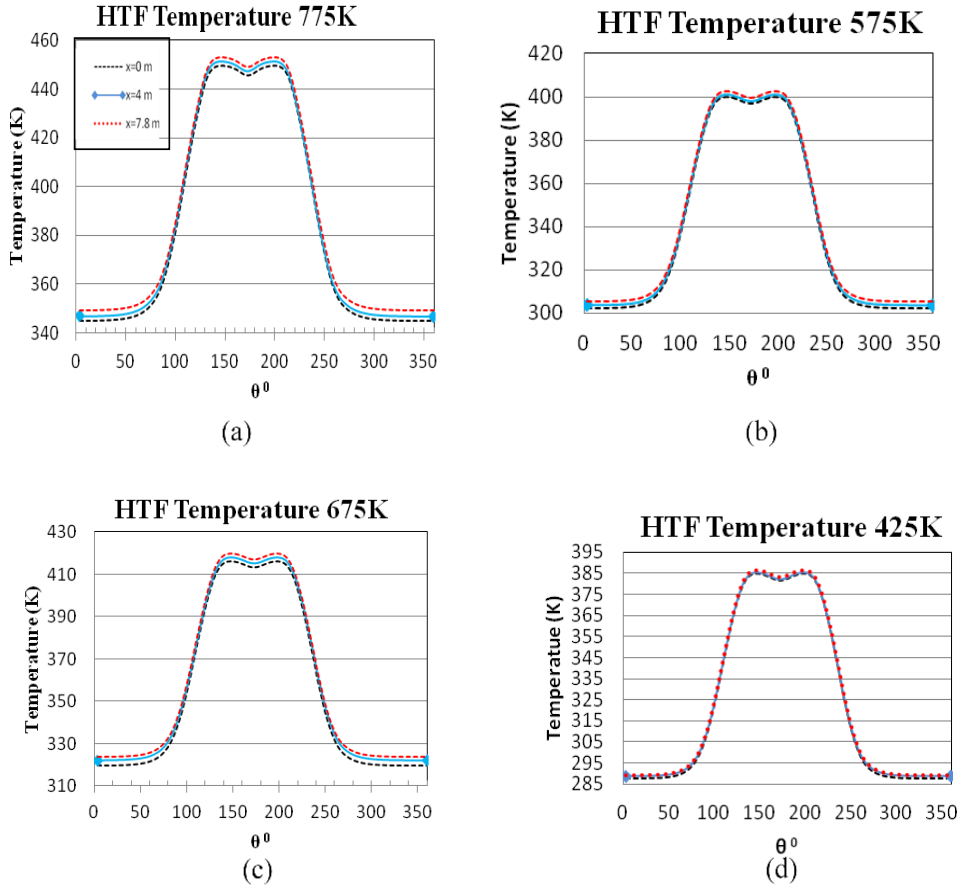

Figure 6.3: Temperature around the glass cover circumference taken at different distances for different input HTF temperatures

6.1.2 Effect of Hot Mirror coating on receiver performance

The question this section addresses is how different hot mirror coatings in PTSC receiver affect the receiver performance. The question is addressed by comparing how some selected hot mirror coating affects a variety of parameters such as surface

temperature distribution along the length and circumference of both the AP and GC, the HTF temperature distribution along the length, the local and overall efficiencies.

The GC temperature experiences the largest thermal gradient and absolute temperature in the bare pipe case (400 K to 450 K) (Figure 6.4 (a)), while the absolute temperatures for the coated GCs do not exceed 400 K, and their gradient is < 40 K (Figures 6.4 (d) and 6.5 (a) and (d)). The smaller thermal gradient induces fewer thermal stresses in the glass, allowing a longer lifetime. The lower GC temperature will allow coatings there without thermal decomposition even at high AP temperatures. Even for the highest AP temperature reached in the ITO case in excess of 1000 K, the GC temperature does not exceed 400 K. It is worthy to note that the molten salt limiting temperature is 827.15K. The comparison is mainly for the GC temperature and the coating limiting temperature.

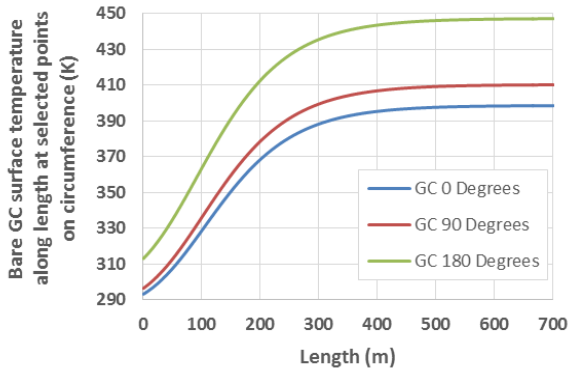

(a)

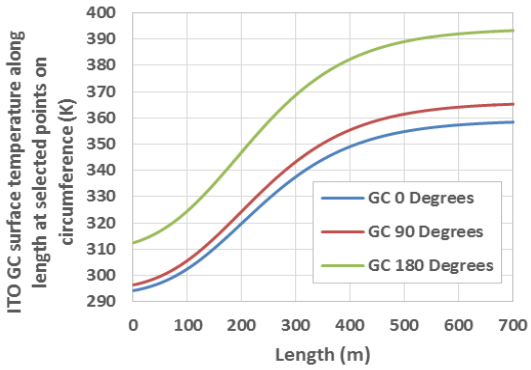

(d)

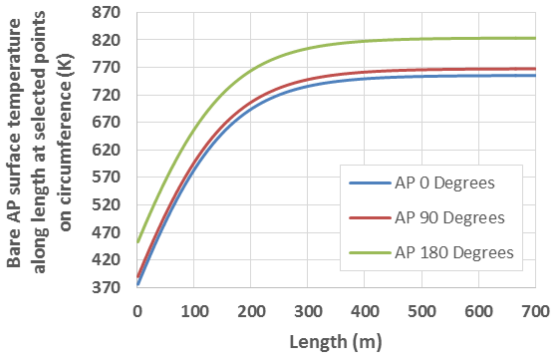

(b)

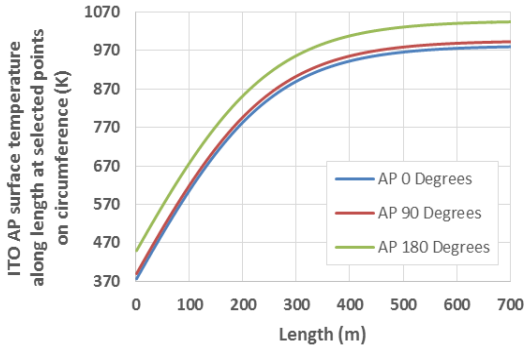

(e)

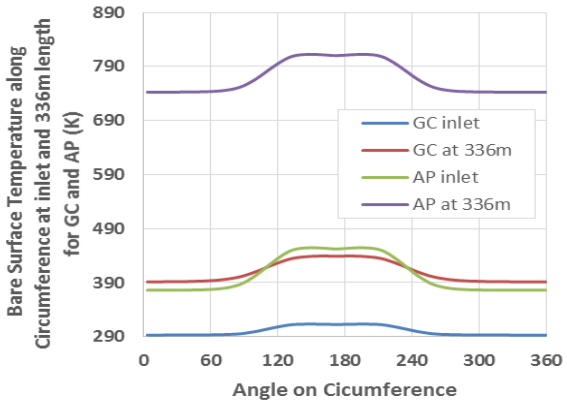

(c)

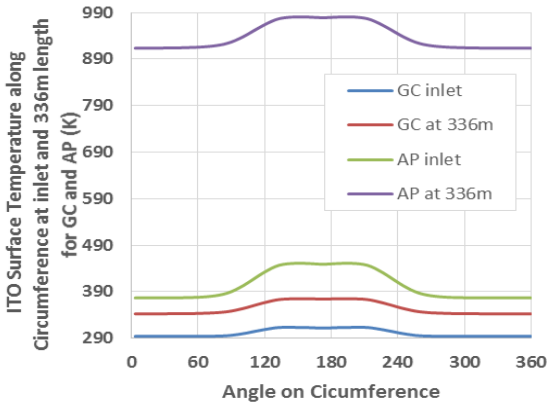

(f)

Figure 6.4: Glass cover surface temperature along length for bare pipe (a) and ITO (d); Absorber surface temperature along length for bare (b) and ITO (e); Surface temperature along circumference at 0 meters and 336 meters for bare (c) and ITO (f)

The AP surface temperature along the length taken at points 0º, 90º (=270º) and 180º angles on the circumference is shown in graphs (b) and (e). There is a similar temperature gradient of around 50 K present in all cases, which is close to the suggested maximum. The smaller effect of the different coating is likely due to the dominant heat dispersion effect arising from contact with the HTF.

Graphs (c) and (f) show the more detailed thermal distribution around the circumference of the AP and the GC, at the HTF inlet (0 m) and after a randomly chosen distance of 336 m along the length. The distributions clearly mimic the incoming radiation described by [64] as expected.

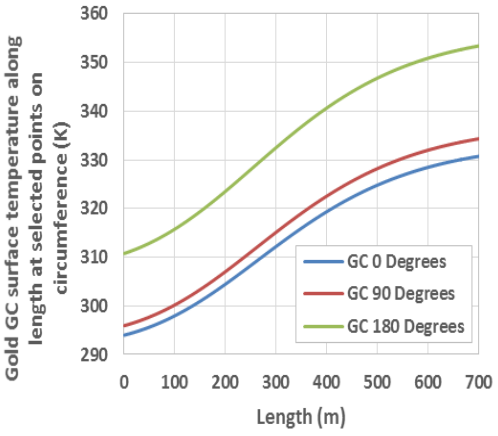

(a)

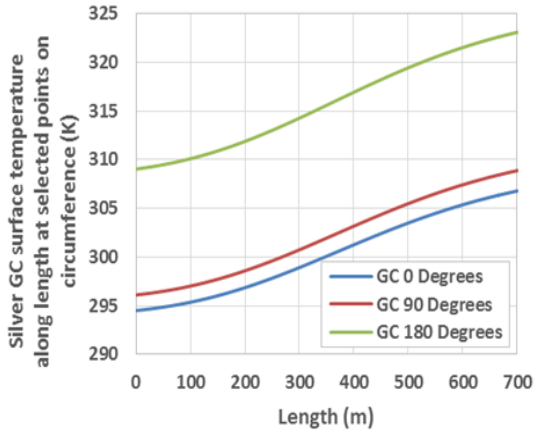

(d)

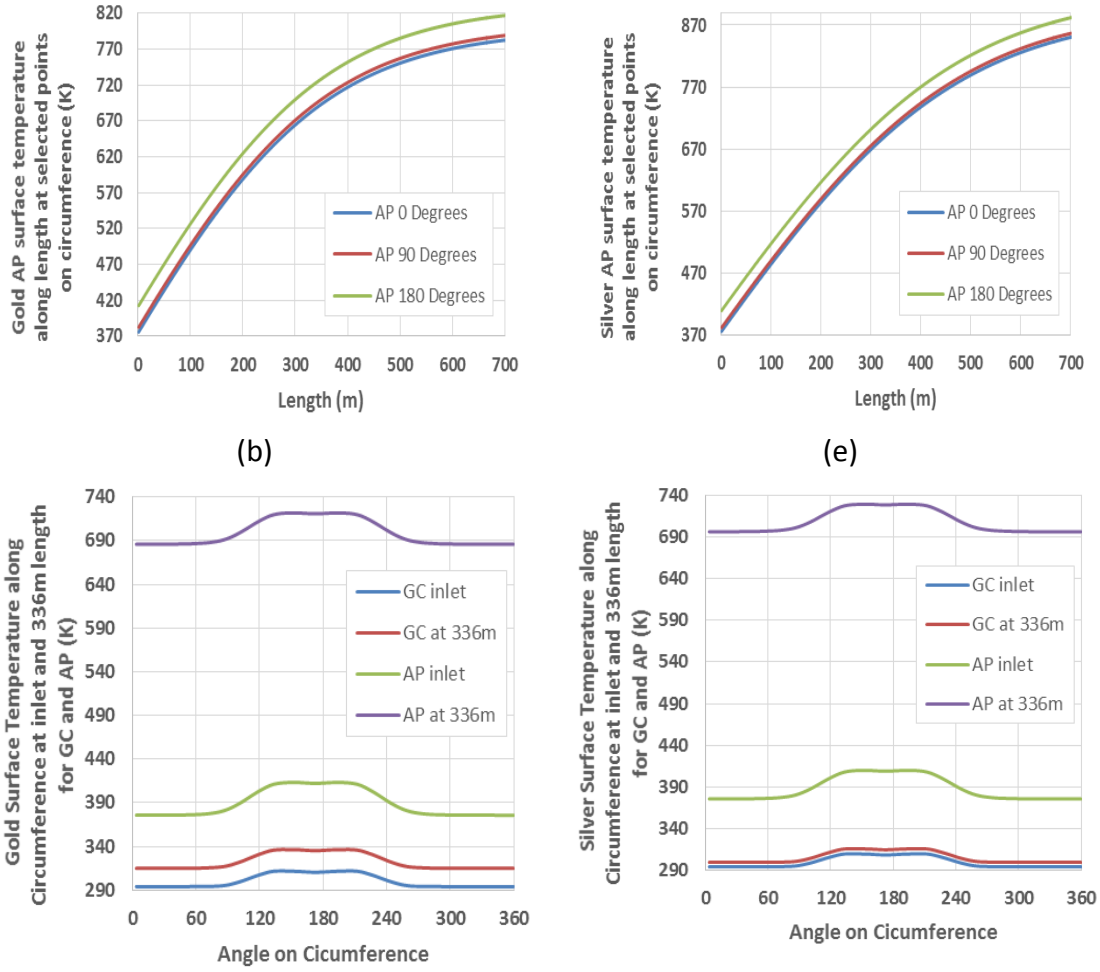

Figure 6.5: Glass cover surface temperature along length for gold pipe (a) and silver (d); Absorber surface temperature along length for gold (b) and silver (e); Surface temperature along circumference at 0 meters and 336 meters for gold (c) and silver (f)

Figure 6.6 compares the results for the HTF temperature variations along the length of the receiver for the different coatings. ITO outperforms all other considered coatings in terms of final HTF temperature. This is considered close to stagnation temperature (local efficiency has dropped to below 5% for all coatings, implying closeness to the local stagnation efficiency at 0%). ITO also approaches this stagnation temperature quite rapidly when compared to Gold and Silver. The reasonably better performance of the bare pipe over Gold and Silver is related to its good visible transmissivity, as will be seen in a later section.

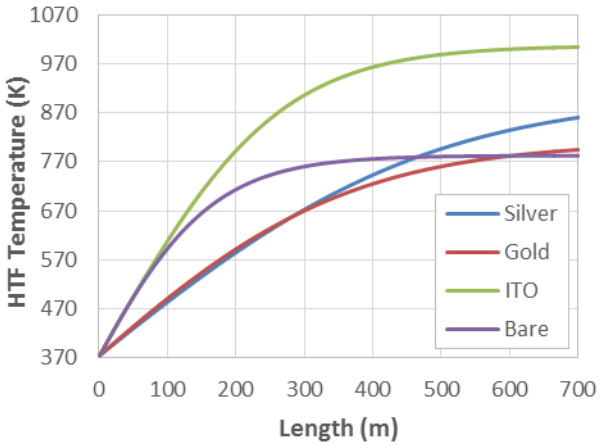

Figure 6.6: HTF temperature variations along the length

Figure 6.7 (a) below shows the local thermal efficiency along the AP length for the different coatings. The local efficiency curves for the different coatings show a strong local variation with respect to each other. The bare pipe starts with the highest efficiency since the typically deterring effect of coatings on visible radiation transmission is absent (see later), but soon drops to lowest place, as the IR retention effects of the coatings for the other receivers take effect. The ITO coating quickly overtakes the bare pipe and remains a good performer, until the Gold and Silver coating overtake it. This apparent loss of ITO in efficiency relative to the other coatings is due to the much higher temperature of the HTF in the ITO receiver rather than to superior performance of the Gold and Silver, which can be deduced from the overall efficiency graph in Figure 6.7 (b).

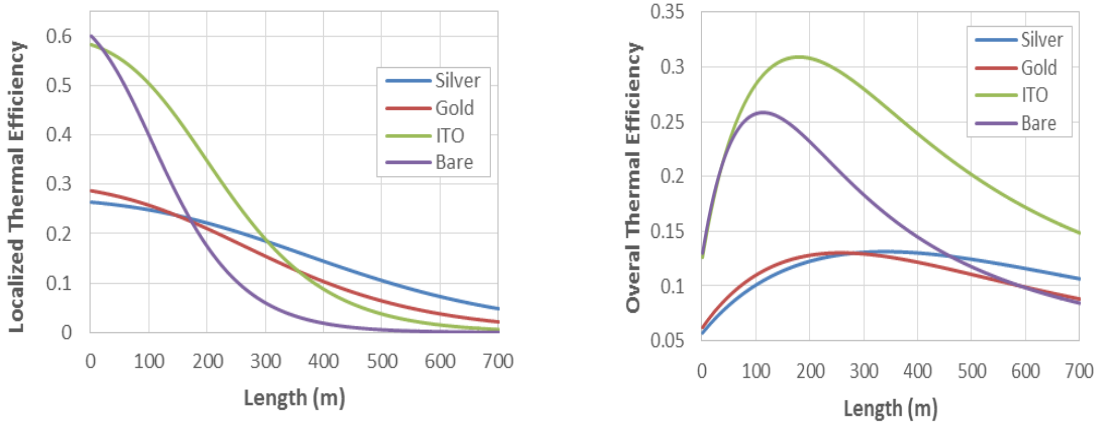

(a) (b)

Figure 6.7: (a) Local efficiency along the AP length for the different coatings (b) Overall optical and thermal efficiency along AP length for the different coatings

Figure 6.7 (b) is a measure of the overall performance of the solar plant in converting sunlight into electricity. The maxima of the curves indicate the overall optimal efficiency of the solar plants, as well as the optimum length at which this can be achieved. ITO reaches the highest plant efficiency of ~31%, with the bare pipe at 26%. The Gold and Silver coating peak around 12% efficiency, signaling weak performance. The likely causes for this ranking will be discussed in the next section.

6.1.3 Effects of visible transparency and IR reflectivity

Transparency to visible radiation allows more energy to fall onto the pipe, while reflectivity of the glass cover in the IR prevents more thermal radiation losses. In the case of ITO, Gold and Silver, materials with high reflectivity in the IR often have reduced transparency in the visible. In this section, the question of whether high visible transmissivity is a preferred characteristic to high IR reflectivity is addressed. This is done through the study of the performance of two hypothetical materials, H1 and H2. The material H1 has high IR reflectivity but relatively poorer visible light transparency, while these properties are reversed for H2. This section is intended as a general guideline for material design where a tradeoff has to be made between visible transparency and IR reflectivity. The GC spectral characteristics are shown in Table 6.3.

Table 6.3: Optical properties on the GC for H1 and H2

		H1	H2
Visible	Transmissivity	0.875	0.95
	Reflectivity	0.1	0.027
IR	Transmissivity	0	0
	Reflectivity	0.95	0.85

The GC temperature (shown figure 6.8 (a) and (c)) for H1 (strong IR mirror) has a smaller thermal gradient and absolute temperature than H2. A similar pattern is also observed in Figures 6.3 and 6.4 (a) and (c), where the HM coating prevents GC heating and promotes distribution of heat.

The AP temperature along the length taken at points 0^o, 90^o ($=270^o$) and 180^o angles on circumference is given by (b) and (e) in Figure 6.8. There is a similar temperature gradient of around 60K present in both cases. The thermal characteristic is influenced by the contact to the HTF rather than by optical properties, since these curves do not change much with variations in coating.

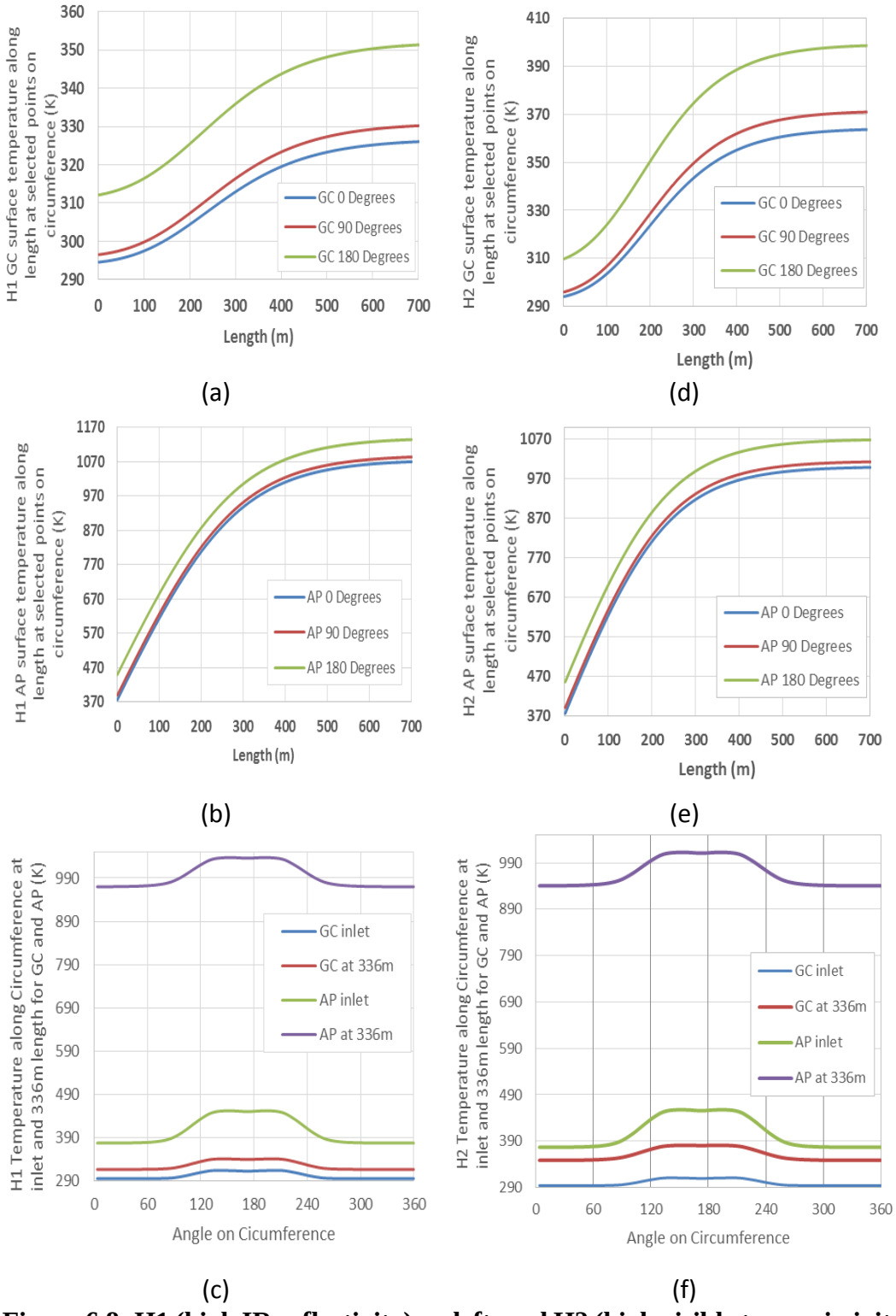

Figure 6.8: H1 (high IR reflectivity) on left, and H2 (high visible transmissivity) on right.(a) and (d) show GC temperature profile, (b) and (e) indicate AP

temperature profile and (c) and (f) a continuous temperature profile around the circumference at two selected locations, the inlet and at 336m

The temperature profile for H1 and H2 of the HTF along the length are shown in Figure 6.9 (a). Again the high visible transmissivity receiver H2 dominates initially and the heat loss reducing effect of H1 only set in at elevated temperatures, leading to a higher stagnation temperature.

The local efficiencies of H1 and H2 are shown in Figure 6.9 (b). H2 has a higher local efficiency initially due to its higher visible light transmissivity, which allows more radiation energy to impinge onto the AP. Again, the effects of the coating only set in at higher temperatures for H1.

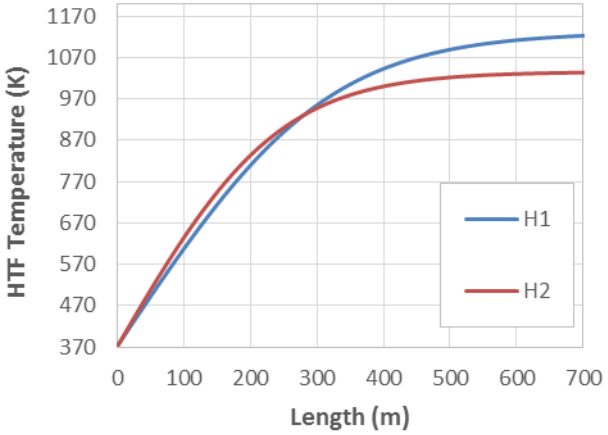

(a)

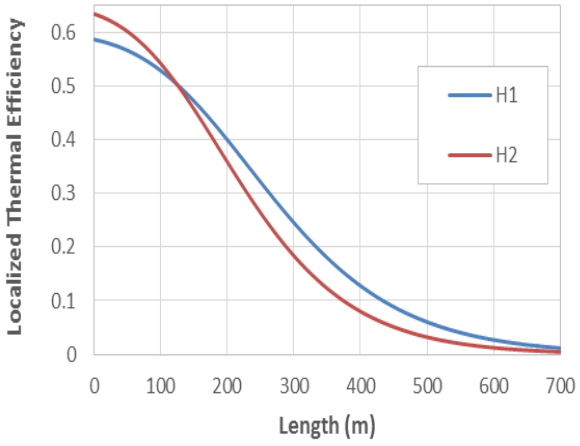

(b)

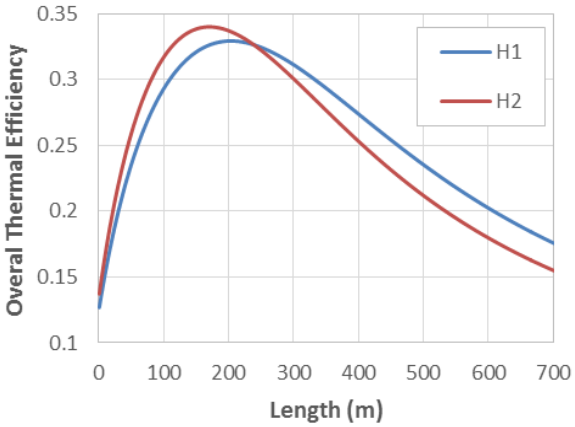

(c)

Figure 6.9: (a) HTF temperature along length for H1 and H2 (b) Localized efficiency along AP length for H1 and H2 (c) Maximum thermal efficiency for H1 and H2

The overall efficiency of the systems is shown in Figure 6.9 (c). Not only does H2 reach a higher overall efficiency (~34%), but it reaches it faster than H1. This implies a more efficient, smaller plant. In terms of these parameters, H2 would be a favorable design to use.

6.1.4 Selective coating and hot mirrors

In this section the question of how selective absorber coating (herein designated SC) on the AP and hot mirror coating on the GC perform comparatively is explored. It is also natural to ask if a combination of selective and hot mirror coating, used simultaneously, can aid performance. Three scenarios were considered, i.e., one of selective coating only (SC), one of a selective coating on the AP and hot mirror coating on the GC (SC+HM) and one of the previously discussed hot mirror coating scenarios. The simulation values are given in the Table 6.4.

Table 6.4: Spectral Specifications for the three scenarios, SC, SC+HM and HM, for the AP and GC

			SC	*SC+HM*	*HM*
GC	*visible*	*Transmissivity*	0.935	0.875	0.875
		Reflectivity	0.04	0.1	0.1
	IR	*Transmissivity*	0	0	0
		Reflectivity	0.14	0.85	0.85
AP	*visible*	*Transmissivity*	0	0	0
		Reflectivity	0.04	0.04	0.04
	IR	*Transmissivity*	0	0	0
		Reflectivity	0.85	0.85	0.14

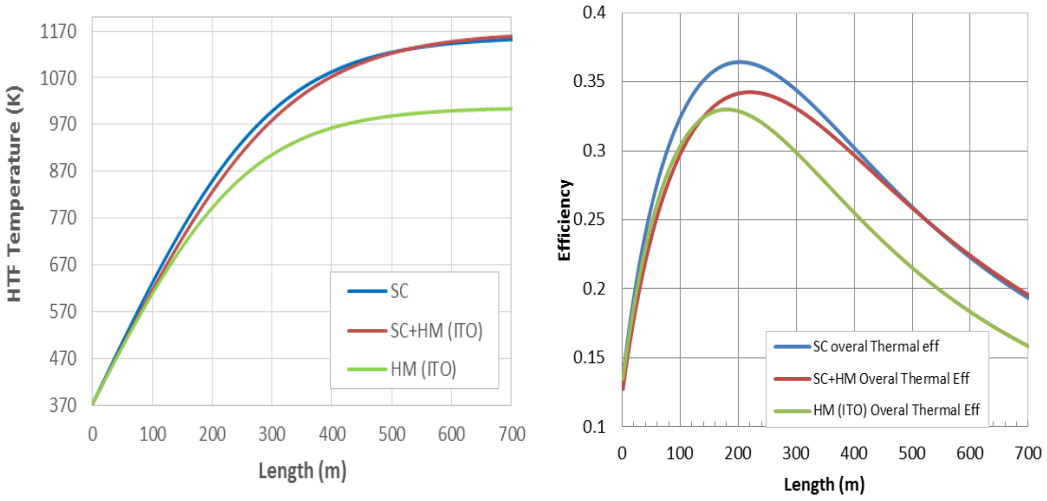

(a) (b)

Figure 6.10: (a) SC, SC+HM and HM cases overall efficiency (b) SC, SC+HM and HM cases HTF temperature

Figure 6.10 (a) shows the HTF temperature distribution for the scenarios. The HM coating reaches the lowest stagnation temperature, while there is very little difference in the temperature distributions of the SC and the SC+HM. The SC+HM scenario has the disadvantage of the relative low temperature ceiling on the AP imposed by SC coating thermal breakdown.

Figure 6.10 (b) summarizes the overall plant performance, indicating that the existing SC will outperform an ITO coating as well as a combination (SC+HM). In this case, the hot mirror advantage still lies with its much higher temperature ceiling, making it a choice for application where high temperature of the HFT is required without conversion to electricity.

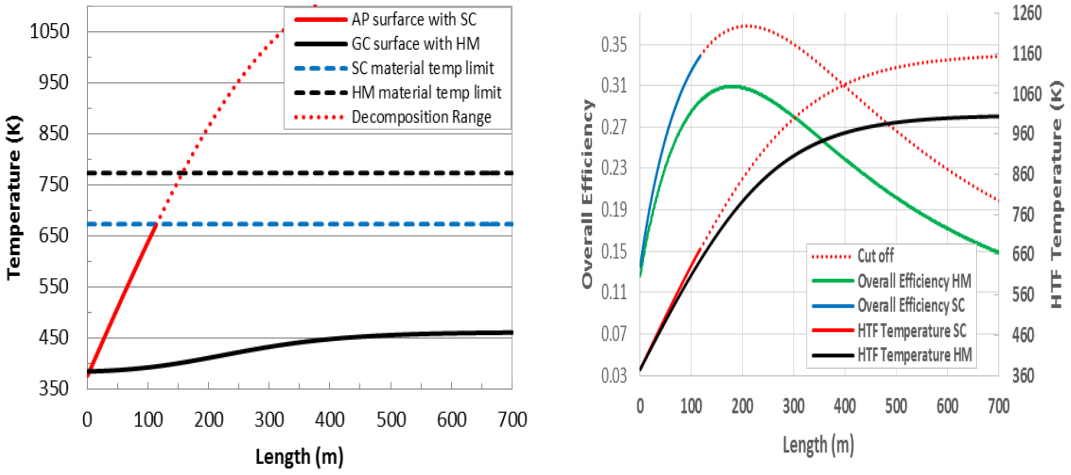

(a) (b)

Figure 6.11: Illustration of SC and HM temperature limitations (b) Total efficiency for the HM and SC case including cutoffs, indicating areas of validity, and HTF temperature

Figure 6.11 (a) displays the limitations of the selective absorber and the hot mirror coatings. The solid lines indicate regions where the coatings can function without thermal decomposition. For the SC located on the AP, the cut-off temperature of was chosen as ~670 K [22,25] which it reaches after approximately 100 m. The HM coatings can sustain a higher operational temperature, and the cutoff temperature was chosen as ~770 K [75]. The solid black line indicates the temperature behavior of the GC, where the HM coating is located, and it remains quite far from the cut-off temperature for the region under study. Since this region is close to the stagnation temperature, the GC temperature is never likely to reach the HM temperature limitation.

In Figure 6.11 (b), the maximum plant efficiency is shown, as well as the limitations of the SC and HM technologies. The temperature for the HTF in the case of the SC terminates at 670 K, but continues for the HM. The efficiency of the SC peaks at 37% but does not reach it due to temperature limitations. The HM coating reaches its peak of 31%. Nevertheless, in this case, even the terminated SC efficiency peak (at ~34%) surpasses the HM maximum, indicating that it is still a better choice in terms of efficiency.

Chapter 7 Discussions and Conclusions

7.0 Introduction

In this study a theoretical framework of a PTSC receiver coated with a hot mirror has been developed. The model was developed using a numerical analysis approach and code written in Visual Basic. It has provided a means to characterize a hot mirror coated PTSC receiver. This was demonstrated using various parameters such as local efficiency, overall efficiency, surface temperatures and the HTF temperatures.

Results of the model compared well with other simulation works with a discrepancy of less than 0.7%. Validation was done using data from experimentally validated simulations. In the sections below, conclusions drawn for the model theory, performance and results for the various simulations done are presented.

7.1 The Theory part

The theory of a hot mirror in a PTSC was analyzed numerically using the finite volume method (FVM). The control volume (CV) approach enabled the non-uniform incident solar radiation to be considered on each finite CV surface accurately during heat transfer analysis. Non-uniform solar flux contributes to a relatively stronger temperature gradient around the circumference than along the axial direction. As such, radiation exchange was very significant between and for surfaces on the circumference than along the length. The sizes of the CV were small enough $(\sim r = 0.002m)$ to justify the forgoing statement. Conduction and convection heat transfer modes in the hot mirror receivers were treated in similar ways as in existing PTSC receivers. However, radiation heat transfer was modified by the significant reflections of Infrared radiation occurring on the GC.

Hot mirror coatings on the GC inner surface reduced radiative heat losses by reflecting the emitted infrared radiation from AP back onto the AP. Equations 33 and 36 are formulations for radiative exchange developed for an enclosure between the AP and GC for all the CVs. The equations were derived from radiosity considerations of all CVs. A CV on the AP received emitted radiation from other CVs on AP via the hot mirror reflections by single and double reflections. These CVs were said to be in radiative contact. Similarly, the AP and GC exchanged radiation through reflections and also directly. The exchanges in reflected infrared radiation occurred even through more than two (double) reflections. However, the intensity of the reflected radiation diminished with increasing number of reflections. In the study, the single and double reflections received by any CV on the AP and GC have been described by equations 51 and 53 respectively. These represent the heat loss reduction effect of the hot mirror coatings in a PTSC receiver. Coupled in a Radiosity term from a CV surface, the equations can be used in the net radiation method. The net radiation method summed all the radiation quantities on any one CV. The result accounted for the radiation component in heat transfer analysis of a CV. It can be emphasized that equations 35

and 38 contain all the information about the significant hot mirror radiation interactions in a hot mirror PTSC receiver.

The theory developed in the study was simplified by assuming flat CV surfaces, gray, specular reflecting and diffuse emitting GC surfaces and gray, diffuse emitting and reflecting AP surfaces. The AP and GC surface spectral properties were also considered not temperature dependent. The CV sizes were small enough $(\sim r = 0.002m)$ for the flat approximation. Specular reflections on the GC were considered as most surfaces are smooth to wavelengths in the infrared spectrum. Most properties were considered constant with temperature. In reality, this is not the case. However, the discrepancies caused by this simplification were not significant as observed from the validation results.

7.2 The Simulation

The small discrepancy of less than 0.7% between results of experimentally validated simulation works and results from the code in this study showed a close match. The simulation validation was done by simulating systems that were modelled and had their results experimentally validated. It is thus hoped that by using the model, various hot mirror materials in PTSCs can be predicted. It is thus hoped that selection optimization of the hot mirror can be made easier.

7.3 Performance results

To appreciate the effect of a hot mirror coating in a PTSC receiver unit, various scenario of interest were simulated. Metallic and doped semiconductor hot mirror materials were considered for application as these are already in fabrication and use. The simulated scenarios were selected to show among other things the viability of hot mirror coating to reduce heat losses as temperature increased.

The ITO, Gold, Silver and the bare case performance were compared. The GC temperature seems to have been reduced and spread by the HM coating, which can have beneficial effects on reducing thermal stresses. The AP temperature distribution seems to have been affected little by the coating, probably due to its thermal contact with the HTF. The ITO outlet HTF temperature increased fast and reached the highest stagnation temperature, and the bare case scenario is only some length overtaken by Gold and Silver coatings. This suggests that there may be other parameters besides IR reflectivity affecting performance, and this is likely visible transmissivity. Of the coatings, ITO performs the best overall when plant performance is simulated.

The effects of IR reflectivity and visible transmissivity were isolated and studied in a hypothetical case, using two coatings H1 (good IR reflector, poorer visible transmitter) and H2 (poorer IR reflector, good visible transmitter). While the coatings showed similar behavior to the previous case in terms of temperature distribution, it is concluded that visible transmissivity was the more important characteristic in terms of

efficiency, while IR reflectivity was more important in terms of a higher temperature ceiling of the HTF.

The ITO coating performance was compared against a conventional SC, and a SC+HM combination. The optical characteristics of the SC were still superior, and the SC performed better in terms of efficiency. A combination of HM and SC in the same receiver did not yield any obvious advantages. The HM by itself did not outperform the SC efficiency-wise, but still was shown to have the advantage of being able to achieve much higher HTF temperatures. Even including the cut-off temperature limitations, the SC managed to reach a higher efficiency than the peak efficiency of the HM considered.

The comparisons of ITO, SC and SC+HM suggest that the SC is a better candidate for high efficiency solar plants, while HM coatings can be used for high HTF temperature applications.

7.4 Recommendations

In view of the observations made in the study, (visible transmissivity affects receiver performance more than infrared reflectivity), it is recommended that future work be done to investigate high visible transmissivity in hot mirror materials whilst maintaining IR reflectivity. Increased transmissivity increases solar energy input. Thus the effect of IR reflectivity with respect to stagnation point are necessary to investigate.

Increased temperatures also call for a thorough into the structural thermal stresses. In any case, since experimental research is still under way, it is recommended that the study includes analysis of thermal stresses in the hot mirror PTSC receiver.

8.0 References

1. Solomon, S., Qin, D., Manning, M., Chen, Z., Marquis, M., Averyt, K.B., Tignor, M. and Miller, H.L. Climate change 2007; The physical science basis, New York, Cambridge University Press, 2007.
2. Kalogirou, S. Solar thermal collectors and applications, Progress in Energy and Combustion Science 30, 2004, pp. 231–295.
3. UNFCCC 2009, Copenhagen Accord, Document FCCC/CP/2009/11/Add.1, available at http://unfccc.int/documentation/items/2643.php, Accessed on 26th December, 2016
4. IEA, 2012: Measuring progress towards energy for all. World Energy Outlook 2012, Paris, OECD/IEA, pp. 529-668
5. IEA, 2010: World energy outlook 2010: Executive summary, available at htpp://www.worldenergyoutlook.com/docs/weo2010/WEO2010ES_English.pdf. Accessed 10th August, 2016
6. Duffie, J. and Beckman W. Solar engineering of thermal processes, 4th Edition, Hobokeo, New Jersey, John Wiley & Sons, Inc, 2013
7. Kreith, F. and Goswami, D. A handbook of energy efficiency and renewable energy, New York, CRS Press, 2007, pp. 1052
8. Kalogirou, S. Solar Energy Engineering Processes and Systems, Second Edition, The Boulevard, Langford Lane, Kidlington, Oxford OX5 1GB, UK, Academic Press, 2014
9. Richter, C. Concentrated solar power global outlook 09 – why renewable energy is hot, Green peace international solarPACES and ESTELA, 2009, pp. 18.
10. Shaner, W.W and Duff, W.S. Solar thermal electric power systems: comparison of line-focus collectors. Sol Energy 1979, 22, pp. 13–49.
11. DLR 2007: WP1Review of CSP and desalination technology, available at http://www.dlr.de/tt/portaldata/41/resources, Accessed on 7th June, 2016
12. Kearney, D.W. and Price, H.W. Solar thermal plants-LUZ concept (current status of the SEGS plants). Proceedings of the Second Renewable Energy Congress, Reading UK, vol. 2, 1992, pp. 582–8.

13. Grasse, W. Solar PACES Annual Report, DLR Germany; 1995.
14. Porta, F.L. Technical and economical analysis of future perspective of solar thermal power plants, Report of IER, 2005.
15. Kutscher, C.F., Davenport, R.L., Dougherty, D.A., Gee, R.C., Masterson, P.M. and May, E.K. Design approaches for solar industrial process heat systems. Tech. Rep. No. SERI/TR-253-1358. Colorado, SERI, 1982.
16. Cameron, C.P. and Dudley V.E. Acurex Solar Corporation Modular Industrial Solar Retrofit Qualification Test Results, Tech. Rep. No. SAND85-2316. Albuquerque, SANDIA, 1987
17. Weiss, W. and Rommel, M. Process heat collectors, State of the art within task 33/ IV. IEA SHC-Task 33 and SolarPACES-Task IV. Gleisdorf: AEE INTEC; 2008.
18. Riffelmann K.,Ritchert T., Nava P. and Schweizter A. Ultimate Trough – A significant step towards cost-competitive. SolarPACEs 201, Energy Procedia 49 (2014) 1831 – 1839
19. Micheal F. Modest, Radiative Heat Transfer, Second Edition, California, Academic Press, 2003.
20. Rajput, R. K. Heat and mass transfer, Revised Edition, New Delhi, S. Chand and company, 2008, pp. 678.
21. Kreith, F., Manglik, R. M. and Bohn, S. M. Principles of heat transfer, 7th Edition, Global engineering, 2011, pp. 21
22. Padilla, R., Demirkaya, G., Goswami, Y., Stefanakos, E. and Rahman, M. Heat transfer analysis of parabolic trough solar receiver, Appl Energy 2011;88–110.
23. Alguacil, M., Prieto, C., Rodriguez A. and Lohr J. Direct Steam generation in parabolic trough collectors, Elsevier, Energy Procedia 2014; 49, pp. 21-29,
24. He, Y., Xiao, J., Cheng Z. and Tao, Y. A MCRT and FVM coupled simulation method for energy conversion process in parabolic trough solar collector, Renew Energy, V36, 2011, pp.:976-85
25. Kennedy, C.E. et.al. Progress in development of high-temperature solar-selective coating, NREL/CP-520 36997, 2005, pp. 1-7.

26. Sievers, A.J. Fundamental limits to spectral selectivity of composite materials, Solar Science Materials, Academic Press Inc., 1980
27. Frank, P. Incropera and David, P. DeWitt. Fundamentals of heat and mass transfer, 5th Edition, Wiley, New York, 2012, pp. 783-784
28. Çengel, Y.A. and Ghajar, A.J. Heat and mass transfer: fundamentals & applications, 4th Edition, McGraw-Hill, New York 2011.
29. Tiwari, G. N. and Arvind, S. Tiwari. Handbook of Solar Energy: Theory, Analysis and Applications, CRC Press, Narosa Pub. House Boca Raton FL New Delhi, 2002.
30. Lüpfert, E. et.al. Experimental analysis of overall thermal properties of parabolic trough receivers, Solar Energy Engineering, 2008, pp. 1-30.
31. Burkholder, F. and Kutscher, C. Heat loss testing of Schott's 2008 PTR70 parabolic trough receiver, NREL/TP - 550-45633, 2009, pp. 1-58.
32. Jimenez, Pech A. Efficiency curves analysis of a parabolic trough solar collector in the Yucatan Peninsula, Journal of Renewable and Sustainable Energy 4, 021203, 2012; doi: 10.1063/1.3676071
33. Kalogirou, S. Solar thermal collectors and applications, Progress in energy and combustion science, 2004.
34. Price, H. et.al. Advances in parabolic trough solar power technology," Solar Energy Engineering; 124:109-25, 2002.
35. Lampert, C.M. Optical Coatings for Energy Efficiency and Solar Applications, Proc. Soc. Photo-Opt. Instrum. Eng., 324, 1982.
36. Dudley, V. E., Kolb, G. J. and Mahoney, A. R. Test Results: SEGS LS-2 Solar Collector, Report No. SAND94-1884, SNL, Albuquerque, NM, 1994.
37. Bader, R., M. Barbato, A. Pedretti, and A., Steinfeld. An air-based cavity-receiver for solar trough concentrators. Journal of Solar Energy Engineering 132(3):031017. 2010.
38. García-Valladares O. and N. Velázquez. Numerical simulation of parabolic trough solar collector: improvement using counter flow concentric circular heat exchangers. International Journal of Heat and Mass Transfer, 52(3):597–609, 2009.

39. Gang P., Honglun Y., Qiliang W., Xiaona H. and Jing L. Performance study and comparative analysis of traditional and double-selective-coated parabolic trough receivers. Energy 145 (2018) 206e216
40. De Risi A, Milanese M, Laforgia D. Modelling and optimization of transparent parabolic trough collector based on gas-phase nano-fluids. Renew Energy 2013;58: 134–9.
41. Forristall, R. EES Heat Transfer Model for Solar Receiver Performance, Proceedings of ISEC, Solar 2004, Portland, Oregon, July 11-14, 2004.
42. Cheng ZD, He YL, Xiao J, Tao YB, Xu RJ. Three-dimensional numerical study of heat transfer characteristics in the receiver tube of parabolic trough solar collector. Heat Mass Transfer 2010; 37: 782–7.
43. Men, W., Matthew, R. and Aldo, S. Three-Dimensional Optical and Thermal Numerical Model of Solar Tubular Receivers in Parabolic Trough Concentrators, Journal of Solar Energy Engineering, Vol. 134, page 1, 2012.
44. Hachicha AA, Rodríguez I, Capdevila R, Oliva A. Heat transfer analysis and numerical simulation of a parabolic trough solar collector. Appl Energy 2013; 111:581–92.
45. Edenburn Michael W. Performance analysis of a cylindrical parabolic focusing collector and comparison with experimental results. Sol. Energy1976;18:437– 44.
46. Ratzel, A. C. et.al. Energy loss by thermal conduction and natural convention in annular solar receivers, Plenum Press, New York, 1978.
47. S. Odeh, G. Morrison, and M. Behnia. Modelling of parabolic trough direct steam generation solar collectors. Solar energy, 62(6):395–406, 1998.
48. Abengoa Solar. Solar Power for a sustainable world. http://www.abengoasolar.com/web/en/plantas_solares/plantas_propias/espana accessed on 15th January, 1917
49. Kalogirou S., Parabolic Trough Collector System for Low Temperature Steam Generation: Design and Performance Characteristics. Applied Energy. Vol. 55, No. I. pp. 1 19. lY96

50. Lampert, C.M. Heat mirror coatings for energy conserving windows. Solar energy materials, 6, 1981.
51. Lampert, C.M. Materials chemistry and optical properties of transparent conductive thin films for solar energy utilization. Ind. Eng. Chem. Prod. Res. Dev. 1982, 21, 612-616
52. Lampert, C.M. Advanced optical Material for energy efficiency and solar conversion. Britain, Solar and Wind Technology, Vol 4, 1987, pp. 347-379
53. Winegarner R.M. Proceeedings of the International Solar Energy Society. (USA and Canada). American Section International Solar Society, University of Delaware, Newark, DE, 1976, vol 6, p339.
54. Jarvinen P.O. Journal of Energy, 1978, 2, 95
55. Levin P.E.and Schumecher. Discussion of Heat Mirror Film, Performance, Production Processes and Cost Estimates. Research and Development, Sierracin Corporation, 1977
56. Selkowitz S.E. ASHRAE Trans. 1979, 85 (2), 669.
57. Granqvist, C. G. Spectrally Selective Coatings for Energy Efficiency and Solar Applications, Physica Scripta. Vol. 32, 1985, pp. 401-407,
58. Karlsson, B., Ribbing, C.G. Technical Report of the Inst. of Technol., Contract 3879-1, Uppsala, Sweden, 1978
59. Rubin, M., Creswick, R. and Selkowitz, S. Transparent Heat Mirror for Windows: Thermal Performance, 11 Proceedings of the 5th National Passive Solar Conference, Amherst, Mass., October 1980.
60. Valkonen, E. et.al. Solar Optical Properties of thin films of Cu, Ag, Au, Cr, Fe, Co, Ni, and Al. Solar Energy, Vol 32 No. 2, 1984,pp. 311-222
61. Hamberg, I. and Granqvist, C.G. Optical properties of transparent and heat reflecting indium tin oxide films: Experiment data and theoretical analysis, Solar energy materials 11, 1984 pp. 239-248
62. Lampert, C.M. Transparent heat mirror and deposition technology, SPIE, Los Angeles, January 25-29, 1982

63. Grena, R. Efficiency gain of a solar trough collector due to an IR reflective film on the non-irradiated part of the receiver, Int. J. Green Energy 8(7), 715, 2011.
64. Jeter, M. Calculation of the concentrated flux density distribution in a parabolic trough collectors by a semifinite formulation, Sol. Energy 37(5), 1986, pp. 335–345
65. William, S.J. Engineering Heat Transfer, PSW Publishers, 1986, pp. 15.
66. Lienhard, J.IV. and Lienhard, J.V. A Heat Transfer Text Book, Available on http://web.mit.edu/lienhard, Accessed on 12th May, 2013.
67. Gnielinski, V. New equations for heat and mass transfer in turbulent pipe and channel flow, Int Chem Eng., 16(2), 1976, pp. 359–363.
68. Nellis, G. and Klein, S. Heat transfer, 1st Edition, New York, Cambridge University Press, 2009.
69. Mullick, S.C. et. al. An improved technique for computing heat loss factor. Sol Energy 42 (1), 1, 1987.
70. Siegel, R., Howell, J.R. and Menguc, M.P. Thermal radiation heat transfer, 5th Edition, New York, CRC Press, 2010.
71. Patankar, S.V. Numerical Heat Transfer and Fluid Flow, Hemisphere Publishing Corporation, Washington, USA, 1980.
72. Allegrezza, M. et.al. Transparent conducting oxides for high temperature processing, Energy Procedia 44,23– 31, 2014.
73. Granqvist, C. G. Radiative heating and cooling with spectrally selective surfaces, Applied Optics, 20 (15), DOI: 10.1364/AO.20.002606, 1981, pp. 2606-2615
74. Loebich, O. The optical properties of gold, Gold Bull. 5(1), 1972, pp.2.
75. Gregory, O. J. High temperature stability of indium tin oxide thin films, Solid thin films, Elservier, 406, 2002, pp. 293.

9.0 Appendix A

Simulation Code

```
Sub Activatingworkingsheet() 'Activates working sheet

   Worksheets("Sheet4").Activate

   MsgBox ("Enter All Parameters")

End Sub


Sub SolarIRRandGuessedTemperature() ‘Maps Solar flux on CVs and initiates guessed temperature
for AP and GC CVs

         Tf = Cells(6, 6).Value

 For i = 1 To 100       'Guessed Temperature values for AP and GC CVs’ temperatures (100 is the No.
of CV                              along circumference)

      Cells(27, i * 3).Value = Tf + 1         'AP CV

      Cells(27, i * 3 + 300).Value = Tf - 1   'GC CV

      Cells(25, i * 3).Value = Worksheets("sheet5").Cells(i + 2, 13).Value

Next i

End Sub


Sub Fillupcells() ' Populates worksheet4 cells with coefficient equations

   Worksheets("Sheet4").Range("A31:DR197").Clear

   For i = 1 To 1000

   Range(Cells(29 + i, 1), Cells(29 + i, 1309)).Select

   Selection.AutoFill Destination:=Range(Cells(29 + i, 1), Cells(i + 30, 1309)), Type:=xlFillDefault

   Next i

End Sub


Sub CVTemperature() ‘Extracts Temperature values after error is minimized for CVs

Dim e1 As Double, e2 As Double, e3 As Double, e4 As Double, e5 As Double, e6 As Double, e7 As
Double, e8 As Double, e9 As Double, e10 As Double, e11 As Double, e12 As Double, e13 As Double,
e14 As Double, e15 As Double, e16 As Double, e17 As Double, e18 As Double, e19 As Double, e20
As Double, e21 As Double, e22 As Double, e23 As Double, e24 As Double, e25 As Double, e26 As
Double, e27 As Double, e28 As Double, e29 As Double, e30 As Double, e31 As Double, e32 As
Double, e33 As Double, e34 As Double, e35 As Double, e36 As Double, e37 As Double, e38 As
```

```
Double, e39 As Double, e40 As Double, e41 As Double, e42 As Double, e43 As Double, e44 As
Double, e45 As Double, e46 As Double, e47 As Double, e48 As Double, e49 As Double, e50 As
Double, e51 As Double, e52 As Double, e53 As Double, e54 As Double, e55 As Double, e56 As
Double, e57 As Double, e58 As Double, e59 As Double, e60 As Double,Dim e61 As Double, e62 As
Double, e63 As Double, e64 As Double, e65 As Double, e66 As Double, e67 As Double, e68 As
Double, e69 As Double, e70 As Double, e71 As Double, e72 As Double, e73 As Double, e74 As
Double, e75 As Double, e76 As Double, e77 As Double, e78 As Double, e79 As Double, e80 As
Double, e81 As Double, e82 As Double, e83 As Double, e84 As Double, e85 As Double, e86 As
Double, e87 As Double, e88 As Double, e89 As Double, e90 As Double, e91 As Double, e92 As
Double, e93 As Double, e94 As Double, e95 As Double, e96 As Double, e97 As Double, e98 As
Double, e99 As Double, e100 As Double, ArrayTs1(1 To 100) As Double,Dim eg1 As Double, eg2 As
Double, eg3 As Double, eg4 As Double, eg5 As Double, eg6 As Double, eg7 As Double, eg8 As
Double, eg9 As Double, eg10 As Double, eg11 As Double, eg12 As Double, eg13 As Double, eg14 As
Double, eg15 As Double, eg16 As Double, eg17 As Double, eg18 As Double, eg19 As Double, eg20
As Double, eg21 As Double, eg22 As Double, eg23 As Double, eg24 As Double, eg25 As Double,
eg26 As Double, eg27 As Double, eg28 As Double, eg29 As Double, eg30 As Double, eg31 As
Double, eg32 As Double, eg33 As Double, eg34 As Double, eg35 As Double, eg36 As Double, eg37
As Double, eg38 As Double, eg39 As Double, eg40 As Double, eg41 As Double, eg42 As Double,
eg43 As Double, eg44 As Double, eg45 As Double, eg46 As Double, eg47 As Double, eg48 As
Double, eg49 As Double, eg50 As Double, eg51 As Double, eg52 As Double, eg53 As Double, eg54
As Double, eg55 As Double, eg56 As Double, eg57 As Double, eg58 As Double, eg59 As Double,
eg60 As Double, Dim eg61 As Double, eg62 As Double, eg63 As Double, eg64 As Double, eg65 As
Double, eg66 As Double, eg67 As Double, eg68 As Double, eg69 As Double, eg70 As Double, eg71
As Double, eg72 As Double, eg73 As Double, eg74 As Double, eg75 As Double, eg76 As Double,
eg77 As Double, eg78 As Double, eg79 As Double, eg80 As Double, eg81 As Double, eg82 As
Double, eg83 As Double, eg84 As Double, eg85 As Double, eg86 As Double, eg87 As Double, eg88
As Double, eg89 As Double, eg90 As Double, eg91 As Double, eg92 As Double, eg93 As Double,
eg94 As Double, eg95 As Double, eg96 As Double, eg97 As Double, eg98 As Double, eg99 As
Double, eg100 As Double

Worksheets("Sheet4").Activate

Application.Calculation = xlCalculationManual

        For j = 1 To 100            '(100 is the No. of CV along circumference)

        Cells(29, j * 3).Value = Cells(6, 6).Value + 1

Next j


For i = 1 To 1000    'Extracting CV Temperatures from spreadsheet4

        Range(Cells(i + 28, 1), Cells(i + 30, 1309)).Calculate

'Error condition (e<10^-6)

    e1 = Abs((Cells((i + 29), 3).Value - Cells((i + 28), 3).Value) / Cells((i + 29), 3).Value)

    e2 = Abs((Cells((i + 29), 6).Value - Cells((i + 28), 6).Value) / Cells((i + 29), 6).Value)

    e3 = Abs((Cells((i + 29), 9).Value - Cells((i + 28), 9).Value) / Cells((i + 29), 9).Value)
```

```
e4 = Abs((Cells((i + 29), 12).Value - Cells((i + 28), 12).Value) / Cells((i + 29), 12).Value)
e5 = Abs((Cells((i + 29), 15).Value - Cells((i + 28), 15).Value) / Cells((i + 29), 15).Value)
e6 = Abs((Cells((i + 29), 18).Value - Cells((i + 28), 18).Value) / Cells((i + 29), 18).Value)
e7 = Abs((Cells((i + 29), 21).Value - Cells((i + 28), 21).Value) / Cells((i + 29), 21).Value)
e8 = Abs((Cells((i + 29), 24).Value - Cells((i + 28), 24).Value) / Cells((i + 29), 24).Value)
e9 = Abs((Cells((i + 29), 27).Value - Cells((i + 28), 27).Value) / Cells((i + 29), 27).Value)
e10 = Abs((Cells((i + 29), 30).Value - Cells((i + 28), 30).Value) / Cells((i + 29), 30).Value)
e11 = Abs((Cells((i + 29), 33).Value - Cells((i + 28), 33).Value) / Cells((i + 29), 33).Value)
e12 = Abs((Cells((i + 29), 36).Value - Cells((i + 28), 36).Value) / Cells((i + 29), 36).Value)
e13 = Abs((Cells((i + 29), 39).Value - Cells((i + 28), 39).Value) / Cells((i + 29), 39).Value)
e14 = Abs((Cells((i + 29), 42).Value - Cells((i + 28), 42).Value) / Cells((i + 29), 42).Value)
e15 = Abs((Cells((i + 29), 45).Value - Cells((i + 28), 45).Value) / Cells((i + 29), 45).Value)
e16 = Abs((Cells((i + 29), 48).Value - Cells((i + 28), 48).Value) / Cells((i + 29), 48).Value)
e17 = Abs((Cells((i + 29), 51).Value - Cells((i + 28), 51).Value) / Cells((i + 29), 51).Value)
e18 = Abs((Cells((i + 29), 54).Value - Cells((i + 28), 54).Value) / Cells((i + 29), 54).Value)
e19 = Abs((Cells((i + 29), 57).Value - Cells((i + 28), 57).Value) / Cells((i + 29), 57).Value)
e20 = Abs((Cells((i + 29), 60).Value - Cells((i + 28), 60).Value) / Cells((i + 29), 60).Value)
e21 = Abs((Cells((i + 29), 63).Value - Cells((i + 28), 63).Value) / Cells((i + 29), 63).Value)
e22 = Abs((Cells((i + 29), 66).Value - Cells((i + 28), 66).Value) / Cells((i + 29), 66).Value)
e23 = Abs((Cells((i + 29), 69).Value - Cells((i + 28), 69).Value) / Cells((i + 29), 69).Value)
e24 = Abs((Cells((i + 29), 72).Value - Cells((i + 28), 72).Value) / Cells((i + 29), 72).Value)
e25 = Abs((Cells((i + 29), 75).Value - Cells((i + 28), 75).Value) / Cells((i + 29), 75).Value)
e26 = Abs((Cells((i + 29), 78).Value - Cells((i + 28), 78).Value) / Cells((i + 29), 78).Value)
e27 = Abs((Cells((i + 29), 81).Value - Cells((i + 28), 81).Value) / Cells((i + 29), 81).Value)
e28 = Abs((Cells((i + 29), 84).Value - Cells((i + 28), 84).Value) / Cells((i + 29), 84).Value)
e29 = Abs((Cells((i + 29), 87).Value - Cells((i + 28), 87).Value) / Cells((i + 29), 87).Value)
e30 = Abs((Cells((i + 29), 90).Value - Cells((i + 28), 90).Value) / Cells((i + 29), 90).Value)
e31 = Abs((Cells((i + 29), 93).Value - Cells((i + 28), 93).Value) / Cells((i + 29), 93).Value)
e32 = Abs((Cells((i + 29), 96).Value - Cells((i + 28), 96).Value) / Cells((i + 29), 96).Value)
e33 = Abs((Cells((i + 29), 99).Value - Cells((i + 28), 99).Value) / Cells((i + 29), 99).Value)
```

```
e34 = Abs((Cells((i + 29), 102).Value - Cells((i + 28), 102).Value) / Cells((i + 29), 102).Value)
e35 = Abs((Cells((i + 29), 105).Value - Cells((i + 28), 105).Value) / Cells((i + 29), 105).Value)
e36 = Abs((Cells((i + 29), 108).Value - Cells((i + 28), 108).Value) / Cells((i + 29), 108).Value)
e37 = Abs((Cells((i + 29), 111).Value - Cells((i + 28), 111).Value) / Cells((i + 29), 111).Value)
e38 = Abs((Cells((i + 29), 114).Value - Cells((i + 28), 114).Value) / Cells((i + 29), 114).Value)
e39 = Abs((Cells((i + 29), 117).Value - Cells((i + 28), 117).Value) / Cells((i + 29), 117).Value)
e40 = Abs((Cells((i + 29), 120).Value - Cells((i + 28), 120).Value) / Cells((i + 29), 120).Value)
e41 = Abs((Cells((i + 29), 123).Value - Cells((i + 28), 123).Value) / Cells((i + 29), 123).Value)
e42 = Abs((Cells((i + 29), 126).Value - Cells((i + 28), 126).Value) / Cells((i + 29), 126).Value)
e43 = Abs((Cells((i + 29), 129).Value - Cells((i + 28), 129).Value) / Cells((i + 29), 129).Value)
e44 = Abs((Cells((i + 29), 132).Value - Cells((i + 28), 132).Value) / Cells((i + 29), 132).Value)
e45 = Abs((Cells((i + 29), 135).Value - Cells((i + 28), 135).Value) / Cells((i + 29), 135).Value)
e46 = Abs((Cells((i + 29), 138).Value - Cells((i + 28), 138).Value) / Cells((i + 29), 138).Value)
e47 = Abs((Cells((i + 29), 141).Value - Cells((i + 28), 141).Value) / Cells((i + 29), 141).Value)
e48 = Abs((Cells((i + 29), 144).Value - Cells((i + 28), 144).Value) / Cells((i + 29), 144).Value)
e49 = Abs((Cells((i + 29), 147).Value - Cells((i + 28), 147).Value) / Cells((i + 29), 147).Value)
e50 = Abs((Cells((i + 29), 150).Value - Cells((i + 28), 150).Value) / Cells((i + 29), 150).Value)
e51 = Abs((Cells((i + 29), 153).Value - Cells((i + 28), 153).Value) / Cells((i + 29), 153).Value)
e52 = Abs((Cells((i + 29), 156).Value - Cells((i + 28), 156).Value) / Cells((i + 29), 156).Value)
e53 = Abs((Cells((i + 29), 159).Value - Cells((i + 28), 159).Value) / Cells((i + 29), 159).Value)
e54 = Abs((Cells((i + 29), 162).Value - Cells((i + 28), 162).Value) / Cells((i + 29), 162).Value)
e55 = Abs((Cells((i + 29), 165).Value - Cells((i + 28), 165).Value) / Cells((i + 29), 165).Value)
e56 = Abs((Cells((i + 29), 168).Value - Cells((i + 28), 168).Value) / Cells((i + 29), 168).Value)
e57 = Abs((Cells((i + 29), 171).Value - Cells((i + 28), 171).Value) / Cells((i + 29), 171).Value)
e58 = Abs((Cells((i + 29), 174).Value - Cells((i + 28), 174).Value) / Cells((i + 29), 174).Value)
e59 = Abs((Cells((i + 29), 177).Value - Cells((i + 28), 177).Value) / Cells((i + 29), 177).Value)
e60 = Abs((Cells((i + 29), 180).Value - Cells((i + 28), 180).Value) / Cells((i + 29), 180).Value)
e61 = Abs((Cells((i + 29), 183).Value - Cells((i + 28), 183).Value) / Cells((i + 29), 183).Value)
e62 = Abs((Cells((i + 29), 186).Value - Cells((i + 28), 186).Value) / Cells((i + 29), 186).Value)
e63 = Abs((Cells((i + 29), 189).Value - Cells((i + 28), 189).Value) / Cells((i + 29), 189).Value)
```

```
e64 = Abs((Cells((i + 29), 192).Value - Cells((i + 28), 192).Value) / Cells((i + 29), 192).Value)
e65 = Abs((Cells((i + 29), 195).Value - Cells((i + 28), 195).Value) / Cells((i + 29), 195).Value)
e66 = Abs((Cells((i + 29), 198).Value - Cells((i + 28), 198).Value) / Cells((i + 29), 198).Value)
e67 = Abs((Cells((i + 29), 201).Value - Cells((i + 28), 201).Value) / Cells((i + 29), 201).Value)
e68 = Abs((Cells((i + 29), 204).Value - Cells((i + 28), 204).Value) / Cells((i + 29), 204).Value)
e69 = Abs((Cells((i + 29), 207).Value - Cells((i + 28), 207).Value) / Cells((i + 29), 207).Value)
e70 = Abs((Cells((i + 29), 210).Value - Cells((i + 28), 210).Value) / Cells((i + 29), 210).Value)
e71 = Abs((Cells((i + 29), 213).Value - Cells((i + 28), 213).Value) / Cells((i + 29), 213).Value)
e72 = Abs((Cells((i + 29), 216).Value - Cells((i + 28), 216).Value) / Cells((i + 29), 216).Value)
e73 = Abs((Cells((i + 29), 219).Value - Cells((i + 28), 219).Value) / Cells((i + 29), 219).Value)
e74 = Abs((Cells((i + 29), 222).Value - Cells((i + 28), 222).Value) / Cells((i + 29), 222).Value)
e75 = Abs((Cells((i + 29), 225).Value - Cells((i + 28), 225).Value) / Cells((i + 29), 225).Value)
e76 = Abs((Cells((i + 29), 228).Value - Cells((i + 28), 228).Value) / Cells((i + 29), 228).Value)
e77 = Abs((Cells((i + 29), 231).Value - Cells((i + 28), 231).Value) / Cells((i + 29), 231).Value)
e78 = Abs((Cells((i + 29), 234).Value - Cells((i + 28), 234).Value) / Cells((i + 29), 234).Value)
e79 = Abs((Cells((i + 29), 237).Value - Cells((i + 28), 237).Value) / Cells((i + 29), 237).Value)
e80 = Abs((Cells((i + 29), 240).Value - Cells((i + 28), 240).Value) / Cells((i + 29), 240).Value)
e81 = Abs((Cells((i + 29), 243).Value - Cells((i + 28), 243).Value) / Cells((i + 29), 243).Value)
e82 = Abs((Cells((i + 29), 246).Value - Cells((i + 28), 246).Value) / Cells((i + 29), 246).Value)
e83 = Abs((Cells((i + 29), 249).Value - Cells((i + 28), 249).Value) / Cells((i + 29), 249).Value)
e84 = Abs((Cells((i + 29), 252).Value - Cells((i + 28), 252).Value) / Cells((i + 29), 252).Value)
e85 = Abs((Cells((i + 29), 255).Value - Cells((i + 28), 255).Value) / Cells((i + 29), 255).Value)
e86 = Abs((Cells((i + 29), 258).Value - Cells((i + 28), 258).Value) / Cells((i + 29), 258).Value)
e87 = Abs((Cells((i + 29), 261).Value - Cells((i + 28), 261).Value) / Cells((i + 29), 261).Value)
e88 = Abs((Cells((i + 29), 264).Value - Cells((i + 28), 264).Value) / Cells((i + 29), 264).Value)
e89 = Abs((Cells((i + 29), 267).Value - Cells((i + 28), 267).Value) / Cells((i + 29), 267).Value)
e90 = Abs((Cells((i + 29), 270).Value - Cells((i + 28), 270).Value) / Cells((i + 29), 270).Value)
e91 = Abs((Cells((i + 29), 273).Value - Cells((i + 28), 273).Value) / Cells((i + 29), 273).Value)
e92 = Abs((Cells((i + 29), 276).Value - Cells((i + 28), 276).Value) / Cells((i + 29), 276).Value)
e93 = Abs((Cells((i + 29), 279).Value - Cells((i + 28), 279).Value) / Cells((i + 29), 279).Value)
```

```
e94 = Abs((Cells((i + 29), 282).Value - Cells((i + 28), 282).Value) / Cells((i + 29), 282).Value)
e95 = Abs((Cells((i + 29), 285).Value - Cells((i + 28), 285).Value) / Cells((i + 29), 285).Value)
e96 = Abs((Cells((i + 29), 288).Value - Cells((i + 28), 288).Value) / Cells((i + 29), 288).Value)
e97 = Abs((Cells((i + 29), 291).Value - Cells((i + 28), 291).Value) / Cells((i + 29), 291).Value)
e98 = Abs((Cells((i + 29), 294).Value - Cells((i + 28), 294).Value) / Cells((i + 29), 294).Value)
e99 = Abs((Cells((i + 29), 297).Value - Cells((i + 28), 297).Value) / Cells((i + 29), 297).Value)
e100 = Abs((Cells((i + 29), 300).Value - Cells((i + 28), 300).Value) / Cells((i + 29), 300).Value)
eg1 = Abs((Cells((i + 29), 305).Value - Cells((i + 28), 305).Value) / Cells((i + 29), 305).Value)
eg2 = Abs((Cells((i + 29), 308).Value - Cells((i + 28), 308).Value) / Cells((i + 29), 308).Value)
eg3 = Abs((Cells((i + 29), 311).Value - Cells((i + 28), 311).Value) / Cells((i + 29), 311).Value)
eg4 = Abs((Cells((i + 29), 314).Value - Cells((i + 28), 314).Value) / Cells((i + 29), 314).Value)
eg5 = Abs((Cells((i + 29), 317).Value - Cells((i + 28), 317).Value) / Cells((i + 29), 317).Value)
eg6 = Abs((Cells((i + 29), 320).Value - Cells((i + 28), 320).Value) / Cells((i + 29), 320).Value)
eg7 = Abs((Cells((i + 29), 323).Value - Cells((i + 28), 323).Value) / Cells((i + 29), 323).Value)
eg8 = Abs((Cells((i + 29), 326).Value - Cells((i + 28), 326).Value) / Cells((i + 29), 326).Value)
eg9 = Abs((Cells((i + 29), 329).Value - Cells((i + 28), 329).Value) / Cells((i + 29), 329).Value)
eg10 = Abs((Cells((i + 29), 332).Value - Cells((i + 28), 332).Value) / Cells((i + 29), 332).Value)
eg11 = Abs((Cells((i + 29), 335).Value - Cells((i + 28), 335).Value) / Cells((i + 29), 335).Value)
eg12 = Abs((Cells((i + 29), 338).Value - Cells((i + 28), 338).Value) / Cells((i + 29), 338).Value)
eg13 = Abs((Cells((i + 29), 341).Value - Cells((i + 28), 341).Value) / Cells((i + 29), 341).Value)
eg14 = Abs((Cells((i + 29), 344).Value - Cells((i + 28), 344).Value) / Cells((i + 29), 344).Value)
eg15 = Abs((Cells((i + 29), 347).Value - Cells((i + 28), 347).Value) / Cells((i + 29), 347).Value)
eg16 = Abs((Cells((i + 29), 350).Value - Cells((i + 28), 350).Value) / Cells((i + 29), 350).Value)
eg17 = Abs((Cells((i + 29), 353).Value - Cells((i + 28), 353).Value) / Cells((i + 29), 353).Value)
eg18 = Abs((Cells((i + 29), 356).Value - Cells((i + 28), 356).Value) / Cells((i + 29), 356).Value)
eg19 = Abs((Cells((i + 29), 359).Value - Cells((i + 28), 359).Value) / Cells((i + 29), 359).Value)
eg20 = Abs((Cells((i + 29), 362).Value - Cells((i + 28), 362).Value) / Cells((i + 29), 362).Value)
eg21 = Abs((Cells((i + 29), 365).Value - Cells((i + 28), 365).Value) / Cells((i + 29), 365).Value)
eg22 = Abs((Cells((i + 29), 368).Value - Cells((i + 28), 368).Value) / Cells((i + 29), 368).Value)
eg23 = Abs((Cells((i + 29), 371).Value - Cells((i + 28), 371).Value) / Cells((i + 29), 371).Value)
```

```
eg24 = Abs((Cells((i + 29), 374).Value - Cells((i + 28), 374).Value) / Cells((i + 29), 374).Value)
eg25 = Abs((Cells((i + 29), 377).Value - Cells((i + 28), 377).Value) / Cells((i + 29), 377).Value)
eg26 = Abs((Cells((i + 29), 380).Value - Cells((i + 28), 380).Value) / Cells((i + 29), 380).Value)
eg27 = Abs((Cells((i + 29), 383).Value - Cells((i + 28), 383).Value) / Cells((i + 29), 383).Value)
eg28 = Abs((Cells((i + 29), 386).Value - Cells((i + 28), 386).Value) / Cells((i + 29), 386).Value)
eg29 = Abs((Cells((i + 29), 389).Value - Cells((i + 28), 389).Value) / Cells((i + 29), 389).Value)
eg30 = Abs((Cells((i + 29), 392).Value - Cells((i + 28), 392).Value) / Cells((i + 29), 392).Value)
eg31 = Abs((Cells((i + 29), 395).Value - Cells((i + 28), 395).Value) / Cells((i + 29), 395).Value)
eg32 = Abs((Cells((i + 29), 398).Value - Cells((i + 28), 398).Value) / Cells((i + 29), 398).Value)
eg33 = Abs((Cells((i + 29), 401).Value - Cells((i + 28), 401).Value) / Cells((i + 29), 401).Value)
eg34 = Abs((Cells((i + 29), 404).Value - Cells((i + 28), 404).Value) / Cells((i + 29), 404).Value)
eg35 = Abs((Cells((i + 29), 407).Value - Cells((i + 28), 407).Value) / Cells((i + 29), 407).Value)
eg36 = Abs((Cells((i + 29), 410).Value - Cells((i + 28), 410).Value) / Cells((i + 29), 410).Value)
eg37 = Abs((Cells((i + 29), 413).Value - Cells((i + 28), 413).Value) / Cells((i + 29), 413).Value)
eg38 = Abs((Cells((i + 29), 416).Value - Cells((i + 28), 416).Value) / Cells((i + 29), 416).Value)
eg39 = Abs((Cells((i + 29), 419).Value - Cells((i + 28), 419).Value) / Cells((i + 29), 419).Value)
eg40 = Abs((Cells((i + 29), 422).Value - Cells((i + 28), 422).Value) / Cells((i + 29), 422).Value)
eg41 = Abs((Cells((i + 29), 425).Value - Cells((i + 28), 425).Value) / Cells((i + 29), 425).Value)
eg42 = Abs((Cells((i + 29), 428).Value - Cells((i + 28), 428).Value) / Cells((i + 29), 428).Value)
eg43 = Abs((Cells((i + 29), 431).Value - Cells((i + 28), 431).Value) / Cells((i + 29), 431).Value)
eg44 = Abs((Cells((i + 29), 434).Value - Cells((i + 28), 434).Value) / Cells((i + 29), 434).Value)
eg45 = Abs((Cells((i + 29), 437).Value - Cells((i + 28), 437).Value) / Cells((i + 29), 437).Value)
eg46 = Abs((Cells((i + 29), 440).Value - Cells((i + 28), 440).Value) / Cells((i + 29), 440).Value)
eg47 = Abs((Cells((i + 29), 443).Value - Cells((i + 28), 443).Value) / Cells((i + 29), 443).Value)
eg48 = Abs((Cells((i + 29), 446).Value - Cells((i + 28), 446).Value) / Cells((i + 29), 446).Value)
eg49 = Abs((Cells((i + 29), 449).Value - Cells((i + 28), 449).Value) / Cells((i + 29), 449).Value)
eg50 = Abs((Cells((i + 29), 452).Value - Cells((i + 28), 452).Value) / Cells((i + 29), 452).Value)
eg51 = Abs((Cells((i + 29), 455).Value - Cells((i + 28), 455).Value) / Cells((i + 29), 455).Value)
eg52 = Abs((Cells((i + 29), 458).Value - Cells((i + 28), 458).Value) / Cells((i + 29), 458).Value)
eg53 = Abs((Cells((i + 29), 461).Value - Cells((i + 28), 461).Value) / Cells((i + 29), 461).Value)
```

```
eg54 = Abs((Cells((i + 29), 464).Value - Cells((i + 28), 464).Value) / Cells((i + 29), 464).Value)
eg55 = Abs((Cells((i + 29), 467).Value - Cells((i + 28), 467).Value) / Cells((i + 29), 467).Value)
eg56 = Abs((Cells((i + 29), 470).Value - Cells((i + 28), 470).Value) / Cells((i + 29), 470).Value)
eg57 = Abs((Cells((i + 29), 473).Value - Cells((i + 28), 473).Value) / Cells((i + 29), 473).Value)
eg58 = Abs((Cells((i + 29), 476).Value - Cells((i + 28), 476).Value) / Cells((i + 29), 476).Value)
eg59 = Abs((Cells((i + 29), 479).Value - Cells((i + 28), 479).Value) / Cells((i + 29), 479).Value)
eg60 = Abs((Cells((i + 29), 482).Value - Cells((i + 28), 482).Value) / Cells((i + 29), 482).Value)
eg61 = Abs((Cells((i + 29), 485).Value - Cells((i + 28), 485).Value) / Cells((i + 29), 485).Value)
eg62 = Abs((Cells((i + 29), 488).Value - Cells((i + 28), 488).Value) / Cells((i + 29), 488).Value)
eg63 = Abs((Cells((i + 29), 491).Value - Cells((i + 28), 491).Value) / Cells((i + 29), 491).Value)
eg64 = Abs((Cells((i + 29), 494).Value - Cells((i + 28), 494).Value) / Cells((i + 29), 494).Value)
eg65 = Abs((Cells((i + 29), 497).Value - Cells((i + 28), 497).Value) / Cells((i + 29), 497).Value)
eg66 = Abs((Cells((i + 29), 500).Value - Cells((i + 28), 500).Value) / Cells((i + 29), 500).Value)
eg67 = Abs((Cells((i + 29), 503).Value - Cells((i + 28), 503).Value) / Cells((i + 29), 503).Value)
eg68 = Abs((Cells((i + 29), 506).Value - Cells((i + 28), 506).Value) / Cells((i + 29), 506).Value)
eg69 = Abs((Cells((i + 29), 509).Value - Cells((i + 28), 509).Value) / Cells((i + 29), 509).Value)
eg70 = Abs((Cells((i + 29), 512).Value - Cells((i + 28), 512).Value) / Cells((i + 29), 512).Value)
eg71 = Abs((Cells((i + 29), 515).Value - Cells((i + 28), 515).Value) / Cells((i + 29), 515).Value)
eg72 = Abs((Cells((i + 29), 518).Value - Cells((i + 28), 518).Value) / Cells((i + 29), 518).Value)
eg73 = Abs((Cells((i + 29), 521).Value - Cells((i + 28), 521).Value) / Cells((i + 29), 521).Value)
eg74 = Abs((Cells((i + 29), 524).Value - Cells((i + 28), 524).Value) / Cells((i + 29), 524).Value)
eg75 = Abs((Cells((i + 29), 527).Value - Cells((i + 28), 527).Value) / Cells((i + 29), 527).Value)
eg76 = Abs((Cells((i + 29), 530).Value - Cells((i + 28), 530).Value) / Cells((i + 29), 530).Value)
eg77 = Abs((Cells((i + 29), 533).Value - Cells((i + 28), 533).Value) / Cells((i + 29), 533).Value)
eg78 = Abs((Cells((i + 29), 536).Value - Cells((i + 28), 536).Value) / Cells((i + 29), 536).Value)
eg79 = Abs((Cells((i + 29), 539).Value - Cells((i + 28), 539).Value) / Cells((i + 29), 539).Value)
eg80 = Abs((Cells((i + 29), 542).Value - Cells((i + 28), 542).Value) / Cells((i + 29), 542).Value)
eg81 = Abs((Cells((i + 29), 545).Value - Cells((i + 28), 545).Value) / Cells((i + 29), 545).Value)
eg82 = Abs((Cells((i + 29), 548).Value - Cells((i + 28), 548).Value) / Cells((i + 29), 548).Value)
eg83 = Abs((Cells((i + 29), 551).Value - Cells((i + 28), 551).Value) / Cells((i + 29), 551).Value)
```

```
eg84 = Abs((Cells((i + 29), 554).Value - Cells((i + 28), 554).Value) / Cells((i + 29), 554).Value)
eg85 = Abs((Cells((i + 29), 557).Value - Cells((i + 28), 557).Value) / Cells((i + 29), 557).Value)
eg86 = Abs((Cells((i + 29), 560).Value - Cells((i + 28), 560).Value) / Cells((i + 29), 560).Value)
eg87 = Abs((Cells((i + 29), 563).Value - Cells((i + 28), 563).Value) / Cells((i + 29), 563).Value)
eg88 = Abs((Cells((i + 29), 566).Value - Cells((i + 28), 566).Value) / Cells((i + 29), 566).Value)
eg89 = Abs((Cells((i + 29), 569).Value - Cells((i + 28), 569).Value) / Cells((i + 29), 569).Value)
eg90 = Abs((Cells((i + 29), 572).Value - Cells((i + 28), 572).Value) / Cells((i + 29), 572).Value)
eg91 = Abs((Cells((i + 29), 575).Value - Cells((i + 28), 575).Value) / Cells((i + 29), 575).Value)
eg92 = Abs((Cells((i + 29), 578).Value - Cells((i + 28), 578).Value) / Cells((i + 29), 578).Value)
eg93 = Abs((Cells((i + 29), 581).Value - Cells((i + 28), 581).Value) / Cells((i + 29), 581).Value)
eg94 = Abs((Cells((i + 29), 584).Value - Cells((i + 28), 584).Value) / Cells((i + 29), 584).Value)
eg95 = Abs((Cells((i + 29), 587).Value - Cells((i + 28), 587).Value) / Cells((i + 29), 587).Value)
eg96 = Abs((Cells((i + 29), 590).Value - Cells((i + 28), 590).Value) / Cells((i + 29), 590).Value)
eg97 = Abs((Cells((i + 29), 593).Value - Cells((i + 28), 593).Value) / Cells((i + 29), 593).Value)
eg98 = Abs((Cells((i + 29), 596).Value - Cells((i + 28), 596).Value) / Cells((i + 29), 596).Value)
eg99 = Abs((Cells((i + 29), 599).Value - Cells((i + 28), 599).Value) / Cells((i + 29), 599).Value)
eg100 = Abs((Cells((i + 29), 602).Value - Cells((i + 28), 602).Value) / Cells((i + 29), 602).Value)
'Implementing the error condition

If e1 < 0.000001 And e2 < 0.000001 And e3 < 0.000001 And e4 < 0.000001 And e5 < 0.000001 And
e6 < 0.000001 And e7 < 0.000001 And e8 < 0.000001 And e9 < 0.000001 And e10 < 0.000001 And
e11 < 0.000001 And e12 < 0.000001 And e13 < 0.000001 And e14 < 0.000001 And e15 < 0.000001
And e16 < 0.000001 And e17 < 0.000001 And e18 < 0.000001 And e19 < 0.000001 And e20 <
0.000001 And e21 < 0.000001 And e22 < 0.000001 And e23 < 0.000001 And e24 < 0.000001 And e25
< 0.000001 And e26 < 0.000001 And e27 < 0.000001 And e28 < 0.000001 And e29 < 0.000001 And
e30 < 0.000001 And e31 < 0.000001 And e32 < 0.000001 And e33 < 0.000001 And e34 < 0.000001
And e35 < 0.000001 And e36 < 0.000001 And e37 < 0.000001 And e38 < 0.000001 And e39 <
0.000001 And e40 < 0.000001 And e41 < 0.000001 And e42 < 0.000001 And e43 < 0.000001 And e44
< 0.000001 And e45 < 0.000001 And e46 < 0.000001 And e47 < 0.000001 And e48 < 0.000001 And
e49 < 0.000001 And e50 < 0.000001 And e51 < 0.000001 And e52 < 0.000001 And e53 < 0.000001
And e54 < 0.000001 And e55 < 0.000001 And e56 < 0.000001 And e57 < 0.000001 And e58 <
0.000001 And e59 < 0.000001 And e60 < 0.000001 And e61 < 0.000001 And e62 < 0.000001 And e63
< 0.000001 And e64 < 0.000001 And e65 < 0.000001 And e66 < 0.000001 And e67 < 0.000001 And
e68 < 0.000001 And e69 < 0.000001 And e70 < 0.000001 And e71 < 0.000001 And e72 < 0.000001
And e73 < 0.000001 And e74 < 0.000001 And e75 < 0.000001 And e76 < 0.000001 And e77 <
0.000001 And e78 < 0.000001 And e79 < 0.000001 And e80 < 0.000001 And e81 < 0.000001 And e82
< 0.000001 And e83 < 0.000001 And e84 < 0.000001 And e85 < 0.000001 And e86 < 0.000001 And
e87 < 0.000001 And e88 < 0.000001 And e89 < 0.000001 And e90 < 0.000001 And e91 < 0.000001
And e92 < 0.000001 And e93 < 0.000001 And e94 < 0.000001 And e95 < 0.000001 And e96 <
```

```
0.000001 And e97 < 0.000001 And e98 < 0.000001 And e99 < 0.000001 And e100 < 0.000001 And
eg1 < 0.000001 And eg2 < 0.000001 And eg3 < 0.000001 And eg4 < 0.000001 And eg5 < 0.000001
And eg6 < 0.000001 And eg7 < 0.000001 And eg8 < 0.000001 And eg9 < 0.000001 And eg10 <
0.000001 And eg11 < 0.000001 And eg12 < 0.000001 And eg13 < 0.000001 And eg14 < 0.000001
And eg15 < 0.000001 And eg16 < 0.000001 And eg17 < 0.000001 And eg18 < 0.000001 And eg19 <
0.000001 And eg20 < 0.000001 And eg21 < 0.000001 And eg22 < 0.000001 And eg23 < 0.000001
And eg24 < 0.000001 And eg25 < 0.000001 And eg26 < 0.000001 And eg27 < 0.000001 And eg28 <
0.000001 And eg29 < 0.000001 And eg30 < 0.000001 And eg31 < 0.000001 And eg32 < 0.000001
And eg33 < 0.000001 And eg34 < 0.000001 And eg35 < 0.000001 And eg36 < 0.000001 And eg37 <
0.000001 And eg38 < 0.000001 And eg39 < 0.000001 And eg40 < 0.000001 And eg41 < 0.000001
And eg42 < 0.000001 And eg43 < 0.000001 And eg44 < 0.000001 And eg45 < 0.000001 And eg46 <
0.000001 And eg47 < 0.000001 And eg48 < 0.000001 And eg49 < 0.000001 And eg50 < 0.000001
And eg51 < 0.000001 And eg52 < 0.000001 And eg53 < 0.000001 And eg54 < 0.000001 And eg55 <
0.000001 And eg56 < 0.000001 And eg57 < 0.000001 And eg58 < 0.000001 And eg59 < 0.000001
And eg60 < 0.000001 And eg61 < 0.000001 And eg62 < 0.000001 And eg63 < 0.000001 And eg64 <
0.000001 And eg65 < 0.000001 And eg66 < 0.000001 And eg67 < 0.000001 And eg68 < 0.000001
And eg69 < 0.000001 And eg70 < 0.000001 And eg71 < 0.000001 And eg72 < 0.000001 And eg73 <
0.000001 And e74 < 0.000001 And eg75 < 0.000001 And eg76 < 0.000001 And eg77 < 0.000001 And
eg78 < 0.000001 And eg79 < 0.000001 And eg80 < 0.000001 And eg81 < 0.000001 And eg82 <
0.000001 And eg83 < 0.000001 And eg84 < 0.000001 And eg85 < 0.000001 And eg86 < 0.000001
And eg87 < 0.000001 And eg88 < 0.000001 And eg89 < 0.000001 And eg90 < 0.000001 And eg91 <
0.000001 And eg92 < 0.000001 And eg93 < 0.000001 And eg94 < 0.000001 And eg95 < 0.000001
And eg96 < 0.000001 And eg97 < 0.000001 And eg98 < 0.000001 And eg99 < 0.000001 And eg100 <
0.000001 Then Exit For

Next

        For j = 1 To 100    ('100 is the No. of CV along circumference)

        Cells(j + 2, 705).Value = Cells((i + 29), j * 3).Value

        Cells(j + 2, 703).Value = Cells((i + 29), j * 3 + 302).Value

        ArrayTs1(j) = (2 * Cells(5, 2).Value * Cells((i + 29), j * 3).Value +Cells(5, 6).Value *
        Cells(11, 2).Value* Cells(6, 6).Value) / (2 * Cells(5, 2).Value +Cells(5, 6).Value * Cells(11,
        2).Value)

        Cells(j + 2, 706).Value = ArrayTs1(j)

        Cells(j + 2, 707).Value = Cells(5, 6).Value * Cells(20, 3).Value * (ArrayTs1(j) - Cells(6,
        6).Value)

 Next j

        Cells(3, 708).Value = "=Sum(AAE3:AAE102)"

        Cells(3, 708).Calculate

End Sub
```

```
Sub TemperatureProfiles()  'Determines the HTF and surface temperature for HTF, AP and GC CVs
        Dim ArrayTf(3546) As Double
        Dim N As Double
        Worksheets("sheet4").Activate
        Range(Cells(1, 1), Cells(26, 11)).Calculate
N = Cells(13, 11).Value    'Total number of HTF CVs
k = 1
        Cells(6, 6).Value = Cells(9, 10 + k).Value
For i = 0 To N
        If i = 0 Then Exit For
        Next
                ArrayTf(i) = Cells(6, 6).Value
                Worksheets("HTF&SERIES").Cells(i + 3, k).Value = ArrayTf(i)
          Call CVTemperature
                Worksheets("HTF&SERIES").Cells(i + 3, 5).Value = Cells(3, 708).Value  'HFT CV
                energy delivered
          For j = 1 To 100   'surface temperature (100 is the No. of CV along circumference)
                Worksheets("HTF&SERIES").Cells(j + 2, i + 10 * k).Value = Cells(j + 2,705).Value
                Worksheets("HTF&SERIES").Cells(j + 105, i + 10 * k).Value = Cells(j + 2,
                703).Value
           Next j
                ArrayTf(i) = (Cells(3, 708).Value / (Cells(11, 11).Value * Cells(12, 11).Value)) +
                ArrayTf(i)
                Cells(7, 6).Value = ArrayTf(i)

  For i = 1 To Cells(13, 11).Value
                Cells(6, 6).Value = Cells(7, 6).Value
                ArrayTf(i) = Cells(7, 6).Value
                Worksheets("HTF&SERIES").Cells(i + 3, k).Value = ArrayTf(i)
        Call CVTemperature
                Worksheets("HTF&SERIES").Cells(i + 3, 5).Value = Cells(3, 708).Value 'energy
```

```
        For j = 1 To 100    '(100 is the No. of CV along circumference)
            Worksheets("HTF&SERIES").Cells(j + 2, i + 10 * k).Value = Cells(j + 2, 705).Value
            Worksheets("HTF&SERIES").Cells(j + 105, i + 10 * k).Value = Cells(j + 2, 703).Value
        Next j

            ArrayTf(i) = (Cells(3, 708).Value / (Cells(11, 11).Value * Cells(12, 11).Value)) +
            ArrayTf(i)
            Cells(7, 6).Value = ArrayTf(i)
Next i
            Worksheets("HeatLoss").Calculate
End Sub

Sub ViewFactor()            'view factor absorber to glass
Dim x1, x2, y1, y2, F, N As Double
        Worksheets("ViewFactor").Range("G7:H35").Clear
        Worksheets("sheet4").Activate
        N = Cells(2, 8).Value

For i = 0 To N
    y1 = (Cells(10, 4).Value ^ 2 + Cells(8, 2).Value ^ 2 - 2 * Cells(10, 4).Value * Cells(8, 2).Value *
    Cos((i * Cells(2, 4).Value))) ^ 0.5
    y2 = (Cells(10, 4).Value ^ 2 + Cells(8, 2).Value ^ 2 - 2 * Cells(10, 4).Value * Cells(8, 2).Value *
    Cos((i * Cells(2, 4).Value))) ^ 0.5
    x1 = (Cells(10, 4).Value ^ 2 + Cells(8, 2).Value ^ 2 - 2 * Cells(10, 4).Value * Cells(8, 2).Value *
    Cos((i + 1) * Cells(2, 4).Value)) ^ 0.5
    x2 = (Cells(10, 4).Value ^ 2 + Cells(8, 2).Value ^ 2 - 2 * Cells(10, 4).Value * Cells(8, 2).Value *
    Cos((i - 1) * Cells(2, 4).Value)) ^ 0.5
    F = ((x1 + x2) - (y1 + y2)) / (2 * Cells(8, 2).Value * Cells(2, 4).Value)
    Worksheets("ViewFactor").Cells(i + 6, 2).Value = F
Next i
End Sub
```

```
Sub ViewFactorGlass()
Dim x1, x2, y1, y2, F, N As Double
        Worksheets("sheet4").Activate
        N = Cells(2, 10).Value
For i = 1 To N
        y1 = (2 * (Cells(10, 4).Value ^ 2) * (1 - Cos((i - 1) * Cells(2, 4).Value))) ^ 0.5
        y2 = (2 * (Cells(10, 4).Value ^ 2) * (1 - Cos((i + 1) * Cells(2, 4).Value))) ^ 0.5
        x1 = (2 * (Cells(10, 4).Value ^ 2) * (1 - Cos((i * Cells(2, 4).Value)))) ^ 0.5
        x2 = (2 * (Cells(10, 4).Value ^ 2) * (1 - Cos((i * Cells(2, 4).Value)))) ^ 0.5
        F = ((x1 + x2) - (y1 + y2)) / (2 * Cells(10, 4).Value * Cells(2, 4).Value)
        Worksheets("ViewFactor").Cells(i + 6, 8).Value = F
Next i
End Sub

Sub ViewFactorSkyGlass()
Dim x, y, F As Double
        Worksheets("sheet4").Activate
        y = Cells(9, 8).Value * Sin(Cells(11, 8).Value)
        x = Cells(9, 8).Value * Sin(Cells(11, 8).Value) + Cells(8, 4).Value * Cells(2, 4).Value
        F = (2 * x - 2 * y) / (Cells(9, 8).Value * Cells(10, 8).Value)
        Worksheets("ViewFactor").Cells(5, 11).Value = F
End Sub
```

10.0 Appendix B

Calculation for the view factor using the Hottel's crossed string method

In the Figure B1, a cross section of the receiver tube is presented. Part (b) is an extract of part (a) illustrating view factor calculation for two control volumes on the AP and GC using the Hottel's crossed string method.

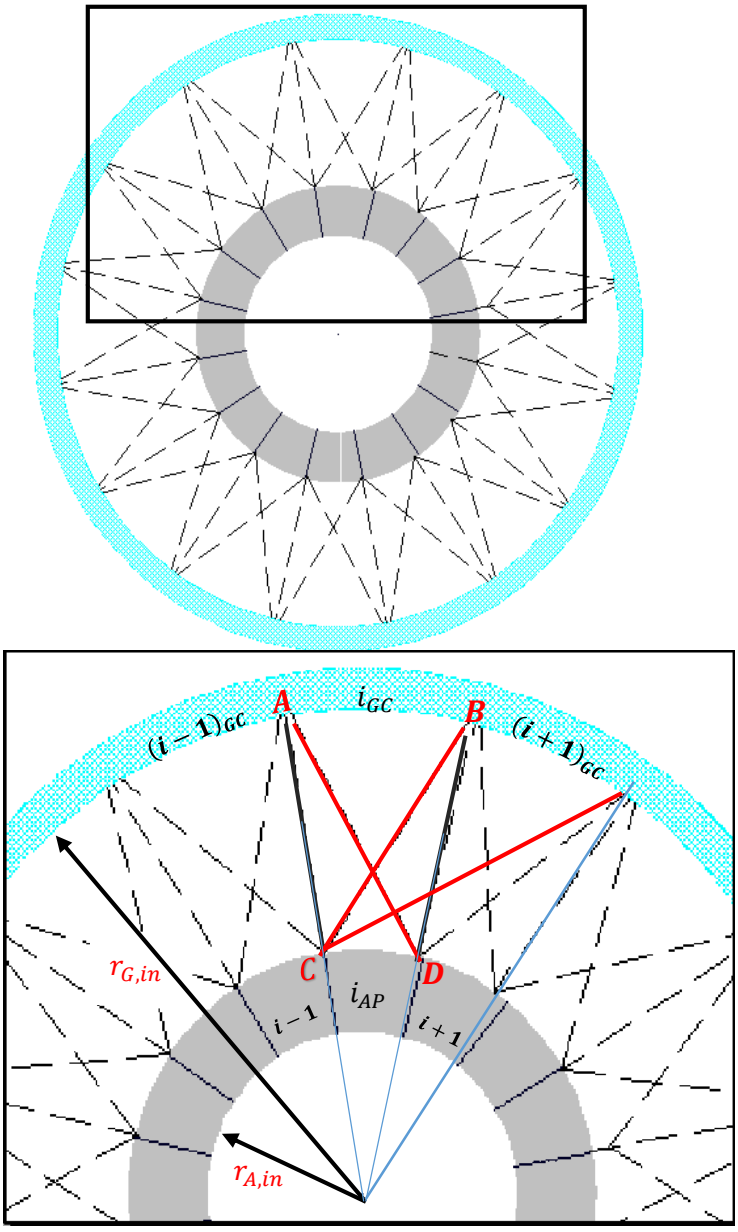

Figure B1: Illustration of implementing Hottel cross method on CVs i_{Ap}

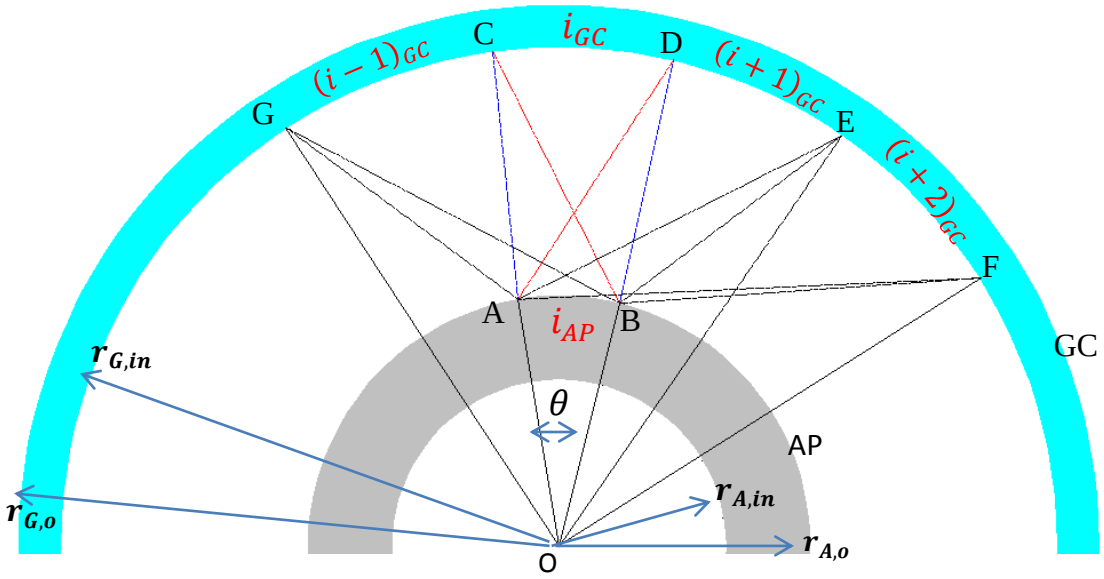

Figure B2: Illustration of Hottel's crossed string method for CVs i_{AP} and $(i \pm N)_{GC}$

From view factor notation,

$F_{i_{AP}-i_{GC}}$ represents the fraction of radiation emanating from CV i_{AP} and intercepted by CV i_{GC} or $(i \pm 1)_{GC}$. Using Hotell's crossed string method, view factor is

$$F_{i_{AP}-i_{GC}} = \frac{\sum(crossed\ strings) - \sum(uncrossed\ strings)}{2L}$$

$$L = r_{A,in}\theta \quad \text{B1}$$

$$OA = OB = r_{A,o} \quad \text{B2}$$

$$OC = OD = OE = OF = r_{G,in} \quad \text{B3}$$

Consider the exchange between CV i_{AP} and CV i_{GC}. From Figure B2; the lengths AD, BC, are the crossed lengths. AC and BD are the uncrossed strings. L is the length in cross section view, of the emitting surface. These lengths are:

$$AD = (OA)^2 + OD^2 - 2(OA)(OD)\cos\theta \quad \text{B4}$$

$$BC = (OB)^2 + OC^2 - 2(OB)(OC)\cos\theta \quad \text{B5}$$

$$AC = BD = r_{G,in} - r_{A,out} \quad \text{B6}$$

Therefore, substituting with the geometric parameters in equation B4 and B5;

$$AD = \left(r_{G,in}\right)^2 + \left(r_{A,out}\right)^2 - 2\left(r_{G,in}\right)\left(r_{A,out}\right)\cos\theta \quad \text{B8}$$

$$BC = \left(r_{G,in}\right)^2 + \left(r_{A,out}\right)^2 - 2\left(r_{G,in}\right)\left(r_{A,out}\right)\cos\theta \quad \text{B9}$$

It's seen that for a case of CV i_{GC} (the intercepting area) being directly above CV i_{AP} (the emitting area), the lengths

$AD = BC$;

Therefore,

$$F_{i_{AP}\to i_{GC}} = \frac{(AD + BC) - (AC + BD)}{2L}$$

$$F_{i_{AP}\to i_{GC}} = \frac{2(AD) - 2(AC)}{2L}$$

$$F_{i_{AP}\to i_{GC}} = \frac{(AD) - (AC)}{L}$$

$$F_{i_{AP}\to i_{GC}} = \frac{(OB)^2 + OC^2 - 2(OB)(OC)\cos\theta - (AC)}{L}$$

$$F_{i_{AP}\to i_{GC}} = \frac{\left((r_{A,o})^2 + (r_{G,in})^2 - 2(r_{G,in})(r_{A,o})\cos\theta\right) - (r_{G,in} - r_{A,o})}{L} \quad \text{B10}$$

The remaining control volumes on the GC (labeled $(i \pm 1)_{GC}$, $(i \pm 2)_{GC}$, up to $(i \pm N)_{GC}$) are not located directly above CV i_{AP}. They are displaced $(N * \theta)$ from CVi_{AP}. N is the number by which a CV on GC is displaced from CVi_{AP} .

Uncrosses lengths (Labeled UX):

$$UX_1 = \left(r_{A,o}\right)^2 + \left(r_{G,in}\right)^2 - 2\left(r_{A,o}\right)\left(r_{G,in}\right)\cos(N\theta) \quad \text{B11}$$

$$UX_2 = \left(r_{A,o}\right)^2 + \left(r_{G,in}\right)^2 - 2\left(r_{A,o}\right)\left(r_{G,in}\right)\cos(N\theta) \quad \text{B12}$$

Crossed lengths (labeled X)

$$X_1 = r_{G,in} - r_{A,o} \qquad \text{for } N = 1 \tag{B13}$$

$$X_1 = \left(r_{A,o}\right)^2 + (r_{Gin})^2 - 2(r_{Ao})(r_{Gin})\cos\left((N-1)\theta\right) \qquad \text{For } N > 1 \tag{B14}$$

$$X_2 = \left(r_{A,o}\right)^2 + (r_{Gin})^2 - 2(r_{Ao})(r_{Gin})\cos\left((N+1)\theta\right) \tag{B15}$$

For CV $(i \pm N)_{GC}$, the view factor is as follows:

$$F_{i_{AP}\to(i\pm N)_{GC}} = \frac{\sum(crossed\ strings) - \sum(uncrossed\ strings)}{2L}$$

$$F_{i_{AP}\to(i\pm N)_{GC}} = \frac{\sum(X_1+X_2) - \sum(UX_1+UX_2)}{2L} \tag{B16}$$